Polarity development by asymmetric protein-cluster distributions in response to cortical flows in *C. elegans* zygotes

Jessica Aylish M^{c}Quade

A dissertation submitted in partial fulfillment

of the requirements for the degree of

Doctor of Philosophy

of

Imperial College London.

Department of Life Sciences

Imperial College London

February 17, 2022

I, Jessica Aylish M^{c}Quade, confirm that the work presented in this thesis is my own. Where information has been derived from other sources, I confirm that this has been indicated in the work.

The copyright of this thesis rests with the author. Unless otherwise indicated, its contents are licensed under a Creative Commons Attribution-Non Commercial 4.0 International Licence (CC BY-NC). Under this licence, you may copy and redistribute the material in any medium or format. You may also create and distribute modified versions of the work. This is on the condition that: you credit the author and do not use it, or any derivative works, for a commercial purpose. When reusing or sharing this work, ensure you make the licence terms clear to others by naming the licence and linking to the licence text. Where a work has been adapted, you should indicate that the work has been changed and describe those changes. Please seek permission from the copyright holder for uses of this work that are not included in this licence or permitted under UK Copyright Law.

Abstract

Asymmetric cell-division in the one-cell embryo is a key step in embryonic development. The initially homogeneous zygote establishes an anterior-posterior axis within the cell, allowing for the unequal distribution of cell fate determinants and subsequent cell differentiation. Therefore, polarity development is a fundamental procedure that defines the information template from which all future cell processes derive their cues. Many molecular players in polarity formation in *C. elegans* have been identified, but the design principles that underpin their interactions and how this contributes to successful polarisation remain unclear. This thesis focuses on the role of the clustering species PAR-3 and how its integration in the governing biochemical network promotes robust polarisation.

To correctly proceed to the two-cell stage, the foundational step of polarity formation must be responsive to the polarising cue and maintain established domains ready for downstream cell-cycle processes. We characterise global flows along the polarity axis and investigate coupling between the cortical flows and PAR-3 cluster sizes. We find there is no dynamic advantage for larger clusters and instead conclude all clusters flow with the same efficiency. Alternatively, we investigate whether enhancement of clusters is a response to mechanical forces within the cortex during the period of flow but find little direct evidence of this relationship. Rodriguez et al proposed kinase cycling between inactive (advective) and inactive (diffuse) state. We model two distinct reaction pathways through reaction-advection-diffusion simulation and assess their viability by implementation of Approximate Bayesian Computation. We find that direct binding through a flow-sensing, inactive state, followed by switching to a diffuse active state yields a network that is unviable and sensitive to perturbation. Sensitivity is alleviated when

the advective species serves only to enhance independent binding of the active species. Therefore, we propose kinase cycling through this network motif as a mechanism towards enhanced robust polarisation.

Acknowledgements

I would like to extend my unreserved thanks to Prof. Robert Endres for providing me the learning opportunity of this project. I am grateful for the continuous support of our collaborator, Dr Nate Goehring. Particular thanks go to my experimental collaborator, Rukshala Illukkumbura, for the provision of data that made this project possible. Finally, I would like to dedicate this work to Jonathan Kuhnel - for teaching me that the only real form of failure is giving up.

Contents

1 Introduction **10**

1.1 Mathematical descriptions of pattern formation and self-organisation . . 13

1.1.1 Common motifs in patterning networks 17

1.2 Models of pattern formation in cells 17

1.2.1 Pattern formation in the *C. elegans* zygote 21

1.2.2 Polarity in *C. elegans*: the PAR proteins 23

1.2.3 Ensuring successful polarisation in *C. elegans* 28

1.3 Motivation and approach 29

2 PAR-3 cluster dynamics as a result of interaction with the cortex **33**

2.1 Biological Background 34

2.1.1 The cellular cortex is a dynamic, complex structure 34

2.1.2 Cellular flows arise as a result of mechanical forces in the acto-myosin cortex 38

2.1.3 Feedback between the cellular cortex, its regulators and the PAR proteins 40

2.1.4 The role of the scaffold protein, PAR-3 43

2.1.5 Open Questions 44

2.2 Image analysis of PAR-3 clusters *in-vivo* 46

2.2.1 PAR-3 cluster movement is closely associated to anteriorly directed myosin flows in the cortex 46

2.2.2 PAR-3 cluster size does not affect its efficiency of translocation towards the anterior . . . 51
2.2.3 PAR-3 clusters are not enlarged as a direct by-product of cortical contractions . . . 52
2.3 Discussion . . . 54
2.4 Methods . . . 57
2.4.1 Experimental Imaging . . . 57
2.4.2 Single particle Tracking . . . 57
2.4.3 Particle Image Velocimetry . . . 57
2.4.4 Global flow along the anterior-posterior axis . . . 59
2.4.5 Local flows of PAR-3 clusters on the membrane . . . 60
2.4.6 Divergence of the cortex at the position of a PAR-3 cluster . . . 62

3 Tables (Image Analysis) 64

4 Reaction-diffusion modelling to uncover the design principles of polarity development in the *C. elegans* zygote 66

4.1 Reaction-diffusion models describing of the PAR proteins and cellular cortex 66
4.1.1 Modelling the anterior PAR proteins . . . 70
4.1.2 Design principles in reaction-diffusion models of the PAR proteins 73
4.2 A 'simple' 2-PAR model of cell polarity . . . 74
4.3 An extended model of cell polarity; the aPKC cycle . . . 82
4.3.1 Open Questions . . . 85
4.3.2 Motivation of modelling choices . . . 87
4.3.3 Reaction pathways for PAR polarity model with an aPKC cycling motif . . . 89
4.3.4 Parametrising the extended models of polarity formation . . . 97
4.3.5 Advection along the anterior-posterior axis . . . 102
4.4 Characteristics of polarisation in the extended models of the aPKC cycle 103

4.4.1 The effect of the relative proportion of active and flow-sensing anterior protein on polarisation of the extended polarity models . . 110
4.4.2 The effect of the relative diffusivity of active protein on polarisation of the extended polarity models 119
4.4.3 The effect of network topology in a mass-conserved model of the aPKC cyle 123
4.4.4 Sensitivity in the coupled model of the aPKC cyle 127
4.5 Bayesian analysis of the extended aPKC models of cell polarity 128
4.5.1 Approximate Bayesian Computation 129
4.5.2 The uncoupled model polarises more robustly than the coupled model 131
4.5.3 The extended aPKC models are less robust to changes in relative antagonism than the 'simple' 2-PAR model. 134
4.5.4 Discussion 140
4.6 Methods 143
4.6.1 Processing and assessing steady states 143
4.6.2 Numerical simulations 147
4.6.3 Approximate Bayesian Computation 152

5 Conclusions and Outlook **156**

Appendices **160**

A Model parametrisations **160**

Bibliography **164**

List of Figures

1.1 Experimental evidence of self-organised development 12

1.2 Simple mathematical models can describe complex patterns. 15

1.3 Polarisation in the single cell enables diverse functions. 19

1.4 The first asymmetric division in the nematode *C. elegans*. 23

1.5 The PAR proteins redistribute to form domains. 24

1.6 Anterior PAR components. 26

1.7 Posterior PAR components. 27

1.8 Mutual antagonism underpins polarity of the PAR system. 28

2.1 Cortical flows are coupled to reorganisation of the acto-myosin cortex. . . 35

2.2 Activity of the small GTPase Rho regulates contractility 41

2.3 Global flow of PAR-3 closely matches that of cortical NMY-2 47

2.4 PAR-3 motion can be decomposed into constituent advective and diffusion components. 49

2.5 Advective and diffusive contributions to motion of the PAR-3 population. 50

2.6 Larger PAR-3 clusters do not translocate to the anterior with greater efficiency. 52

2.7 Larger PAR-3 clusters are not localised preferentially in areas of local contraction. 53

2.8 PAR-3 clusters do not undergo preferential size enhancement after localisation in a region of contraction. 54

2.9 Schematic of Particle Image Velocimetry. 58

2.10 Decomposition of a vector of motion into contributions of advective and diffusive motion. 61

2.11 Divergence in the global flow field of NMY-2 63

4.1 The anterior PAR proteins can respond to flows in the absence of posterior PAR proteins. 77

4.2 Schematic of the 'simple' 2-PAR model 78

4.3 The 2-PAR model is multi-stable in character 80

4.4 The 2-PAR model can both establish and maintain domains. 81

4.5 Schematic of the aPKC cycle. 85

4.6 Schematic of the coupled PAR model. 91

4.7 Schematic of the uncoupled PAR model. 94

4.8 Initial simulation states. 99

4.9 Approximate velocity profile implemented in the reaction-advection-system. 103

4.10 The extended aPKC models are bi-stable in nature and are therefore able to polarise. 104

4.11 The extended models of cell polarity can respond to a polarising cue to establish and maintain polarity. 107

4.12 Poised at the edge of bi-stability, polarisation in the coupled model is sensitive to perturbation of relative antagonism. 109

4.13 The coupled model requires an unviable reconfiguration of relative antagonism to achieve bi-stability when switching between an active and flow-sensing anterior membrane system configuration. 113

4.14 The coupled model cannot produce biologically viable domains when favouring any functional configuration of the anterior proteins. 114

4.15 The uncoupled model can produce biologically viable domains when favouring any functional configuration of the anterior proteins. 116

4.16 The hyper-sensitivity of the coupled model to relative antagonism is amplified when favouring both a 'cue-sensing' and 'active' anterior state. . . 117

4.17 Polarisation outcomes remain stable when switching between a 'cue-sensing' and 'active' state in the uncoupled model. 119

4.18 In the coupled model, the anterior system configuration has a strong effect on the requirements for polarisation unless the diffusivity of *pPAR* is slowed. 120

4.19 In the uncoupled model, the dynamic regime dictates the outcomes of polarisation and not the anterior system configuration. 122

4.20 Schematic of the 'symmetric' PAR model. 124

4.21 The symmetric system reveals tight coupling between species diffusivity and activity in an aPKC model defined by a cyclic motif. 125

4.22 The symmetric system can only polarise effectively when in a 'flow-sensing' configuration. 126

4.23 Scheme describing Approximate Bayesian Computation 130

4.24 Bayesian Computation reveals compressed regions of successful polarisation in the coupled model. 132

4.25 Polarisation in the uncoupled model is most robust when pPAR diffuses slowly. 133

4.26 The extended aPKC models require increased control over relative rates of antagonism. 135

4.27 Comparison of the regions of acceptance across polarity models. 136

4.28 Summary statistics reveal that the coupled model is unable to balance domain concentrations and domain gradients. Conversely, the uncoupled model consistently controls these characteristics. 138

4.29 Polarity profiles of the highest and lowest scoring accepted parameter sets. 139

4.30 The separation of steady states can predict the position of domain equality. 146

4.31 Algorithm describing the custom-built numerical solver. 150

4.32 A comparison of the results of the custom-built solver and Mathematica NDSolve. 151

4.33 The allocation of distance scores based on characteristics of polarisation. 154

4.34 A manual investigation of distance scores and their associated polarisation outcomes. 155

List of Tables

3.1 Calculated dimensions of *C. elegans* embryos. 64

3.2 Particle Image Velocimetry vectors for PAR-3 global flow analysis. 64

3.3 Particle Image Velocimetry vectors for NMY-2 global flow analysis. . . . 65

3.4 Single particle tracks for PAR-3 local flow analysis. 65

4.1 Best fit to accepted simulation data in log-log space for polarity models. . 136

A.1 Parametrisation of the coupled aPKC model. 161

A.2 Parametrisation of the symmetric aPKC model. 162

A.3 Parametrisation of the uncoupled aPKC model. 163

Chapter 1

Introduction

> We have come to the edge of a world of which we have no experience, and where all our preconceptions must be recast.
>
> — D'Arcy Thompson

The question of how order arises from disorder, or more completely from homogeneity, has been a long-standing riddle the sciences have endeavoured to solve. Philosophers, biologists and physicists alike have come to question 'What is life?' and how did it come to its reproducible form? Aristotle saw that the natural world around him, particularly biological phenomena, could not be explained without consideration of natural teleology - that growth of forms didn't occur 'because it happened so in their coming to be', rather, that an organism's form served to fulfil a final purpose [1]. In pre Darwinian times, this purpose could have been pre-supposed by God whilst post Darwinian understanding would instead attribute such purpose to natural selection [2]. Modern research instead shows that the development of form, the emergence of the head from the tail, arises from tightly controlled, self-organising biochemical networks. As such, perhaps a more apt question to ask is 'what is the purpose of these interactions, and what principles do they follow to give rise to the forms we observe?'

In his Critique of Judgement, Immanual Kant outlined his belief that understanding of these 'natural ends' of organisms could not be uncovered by the empirical sciences, where application of mechanistic descriptions to describe causal relationships served only as an indicator of the limited faculties of human understanding [3]. Though pessimistic

in outlook, the work caught the attention of those in the natural sciences igniting a new field of study in developmental biology - that which sought to gain a mechanistic understanding of development in the natural world using mathematics. Over 100 years on from the genesis of the field of the physics of development, this thesis looks to investigate the design principles embedded in the biochemical networks that underpin the most fundamental of developmental steps: the self-regulated and self-organised initial division of the single cell.

With the advancement of microscopes, the initial belief that organisms were fully preformed in sex cells made way for epigenesis - that an embryo develops progressively from an undifferentiated egg cell. The cell theory closely followed, with Theodor Schwann stating that "there is one universal principle of development for the elementary parts of organisms... and this principle is in the formation of cells" [4] [5]. In the wake of this discovery of the 'basic unit of life', an important distinction was drawn between the somatic and germ cells, with August Weismann proposing in his 'Theory of the Germplasm' that inheritance occurred solely through the germ cells and therefore mutations in the the soma had no effect on future generations [6].

Inheritance was believed to occur through the transmission of nuclear determinants, the composition of which provided resources for the creation of varying cellular components and thus determined the character of a cell. The combinatorial effect of different determinant architectures, coupled with the unequal inheritance of determinants through cell cleavage could therefore account for the complex organisms observed in the natural world [7]. Two cornerstone experiments probed this 'mosaic theory' of development and the notion of pre-determined fate, but only one glimpsed the fundamental principle underlying natural development. With the belief that differentiation arose through the segregation of genetic determinants, Wilhelm Roux perturbed the development of frog blastomeres at the 2- cell stage, expecting to evidence the mosaic theory of development - see fig. 1.1 [8]. Ablation of a single blastomere resulted in the continued development of only half the embryo, with the remaining blastomere continuing its usual development as if still associated with the living other. Incorrectly, this observation served only to

corroborate the existence of predetermined fate and in Roux's mind, the mosaic theory of development.

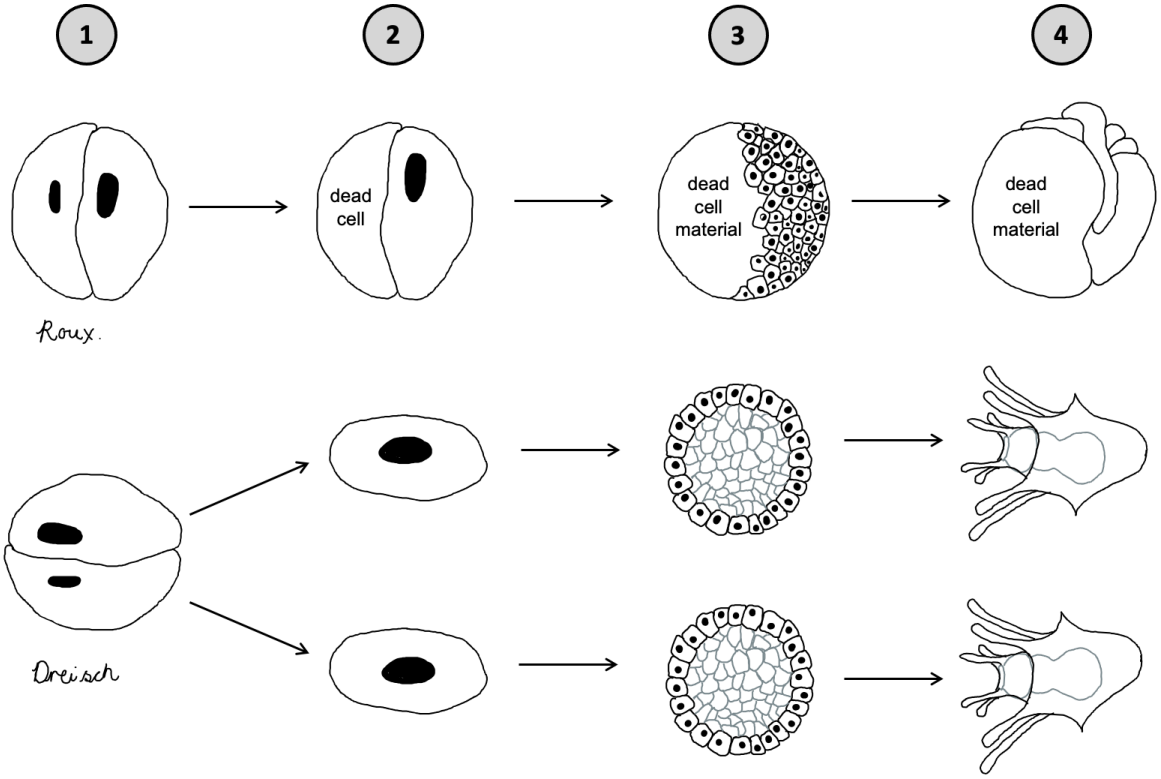


Figure 1.1: Development occurs in a self-organised manner. Observations of development in the experiments of Dreisch and Roux. **(1)** Both experiments begin with a single cell **(2)** After the first division Roux killed the second cell, whilst Dreisch separated the cells by shaking **(3)** The blastomeres of the living cells continued to develop **(4)** Roux observed full development of only half the embryo, whilst Driesch observed the complete development of two, slightly smaller, organisms. Roux incorrectly neglected the effect of the dead material in the embryo and concluded development was mosaic. Driesch instead provided the first evidence that development was self-organised, with the propensity to develop into a complete organism contained within each single cell.

Similar experiments in sea urchins painted a rather different picture of development. When separating the two blastomeres completely Dreisch observed that each cell had the capability to continue developing into a complete larva - see fig. 1.1. This observation confounded Dreisch, who was forced to relinquish the preconceived ideas of 'mosaic development' and re-imagine the principles of development. Inspired by the maverick D'Arcy Thompson, whose seminal work 'On growth and form' work sought to describe the morphology of the natural world with mathematical law, Dreisch sought to interpret

his findings using the language of the physical sciences. Attempts to explain his 'harmonious equipotential system' using the mathematics and physics of the time proved futile for Dreisch. He condemned D'Arcy Thompson's work as serving only to explain 'the general frame for the process' and surrender to the vitalistic belief 'that the phenomena of life are dependent on principles distinct from those of physical law' [8]. Unbeknownst to Dreisch, his landmark experiment provided the first empirical evidence that the embryo could be represented as a self-organised system - one in which the emergence and development of order arose as a result of internal interactions [9]. Hypothesised by Kant, observed by Dreisch and explored in this thesis, the mathematical study of self-organising systems remains a widely active field of study to date.

1.1 Mathematical descriptions of pattern formation and self-organisation

> ...it would be absurd for humans even... to hope that there may yet arise a Newton who would make comprehensible even the generation of a blade of grass according to natural laws...
>
> — Immanual Kant

Following Dreisch's landmark experiment, over half a century would pass before a complete mathematical framework describing biological self-organising systems would be developed. The initial bewilderment of Dreisch gave way to a flood of physiochemical descriptions of the origins of life and in the wake of the discovery of DNA, the divergence of the attention of theoretical biologists of the time [10]. Whilst descriptions of patterning biological systems underwent an incubation period, initial descriptions of chemical self-organised systems had already been established - the simplest of which described the collective behaviour of molecules in a heated liquid [11]. Henri Benard observed that, at a critical temperature, the heated system reached a bifurcation point beyond which the molecules within the system collectively moved up or down forming observable and distinct 'Benard' rolls. Order emerged from disorder, the organisation of which could not

have been predicted by analysis of individual components of the system.

A first step towards considering the dynamics of self-organisation in biological systems was taken by the eminent chemist, Alfred Lotka. Having already formulated a mathematical framework to describe oscillatory dynamics in chemical reactions, he applied the same formality to illustrate the origins of perpetual oscillatory dynamics of coupled predator-prey species. However, alongside many other studies attempting to observe or describe biochemical self-organising systems at the time, Lotka's work was viewed unfavourably and remained on the periphery of scientific interest [12]. Though elements of the framework had previously been described, it wasn't until the dawn of Turing's seminal work - 'The Chemical Basis of Morphogenesis' - that the mathematical world of biological pattern formation came to light.

In his cornerstone work, Turing describes a morphogen – a chemical substance – which diffuses within a tissue and additionally, reacts with other morphogens to create variations in spatial distributions that give rise to patterns with a repeating period [13]. In well-mixed conditions, the Turing mechanism allows for a stable, uniform steady state to exist; a state resembling the homogeneous single cell. A diffusion-driven instability drives the system away from this homogeneous steady state, initiating self-organisation to an inhomogeneous spatial distribution with a regular period – a patterned tissue. Importantly, the solutions of the Turing mechanism result in complex patterns of stationary or oscillatory nature. Theoretical work can replicate the stationary patterning seen on sea shells and puffer fish skin (fig. 1.2), whilst travelling wave solutions faithfully replicate the spiral patterning of interacting *Dictyostelium discoideum* during aggregation (Sawai 2000). Able to give rise to a plethora of patterns, the characterisation of a Turing mechanism *in-vivo* remains a principle goal of research to this day.

A notable extension of the Turing mechanism was proposed by Gierer and Meinhardt who showed that to minimally generate a Turing instability the reaction network need consists of only a short-range slowly diffusing activator and a long-range, quickly diffusing inhibitor. The theory was inspired by the work of Reichardt and Kirschfeld, who noted that the human visual system relied on contrast enhancement to amplify tiny changes



Figure 1.2: Simple mathematical models can describe complex patterns. Mathematical descriptions of interacting reactants can theoretically reproduce the patterning observed in nature. **(Left)** A Turing mechanism can produce the patterning observed on puffer fish skin. **(Middle)**A Grier-Meinhardt mechanism can reproduce the stripes on zebra-fish skin. **(Right)** The French flag model can compartmentalise sections in the direction of a reactant gradient - alike its namesake. Images: Chiswick Chap (puffer fish), Oregon State University (zebra fish) under the licenses https://creativecommons.org/licenses/by-sa/3.0/deed.en, https://creativecommons.org/licenses/by-sa/2.0/deed.en. respectively.

in input [14][15]. From an initially uniform state, stochastic fluctuations in morphogen concentrations can cause the activator to become locally non-uniform. This inhomogeneity in concentration is amplified by the positive-feedback loop of the activator. In turn, this local amplification increases the production of the inhibitor morphogen [16]. The inhibitor diffuses more quickly than the activator, causing limited repression at the peaks which as a result can stabilise. Neighbouring areas of increased inhibitor concentration mean that the activator cannot increase its local concentration, repressing peak formation in nearby zones. Patterning in this way frequently results in spots or stripes, with the size of the repeat characteristic of the global parametrisation of the system.

The Grier-Meinhardt motif has been implemented computationally to faithfully reproduce biological patterns. Nakamasu and colleagues showed that the reactionary network responsible for *in-vivo* striped pigmentation patterns on zebra-fish skin (fig. 1.2) fulfilled the requirements for a Turing mechanism, computationally reproducing the temporal patterning process observed in their laser ablation experiments [17]. Similarly, this combination of experiment and reaction-diffusion modelling has been utilised to identify

the transforming growth factor proteins Lefty and Nodal as an activator-inhibitor pair responsible for left-right asymmetry in the mouse embryo [18]. Further, activator-inhibitor motifs have also been used to explain the root hair patterning in the epidermis of the *Arabidopsis* plant, the spotted follicle spacing in murine rodents and the spacing of the striped ridges of mice palates [19][20][21].

Perhaps one of the simplest described mechanisms of biological pattern formation is that where a morphogen diffuses across a tissue. Such a model, termed the French Flag model, was introduced by Lewis Wolpert to explain the size-independent genetic patterning observed in morphogenesis (Wolpert). This scale invariance was observed in the earlier discussed experiments of Hans Driesch, where splitting of the urchin blastomere at the 2-cell or 4-cell stage resulted in properly developing larva, implying that each cell was endowed with a patterning mechanism and hence regulated its own development [22]. Given a morphogen source and an opposing morphogen sink, morphogen diffusion creates a linear gradient between these positions (given no interim production or degradation) [23]. This gradient is then interpreted by its target cells, who have a threshold response to the morphogen concentration. If there are at least two such thresholds, expression of target cells would give rise to the models three stripes – alike its name-sake French flag (fig. 1.2). Responding to a local change in morphogen concentration, the target cells are not irreversibly tied to a given fate, allowing the pattern to remain in a dynamic equilibrium state. Patterning in this way is controlled by the boundary condition imposed on the tissue - here the inclusion of a source and sink – and so is scale invariant. This more simplistic gradient mechanism has been implemented to successfully describe patterning in a range of processes, including chick limb development and the bicoid protein gradient responsible for gene patterning and segmentation along the dorsal-ventral axis of the drosophila zygote [24][25]. Alike the behaviour of the Benard rolls, a clear limitation to this simple mechanism of pattern formation is that spatial distributions of morphogens can only arise if there is a continuous local source supplying the system. Importantly, the necessity for a morphogen pre-pattern means that unlike a Turing mechanism, patterning in this manner cannot occur spontaneously or be maintained should the patterning cue

be removed [26].

1.1.1 Common motifs in patterning networks

As illustrated in section 1.1, the exact mechanism of pattern formation can vary among species and patterning process. However, there exists universal features within the biochemical networks that successfully describe these self-organising, patterning processes.

- **Negative feedback** Negative feedback results when the product of a reaction inhibits the rate at which the reaction occurs and the product is produced. Negative feedback functions as a control mechanism, working to attenuate a biochemical process [27]. Examples of negative feedback that are key to the work in this thesis are that of substrate-depletion and mutual antagonism. Substrate depletion is a common feature in conserved systems, where the forward reaction of a finite substrate to a new state eventually depletes the resource, stalling the rate of the reaction [28]. Antagonism is where the presence of one product either limits the forward reaction of second reactant, or promotes the backward reaction of the second product.

- **Positive feedback** Positive feedback results when the product of a reaction further enhances the rate at which the reaction occurs and the product is produced. Positive feedback is necessary for the amplification of a system perturbation. The strength of this positive feedback loop dictates the sensitivity of a network to a stimulus [29]. An example of positive feedback that is key to this thesis is that of cooperative binding, where self-recruitment by a molecule enhances its local concentration and further self-recruitment. Interestingly, when two components mutually antagonise each other, the resultant function is that of positive feedback [30].

1.2 Models of pattern formation in cells

Perhaps the most fundamental example of pattern formation is that of polarity formation: the demarkation of a system into two separate domains. Polarisation is a key process in the life-cycle of cells, crucial for a range of cell functions including differen-

tiation, division, migration and immune response. Polarisation is overseen by polarity determinants that are able to respond to extracellular cues, initialising the polarisation process. Following cue-sensing, the determinants reinforce the cue through mechanisms of positive (or negative) feedback. Spatial information is relayed through the signalling network to downstream components which self-organise to produce and maintain patterning. Through this patterning, the propagation of asymmetric cues enable the cell to carry out specific functions - see fig. 1.3.

In the budding yeast, *Saccharomyces cerevisiae*, polarisation occurs to enable the cell to divide and propagate (fig. 1.3a). The yeast cell is initially round and grows isotropically. However, in response to an external cue - derived from a budding scar left on the cortex from a previous division, the cell undergoes a symmetry breaking event and begins to grow a peripheral 'bud' [31]. The budding process is governed by the Rho-GTPase CDC-42, with CDC-42 mutant phenotypes observed to instead continue to grow isotropically before arresting [32]. Polarisation can occur both spontaneously and in response to an external cue [33]. CDC-42 is upregulated at a single site and through its activation triggers the polarisation of the cytoskeleton. This up-regulation is an example of a positive feedback loop that drives polarisation. Local enhancement of CDC-42 results in localised assembly of actin patches and reorientation of actin cables towards the bud site. Together, these facilitate polarised vesicle secretion and asymmetric growth. The resulting bud eventually undergoes cytokinesis resulting in the formation of a second yeast cell [34]. In a separate division process, the rod-like bacterium *Escherichia coli* instead utilises polarisation to discern the point of mid-cell and symmetrically divide (fig. 1.3d). Such a process is governed by the Min system, comprising Min-D, Min-E and Min-C. Initially, Min-D binds to the membrane, where it forms dimers in an ATP-dependent manner. These dimers undergo rapid diffusion and rapid dissociation. Membrane bound Min-D undergoes cooperative binding: in high-density regions, association to the membrane is enhanced. This positive-feedback process results in accelerated uptake of Min-D to cell membrane. In these high-density regions, diffusion and rates of membrane dissociation are slowed. Min-C diffuses freely in the cytosol and associates with the membrane bound

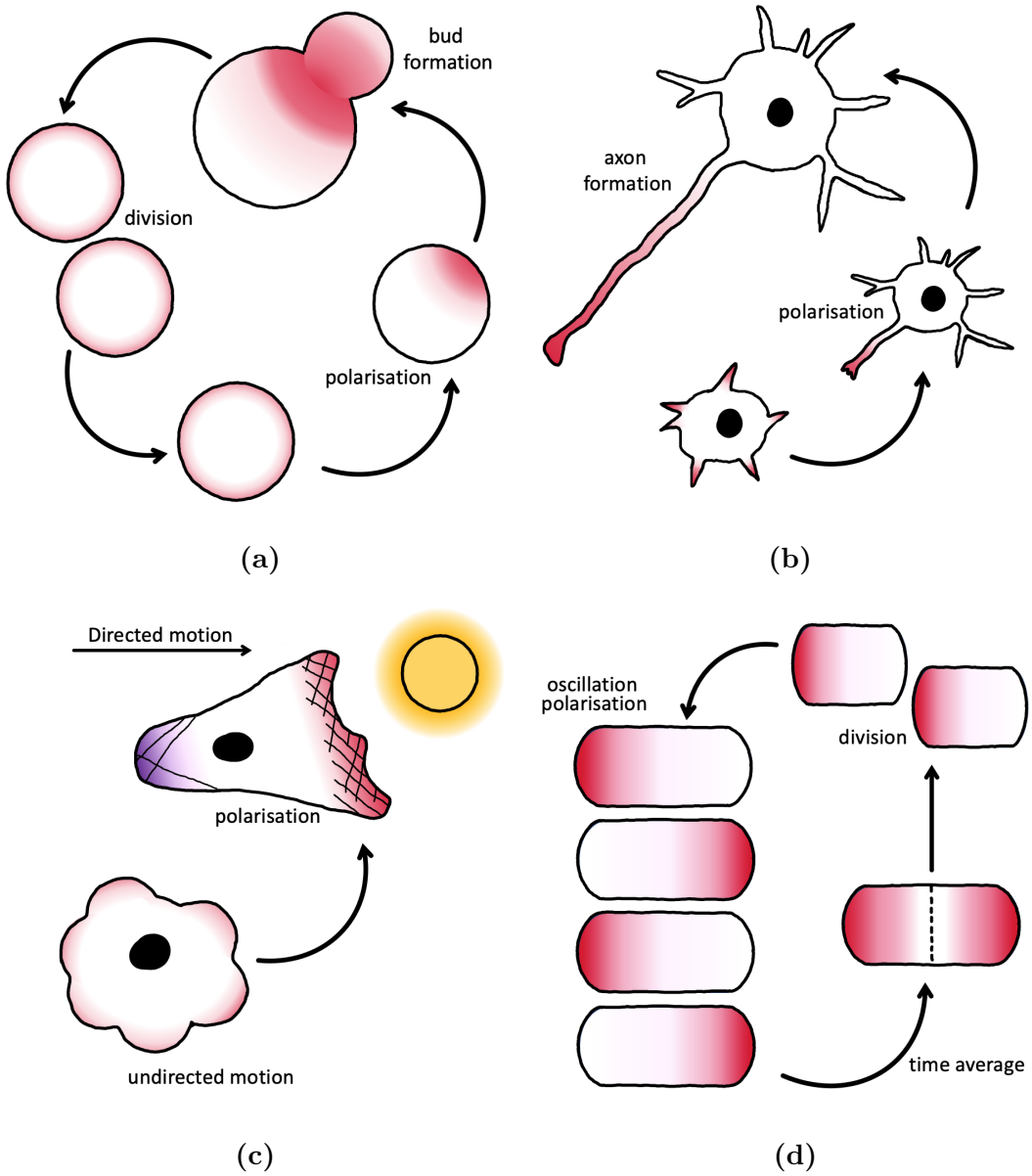


Figure 1.3: Polarisation in the single cell enables diverse functions. **(a)** Polarisation of CDC-42 concentrations in the yeast S. *cerevisiae* underpins cell proliferation. **(b)** Polarisation of cyto-skeletal components such as microtubules dictates axon specification in neuronal development. **(c)** Polarisation of the cytoskeleton in response to a chemoattractant enables directed cell motility. **(d)** Oscillatory dynamics of spatially polarised Min proteins enables *Escherichia coli* to sense the cell centre and divide symmetrically.

Min-D, where is it able to inhibit FtsZ association. Min-E, in a closed confirmation also diffuses rapidly in the cytosol. Upon locality to Min-D, Min-E switches to a reactive state and binds with Min-D, displacing Min-C which dissociates back into the cytosol. When bound, Min-E triggers ATPase activity which causes Min-D to become ADP-bound and the Min-DE complex to dissociate from the membrane. As a result, Min-E is

responsible for clearing the mid-cell of Min-C, leading to polarised Min-D distributions at the ends of the cell. This process causes Min pole-pole oscillations where MinE clears Min-CD sequentially from polar regions. Min-C can only inhibit FtsZ above a threshold concentration. As the cell elongates, the concentration of Min-C at mid-cell eventually decreases. FtsZ is no longer inhibited and the cytokinetic ring can form, successfully splitting the cell into two equally sized daughter cells when in a rod-like geometry [35]. Interestingly, in-vitro studies of the Min system reveal that these protein waves are able to sense the longest polarisation axis and are quick to adapt to changes in membrane geometry [36].

Beyond division, polarity formation is able to define morphological and functional differences within cells. Neurons exhibit high levels of polarity which enables efficient information flow across the nervous system. In vitro, initially spherical neurons have been observed to extend lamellipodia in all directions before forming minor neurites. Symmetry is then broken when one neurite is selected to become an axon - extending at a rate much faster than the remaining neurites. This single axon is able to transmit signals across the cell to other neurons. These neurites become dendrites which through maturity form spines and synaptic contacts which in turn interpret signals from other neurons. In this manner, polarity formation ensures directed propagation of information across the neuron [37]. The polarisation of the neuron is considered to occur under a local-activation, long-range inhibition model whereby dendrite growth is inhibited in all but the selected axon which instead experiences local activation (fig. 1.3b). This selection is ensured through long-range Ca+ waves which propagate down the axon towards the cell body and inhibit dendrite growth through Rho kinase activity [38].

Finally, polarisation is crucial for cell motility. In an immune response, migrating neutrophils are the first defensive barrier to infection, working to efficiently destroy infectious microorganisms. In order to migrate, neutrophils must undergo front-rear polarisation in response to a chemotactic gradient, a process regulated by the family of rho GTPases: Rac, Rho and CDC-42. At the leading edge, Rac activity is enhanced which in turn promotes the polymerisation of actin monomers to F-actin, producing protruding

lamellipodia. Concurrently, at the rear-end of the cell, RhoA stimulates the formation of myosin filaments which cross-link with actin bundles forming a network that generates cortical tension and inhibits lamellipodia formation [39]. Through this polarisation, the cell can migrate only in the direction of the cue (fig. 1.3c). The action of the front and rear of the cell are linked through the activity of CDC-42 which works through a 'long-range' signalling pathway. Situated at the front of the cell, CDC-42 confines Rac activity to the leading edge whilst also amplifying Rac activity at the rear of the cell through interaction with the WASp effector protein [40]. As a result, mutant cells lacking CDC-42 are unable to undergo this directed motion, instead extending lamellipodia in all directions [41].

1.2.1 Pattern formation in the *C. elegans* zygote

1.2.1.1 The nematode *C. elegans* is a model species

The subject of this thesis is polarity formation in the *C. elegans* zygote, formation of which governs successful asymmetric division to the 2-cell state. The nematode possesses many desirable characteristics for biological study and as a result *C. elegans* is a model species for studying cellular pattern formation. The worm, approximately $1\,\mathrm{mm}$ in length is transparent and therefore readily imaged using microscopy [25]. The genome of *C. elegans* has been completely sequenced and utilising methods such as RNA interference, single-gene knockdowns enable investigators to probe redundancy and indispensability in cellular processes, revealing the governing biochemical networks behind cell functionality. Perhaps most appealingly, the rapid life cycle of the nematode is circa 3 days, providing good experimental supply which can be frozen for years without fatality [42]. Nematode populations are primarily self-fertilising hermaphrodites, with sexually reproducing males forming just 0.2% of the population [43]. Experimentally, this proves an advantage as genetic homogeneity across generations can be easily maintained. Additionally, genetic crosses can be introduced in a controlled manner through sexual reproduction. Crucially, whilst anatomically simple this model organism exhibits complex behaviours readily found in more sophisticated organisms. During development, the first two rounds of cell division in *C. elegans* are particularly reproducible, which makes them an excellent

candidate for study of cell polarity in the first instance.

1.2.1.2 The first asymmetric cell division of the *C. elegans* zygote

Fertilisation of the *C. elegans* zygote provides the cue through which the zygote breaks symmetry, initialising polarisation (see fig. 1.4). During fertilisation in the hermaphrodite worm, the oocytes are expelled into the spermatheca where they are fertilised by a sperm on the leading edge of the cell [44]. Combination with the sperm reanimates oocyte maturation, which was otherwise arrested in metaphase. Following the two subsequent rapid rounds of meiosis, the fertilised embryo experiences destabilisation of its cortex which produce both cortical and cytoplasmic flows [45]. The cortical flows, caused by the down-regulation of cortical tension near the position of sperm abuttal, produce transient 'ruffling' along the cortex. The direction of the flows follows the increasing tension gradient towards the site of the future anterior pole. Flows of this kind are a key component of polarity formation in the single cell - they provide the polarising cue for the polarity proteins and the direction of flow denotes the polarity axis [46]. The initial expulsion of the oocyte into the spermatheca provides a physical constraint on the orientation of the oocyte and thus the future designation of the posterior pole at the position of sperm entry [47]. The mechanical rearrangement of the cortex during this period of flow characterises establishment phase, where membrane bound polarity determinants undergo translocation in the response to flows. Clearance of the cortex in response to flows allows for subsequent binding of the otherwise cytosolic polarity determinants and resultant establishment of polarised domains. Recent work by Gessele et al. indicates a key role for the activation-deactivation cycle of polarity determinants in the stabilisation of the polarity axis along the long axis of the cell [48].

The sperm-derived centriole pair nucleate and divide in the oocyte, creating two centrosomes either side of the paternal pronucleus. Able to nucleate microtubules, the centrosome is able to generate directed pushing and pulling forces within the cell, reorganising cellular components [50]. The cell now enters prophase, thus indicating the start of mitosis ***I*** and the migration of the maternal pronucleus towards the paternal pronucleus [51]. The pronuclei then move toward the centre of the cell, the chromosomes condense

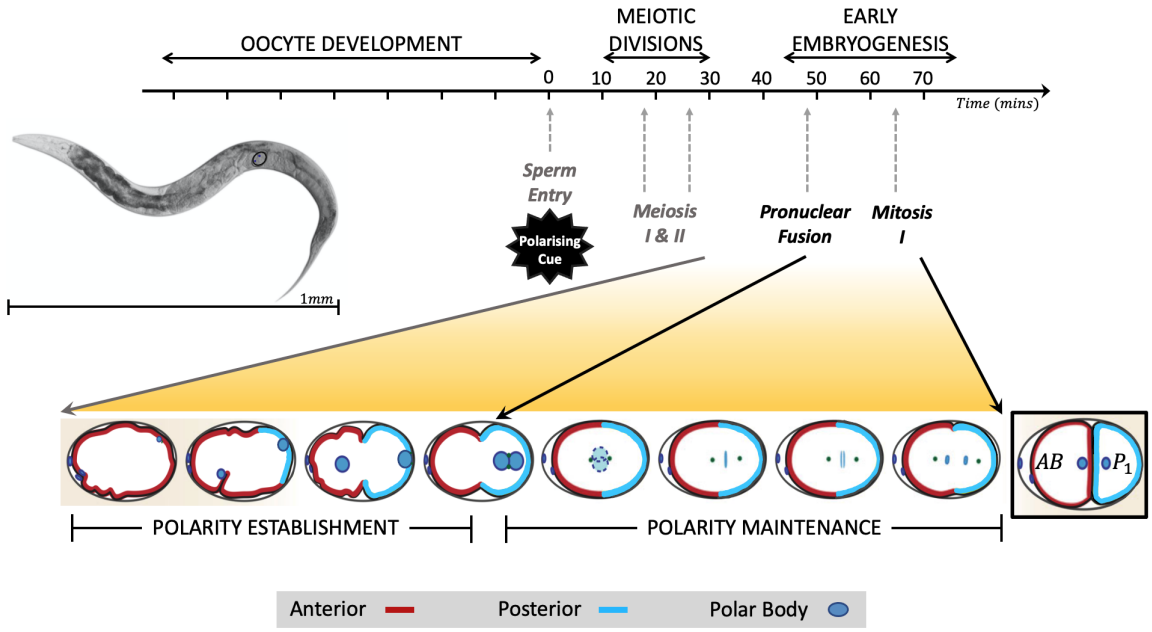


Figure 1.4: The first asymmetric division in the nematode *C. elegans*. Polarity formation in the *C. elegans* is initiated at the time of fertilisation of the oocyte. Two rounds of meiotic divisions are followed by cortical destabilisation and polarity establishment phase. Polarity determinants are rearranged by cortical flows leading the formation of distinct anterior and posterior domains. Pronuclear fusion signifies the transition into polarity maintenance phase. Mitosis *I* completes, resulting in the asymmetric division of the cell at the position of the domain interface. The initial cell division completes, producing a larger somatic *AB* cell and a P_1 cell that will continue to divide asymmetrically. Adapted from [49]. Image: Salk Institute.

and the nuclear envelope breaks down. Unbalanced pulling forces causes rotation of the mitotic spindle, aligning it with the anterior-posterior axis [52]. Metaphase ensues and the mitotic spindle migrates towards the posterior pole. The positioning of the mitotic spindle along the polarity axis denotes the location for cytokinesis and is highly precise within the embryo [53]. Around 5 min after nuclear-envelope breakdown the cell enters telophase and furrow ingression occurs at the bisection of the mitotic spindle. This furrow eventually cleaves, completing cytokinesis. In this way, asymmetric division gives rise to two daughter cells, a larger *AB* cell that continues to divide symmetrically giving rise to much of the ectoderm and a smaller P_1 cell that divides asymmetrically producing a further *P* cell and a cell that will trace different developmental pathways [25].

1.2.2 Polarity in *C. elegans*: the PAR proteins

Polarisation in the *C. elegans* zygote is governed by the conserved PAR (partitioning defective) proteins. Discovered by Kemphues and Preiss during a genetic screening, it was observed that mutant PAR zygotes exhibited defective phenotypes that resulted in the failure of asymmetric cell division [54]. During polarisation, the PAR proteins reorganise to form two distinct domains - dividing the cell into an anterior (front) and posterior (back) along its long-axis [55]. As a result of this partitioning effect, the PAR proteins are further grouped and referenced based on their localisation post-polarisation. The scaffold protein PAR-3, the adaptor protein PAR-6 and an atypical protein kinase aPKC represent the anterior PAR proteins (aPARs), whilst the posterior PAR proteins (pPARs) are composed of the RING protein PAR-2, the kinase PAR-1, the putative Rho GAP CHIN-1, and the tumour suppressor LGL-1 [56].

Polarisation by the PAR proteins is tightly coupled to the cell-cycle, with a sperm derived centrosome initialising the reorganisation of these otherwise homogeneously distributed proteins [49]. Prior to this cue, the anterior proteins occupy the membrane whilst the posterior PARs remain cytosolic. The sperm derived cue induces reorganisation of the acto-myosin cortex and its retraction away from position of abuttal. In this way, the membrane-bound anterior PAR proteins are redistributed towards one pole of the cell - creating the anterior domain. Clearance away from the position of sperm abuttal enables the cytosolic posterior PARs to bind to the cortex and form a posterior domain [45]. This phase of polarisation, when the pre-pattern for polarity is created is referred to as establishment phase [57]. Following establishment phase, the cell enters maintenance phase where self-organisation amongst the PAR proteins sustains domains before asymmetrically dividing in at the position of the domain interface. The asymmetrically localised PAR proteins then signal to downstream effector proteins which results in the unequal inheritance of other cell fate-determinants to each daughter cell [58].

1.2.2.1 Interactions within the anterior PARs

The scaffold protein PAR-3 contains a CR1 oligomerisation domain, a PDZ domain which allows it to form a complex with PAR-6 and a CR3 domain for association with aPKC

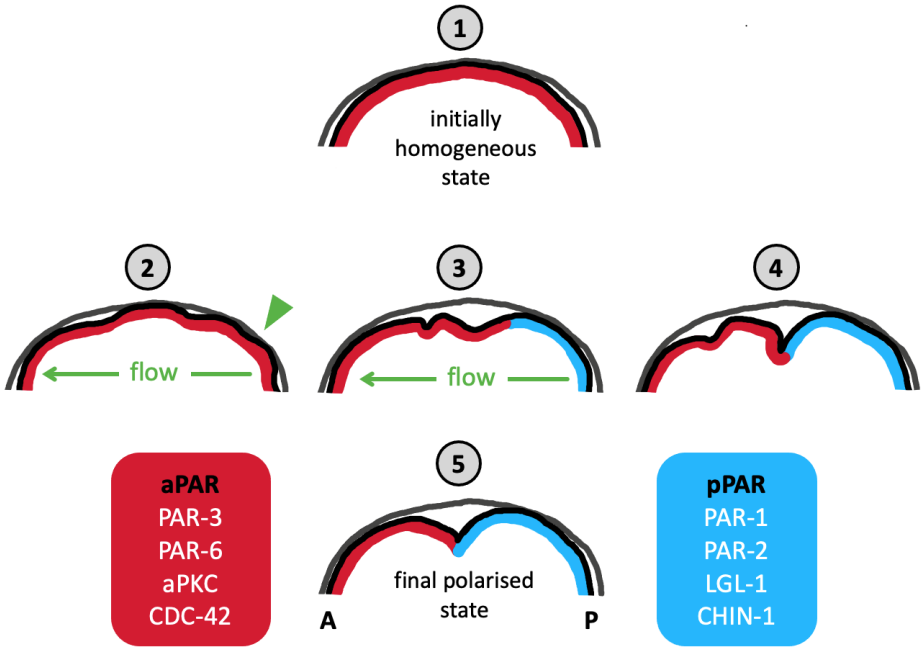


Figure 1.5: The PAR proteins redistribute to form domains. **(1)** The unfertilised cell is in an initially homogeneous, anterior dominant state. **(2)** Near the position of sperm abuttal (green arrow) the cortex destabilises and the inhomogeneity of the cortical tension produces cortical flows that translocate the membrane-bound anterior PAR proteins away from the site of fertilisation. **(3)** Clearance of the domain by cortical flows enables the cytosolic posterior PAR proteins to bind to the membrane. **(4)** The smooth posterior domain expands across the cell along the polarity axis. **(5)** The domain boundary is stalled in a final polarised state, the boundary of which denotes the site of cytokinesis.

[59]. Oligomerisation of PAR-3 has been shown to be indispensable for its localisation. Further, experimental observations in embryos where this oligomerisation is impeded show that PAR-6 also fails to localise, indicating a clear role for PAR-3 clusters in polarity establishment [60]. Mutant PAR-3 RNAi embryos fail to recruit PAR-6 and PKC-3 (aPKC) to the membrane, but cortical accumulation of PAR-6/aPKC does not require direct binding to PAR-3 [61]. The scaffold protein PAR-6 is able to form a heterodimer with aPKC due to their mutual possession of a PB1 domain which associates preferentially to either PAR-3 or the Rho GTPase CDC-42 in a cell-cycle dependent manner. CDC-42 is able to associate with the membrane independently, becoming anteriorly localised in the membrane during maintenance phase [62].

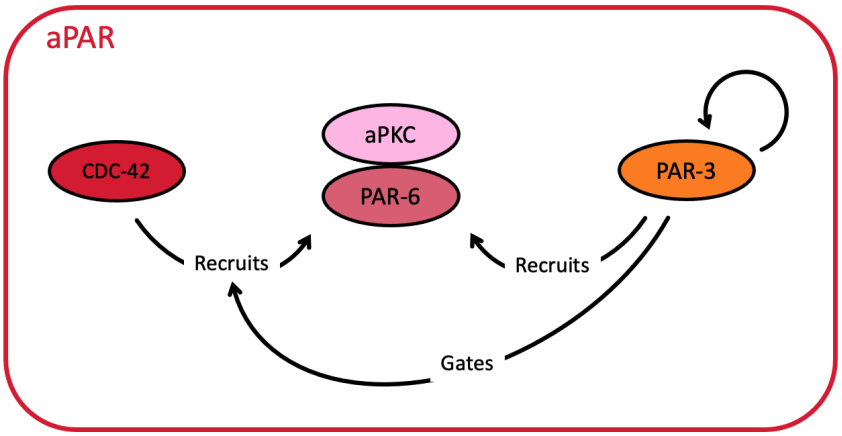


Figure 1.6: Anterior PAR components. The anterior PAR proteins consist of the Rho GTPase CDC-42, the scaffold proteins PAR-6 and PAR-3 and the atypical protein kinase aPKC. PAR-3 self-recruits to form oligomers that are indispensable for polarity establishment. PAR-6/aPKC heterodimers form a complex with both PAR-3 and CDC-42 in a cell-cycle dependent manner. The formation of these complexes is gated by PAR-3.

1.2.2.2 Interactions within the posterior PARs

PAR-2 contains a RING finger domain that allows it to stably associate with the cortex through lipid or microtubule binding [63]. The RING domain has been speculated to enable oligomerisation - similarly to the anterior PAR-3 species - and PAR-2 self-recruitment forms a positive feedback loop [56]. PAR-1 is a conserved serine/theronine kinase that binds to PAR-2 via its C-terminal domain [64]. The clustering CHIN-1 species becomes cortically localised during maintenance phase - an association with the cortex that is considered to be independent of the other posterior PARs [65]. Little is known about LGL-1, but experimental evidence points to a mechanism where LGL-1 acts redundantly to maintain polarity through negative regulation of the recruitment of myosin in the posterior domain [66].

1.2.2.3 Interactions between the anterior and posterior PARs

The PAR proteins diffuse freely across the cortex and therefore to maintain a polarised state, an important interaction in the PAR network is that of mutual antagonism between the opposing aPARs and pPARs. When polarised, mutual antagonism works to asym-

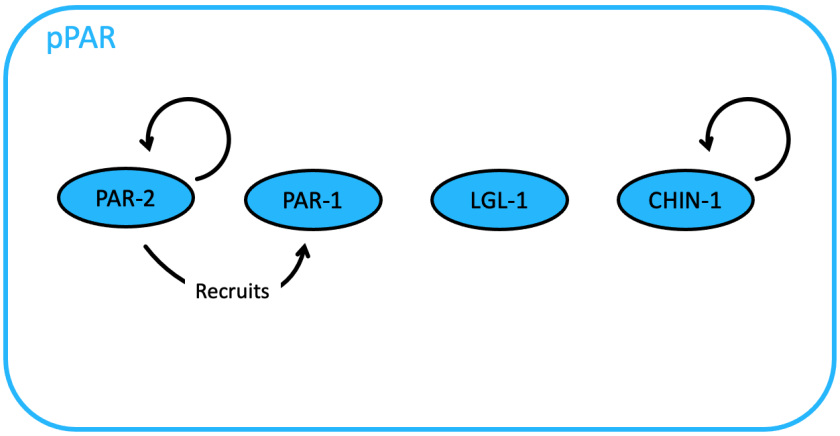


Figure 1.7: Posterior PAR components. The posterior PAR proteins consist of the kinase PAR-1 the RING finger protein PAR-2, lethal giant larva LGL-1 and the GTPase-activating protein CHIN-1. PAR-2 binds the membrane and self-recruits cytosolic PAR-2 in a process of positive feedback. PAR-2 then recruits PAR-1 to the membrane. LGL-1 binds to the membrane independently and is dispensable for successful polarisation. CHIN-1 has been observed to form clusters on the membrane which are able to sense cortical flows.

metrically modulate the membrane-affinity of the species thus maintaining a dominant concentration of a single PAR group, even in the presence of unbounded lateral diffusion. PAR-1, PAR-2, CHIN-1, LGL and aPKC all participate in this antagonistic reaction.

The mechanisms by which membrane affinity is modulated are diverse among the molecular players in the PAR polarity circuit, with many pathways acting redundantly to control localisation of PAR proteins within the cell [56]. During maintenance phase, PAR-2 works to inhibit posterior localisation of NMY-2 thus polarising the acto-myosin cortex, preventing posteriorly directed cortical flows and expansion of the anterior domain [67]. In this manner, PAR-2 maintains PAR-6/aPKC asymmetry by upregulating preferential loading of this complex in the anterior. Loss of asymmetry in PAR-2 mutant embryos can be rescued through the over-expression of LGL, which is considered to regulate the overall concentration of PAR-6 within the zygote [66]. PAR-2 recruits PAR-1 to the membrane, which in turn controls PAR-3 levels by upregulating the dissolution of PAR-3 clusters during maintenance phase [64]. PAR-3 is considered to gate PAR-6/aPKC levels on the membrane and further regulate the association of this heterodimer to active CDC-

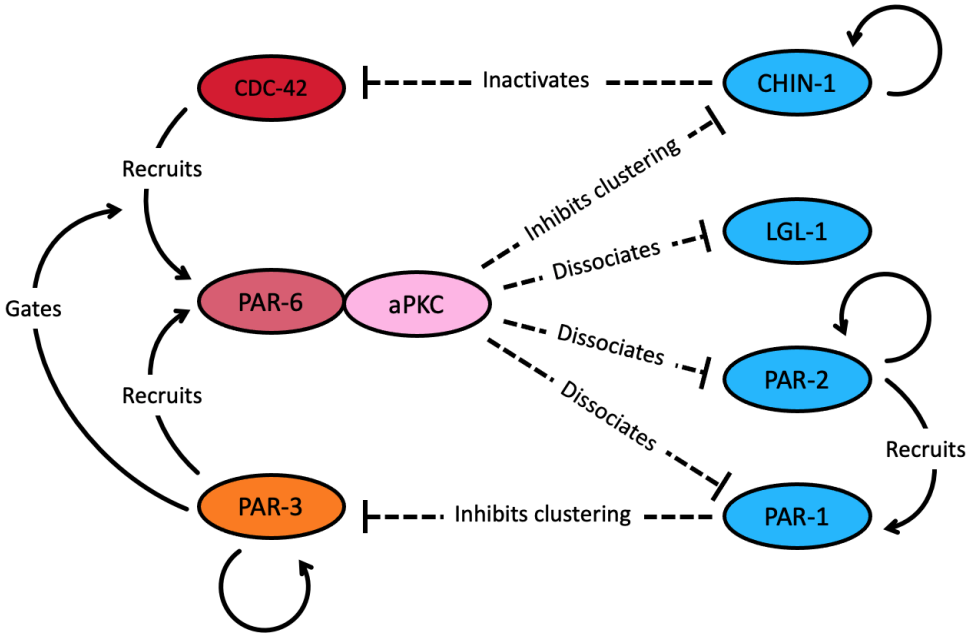


Figure 1.8: Mutual antagonism underpins polarity of the PAR system. The anterior and posterior PAR proteins are linked by a complex network of mutually antagonistic reactions. Active aPKC promotes the dissociation of the posterior proteins LGL-1, PAR-2 and PAR-2 and inhibits CHIN-1 oligomerisation. CHIN-1 acts redundantly to inactivate CDC-42. PAR-2 recruits the kinase PAR-1 which inhibits the oligomerisation of the anterior PAR-3 species. Together the coupled negative feedback loops result in local self-amplification within polarity domains, maintaining the polarity pattern. Adapted from [56].

42. CHIN-1 clusters promote local inactivation of CDC-42, confining CDC-42 activity to the anterior pole. The activity of aPKC is indispensable in maintaining the anterior domain, working to phosphorylates PAR-1, PAR-2 and LGL. Further, aPKC activity regulates the growth of CHIN-1 clusters, completing a negative feedback loop between CHIN-1 and the CDC-42/PAR-6/aPKC heterodimer. The coupled negative feedback loops between the anterior and posterior PARs promote local self-amplification within each domain, enabling the self-organising network to maintain the polarity pattern.

1.2.3 Ensuring successful polarisation in *C. elegans*

Polarisation in the single cell is a process that underpins the blueprint for life. The initial demarcation of head from tail results in spatially localised signals from which downstream determinants take their cues. In developmental processes, the accuracy of this pre-patten

is therefore tantamount, with errors in patterning resulting in grave consequences for the biological system. To ensure reproducibility of phenotype, the biochemical networks that oversee development must be robust - to maintain a characteristic output in the presence of variation in the environment [68]. Common features to enhance robustness in a biological system include redundant or degenerate reaction pathways to ensure fault tolerance and coupled feedback loops to enhance system stability [69].

In the *C. elegans* zygote, polarisation is initialised by a transient external cue before self-organising to form a stable pattern that denotes the future site of cytokinesis. Bookended by cell fertilisation and cell division, polarisation is tightly coupled to the cell cycle [49]. To pattern successfully the polarity network must be sensitive to perturbation by the polarising cue whilst also retaining system controllability. Importantly, the cell polarises only once a perturbation threshold has been reached [70]. It has been shown that contractility levels of the cellular cortex must remain high in order to sustain the cortical flows for a substantial period. In this way, the cell overcomes the 'barrier to polarisation' which exists to ensure that the cell does not spontaneously polarise [71]. The presence of an energetic barrier ensures temporal control of polarisation.

The PAR polarity system moves from a cue-guided to a self-organised state as the cell enters maintenance phase [71]. As polarisation progresses, the localisation and prominence of individual PAR components varies spatio-temporally. For instance, PAR-3 is upregulated during establishment phase with the period of cluster enhancement correlating with the period of cortical flows. PAR-6 is closely localised with PAR-3 clusters during this cue-guided period [60]. PAR-3 clusters are then down-regulated during maintenance phase where PAR-6 dynamics instead appear more diffuse [72]. This compositional variation in the cell in line with distinct phases of polarisation indicates a mechanism by which the cell ensures robustness of polarisation through specialisation of function. Uncovering the design principles of a biochemical network that would allow for such temporal plasticity whilst demonstrating robust polarisation is the general aim of this thesis.

1.3 Motivation and approach

In this thesis, we look to uncover design principles that underlie the biochemical network that governs polarity in the *C. elegans* zygote. Significant research illuminating the localisation and temporal dynamics of the PAR polarity proteins has been undertaken which offers a wealth of information as to their individual function and interaction redundancies [73]. Recent interest has been drawn to the clustering species, PAR-3, as one of the key players in polarity development in *C. elegans* [60][74][75]. PAR-3 has been shown to respond to flows through establishment phase, with clusters increasing in both number and intensity during this time [60]. Embryos lacking PAR-3 lack cortical flows and are thus unable to localise other anterior proteins, indicating that PAR-3 function is indispensable for polarisation [76]. In this thesis we consider the role of PAR-3 clusters in robust polarisation: in the context of cue-sensitivity during establishment phase and as part of an antagonistic feedback loop that contributes to stable polarisation. Both oligomerisation and mutual antagonism are examples of positive feedback loops that reinforce pattern formation. PAR-3 is implicated in both these behaviours and so the elucidation of the design principles underpinning a model of cell polarity which focusses on PAR-3 dynamics is key to gaining a fundamental understanding of successful polarisation in the *C. elegans* zygote.

In the first section of this thesis we probe the *in-vivo* dynamics of PAR-3 clusters during establishment phase. The significance of the upregulation of PAR-3 clusters and the relation of this process to cortical flows remains unclear. Oligomerisation is an example of positive feedback which would provide the cell with a mechanism by which to amplify its response to the polarising cue. We therefore analyse PAR-3 cluster dynamics from the perspective of PAR-3 oligomerisation enhancing sensitivity to cortical flows: do larger PAR-3 clusters flow more efficiently? We utilise methods from image analysis to quantify the response of PAR-3 clusters on both a local and global scale. Importantly, insights into the behaviour of PAR-3 clusters informs our modelling approach used to consider possible biochemical networks for the anterior PAR proteins.

To maintain and stabilise polarised domains, the anterior and posterior PAR proteins

undergo mutual antagonism. Experimental observations evidence that antagonism acts differentially between elements of the PAR polarity network [56]. Interestingly, PAR-3 has been shown to inhibit aPKC activity thus rendering the PAR-3 complex a target of posterior antagonism, yet unable to reciprocate in this interaction [77]. As a gatekeeper to polarisation of the anterior proteins, understanding the design principles and temporal control of a polarisation network whose success hinges on a complex vulnerable to antagonism is crucial to understanding patterning strategies in development.

Cross-talk in biochemical networks coupled with the hierarchical nature of redundant biochemical interactions can render mechanistic, rather than causal insight difficult to decode when studying the system *in-vivo*. Additionally, significant perturbation of the zygote *in-vivo* frequently results in cell fatality, limiting the suitability of 'wet' lab experiments in assessing the limitations of possible network design. To overcome these limitations, we approach the assessment of possible polarity networks with the tools of computational systems biology.

The anterior PAR system has been observed to switch between an advected, inactive state during polarity establishment and a diffuse, active state during polarity maintenance [78]. How control of switching is embedded into the biochemical network design of the polarity network remains unclear. Recent hypotheses point to the cycling of aPKC between functionally distinct molecules as a model for polarity switching and control. In this thesis we probe two possible networks design that encompass the aPKC cycle and simulate our models using a reaction-advection-diffusion framework. We utilise sensitivity analysis to assess the characteristics of polarisation in our functionally distinct hypothesised models of polarisation. Unlike previous models of polarity, we probe both establishment and maintenance phase and consider the different dynamics of the anterior proteins.

In biological systems, trade-offs between system complexity, fragility and resource allocation render it imperative to consider the overall robustness of additional elements of resource complexity [79]. To this end, we compare robustness of polarisation in the extended PAR polarity models with that of a simpler network design. We assess robustness

by implementation of Approximate Bayesian Computation. An interdisciplinary project, we model with an experimentally guided perspective, choosing biologically viable parameterisations and selecting biochemical interactions that remain faithful to observations *in-vivo*. At this interface, we gleam fundamental mechanistic insights through perturbation of networks that would otherwise prove intractable in the wet laboratory. We contribute to the understanding of polarising networks and hope that our findings inform *in-vivo* experiment designs of the future.

Chapter 2

PAR-3 cluster dynamics as a result of interaction with the cortex

Polarity development consists of two distinct phases: an initial establishment phase followed by a stabilising maintenance phase. During establishment phase symmetry is broken, and membrane-bound components undergo spatial reorganisation. While it is possible for symmetry breaking to occur spontaneously, timely polarity establishment relies upon advective triggering in the form of cortical flows [70]. Throughout establishment phase, advective motion translocates membrane-bound PAR proteins toward the anterior pole. This spatial reorganisation initialises the patterning template that is maintained when flows cease. As such, the ability for the PAR proteins to sense and respond to the advective trigger is indispensable for successful polarisation on a biologically viable time-scale.

In this chapter we explore the relationship between the PAR proteins and cellular flows, taking a focus on the clustering PAR-3 species and its role in efficient segregation of the anterior PAR proteins to the anterior pole. Firstly, we introduce the reader to the biological make-up of the cellular cortex and its physical properties. We next move to describe the complex network of self-regulating reactions that link both the cellular cortex and the PAR proteins. An overview of previous works that characterise cellular flows as a result of changes in cortical tension is presented. Finally, we explore the role of PAR-3 clusters in successful polarity establishment. We investigate the relationship between

cluster size and efficiency of translocation, as well as quantifying PAR-3 movement on both a local scale and globally along the polarity axis. Through this, we assess the suitability of recent competing perspective as to the functional role of PAR-3 clustering: oligomerisation as a positive feedback loop that acts to enhance clustering, enabling PAR-3 to better sense flows, or clustering as a by-product of mechanical forces experienced through coupling to the dynamic cortex.

2.1 Biological Background

2.1.1 The cellular cortex is a dynamic, complex structure

Sitting just beneath the plasma membrane the cellular cortex provides a structural framework to this otherwise fluid-like lipid bilayer and so controls the development of cell shape [80]. The cortex is a complex and dynamic structure consisting of many diverse sub-components, including actin filaments, myosin motors, bundlers and cross-linkers. Acto-myosin structures are the framework of the cortex. Embryos under high-levels of acto-myosin inhibitors, such as Latrunculin A or the myosin light chain kinase inhibitor ML-7, have been observed to suffer a complete collapse of their plasma membrane structure [81].

In contrast to actin filaments within muscle sarcomeres, which are highly ordered, actin filaments within the cellular cortex form a dense, disordered meshwork (see fig. 2.1). Filamentous actin is a helical assembly, comprised of globular subunits that are approximately $5nm$ in length. These protein subunits bind in a head-to-tail arrangement, forming a polarised actin filament [82]. This dynamic structure undergoes a series of nucleation, lengthening, branching, bundling and buckling events; all of which are controlled by actin-binding proteins[83] [84].

As a consequence of stochastic depolymerisation and buckling events, the fine actin filaments are arranged heterogeneously within the cortex structure. Bundlers arrange actin filaments into thicker parallel or orthogonal architectures and these higher-order structures are further remodelled by bipolar NMY-2 (non-muscle myosin) motors [85]. A motor will bind to and move along the actin filament in a directed motion towards the

barbed end of the actin filament. As a result of binding, the motor forms cross-bridges between actin filaments, enabling the motor to reorganise actin filaments with respect to each other [86]. Together, these hierarchical sub-structures within this thin contractile layer form a dynamic framework whose organisation dictates the physical properties of the cortex. Continual turnover of cortex architecture modulates its mechanical properties throughout the cell-cycle. Its plasticity is a fundamental feature which allows it to modulate these properties on a local scale, permitting a multitude of morphological processes [87] [88]

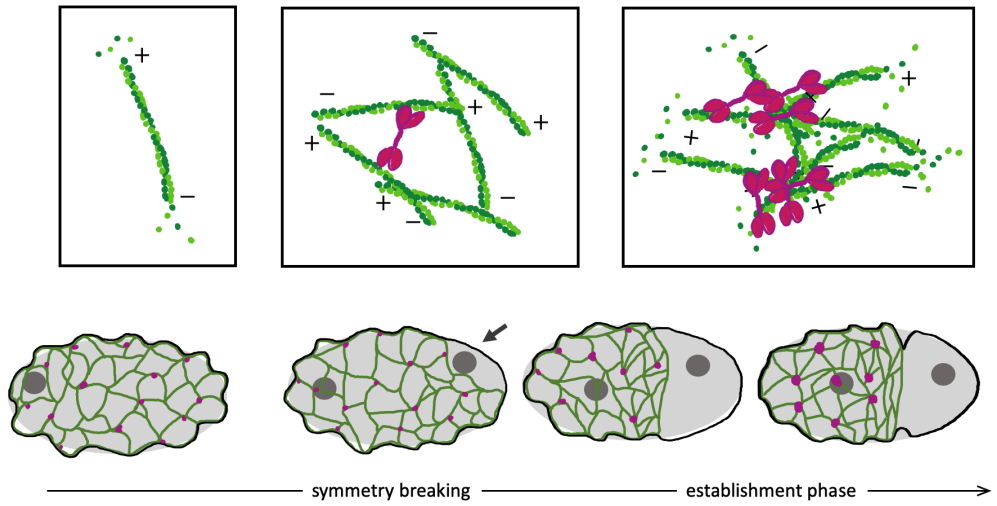


Figure 2.1: Cortical flows are coupled to reorganisation of the acto-myosin cortex. (Top, L-R) The cellular cortex is composed of polarised actin filaments (green) that lengthen, branch and buckle. Filaments are dynamically reorganised by myosin motors (pink) whose heads bind to and traverse along the filaments in a polarised manner. The acto-myosin cortex can restructure to form a dense interconnected network interspersed with myosin foci. **(Bottom)** The initially uniform cortex is destabilised in the region proximal to sperm abuttal. This causes anisotropy in cortical tension which results in directed cortical flows and recendence of the cortex to the anterior pole. During this establishment period, myosin foci (pink) become denser and more sparsely distributed.

The control of these mechanical properties is largely overseen by the activity of both myosin motors and crosslinkers. Towards the end of meiosis II, Mayer et al. reported NMY-2 is uniformly arranged across the entire cortex, presenting as both a filamentous network and connected dense foci. Through observation of GFP tagged NMY-2,

Munro et al. reported that foci appear and enlarge over time through the coalescence of smaller filamentous components. Myosin foci display contractile behaviour that is coherent throughout the network, manifesting in surface invaginations first observed by Hird et al. The coherence of foci pulsation indicates that the network is mechanically coupled and under active tension [45], the origin of which is directly attributed the action of myosin motors and crosslinkers on the actin meshwork. Both myosin motors and cross-linkers are only weakly connected to filamentous actin, enabling the system to respond to mechanical stresses and dynamically remodel. The myosin motors have the ability to produce both extension or contraction within the bound actin filaments, depending on the proximity of the motor to the barbed end of the actin filament. Whilst this process occurs with no intrinsic bias, overall, the cortex has a bias towards contractile motion. Individual actin filaments have a persistence length of $10\,\mu\mathrm{m}$ and so can withstand cortical tension. However, in the presence of myosin motors, the actin filaments have a critical length of $0.3\,\mu\mathrm{m}$ and so undergo stochastic buckling events [84]. This buckling behaviour is considered to be the origin of the contractile bias across the acto-myosin network, a characteristic considered to be indispensable in the propagation of long-range cortical flows [89][90]. Myosin motors exert stresses on the network: whilst close to the pointed end of the actin filament they are tensile, close to the barbed end these stresses are compressive. In the presence of the compressive forces exerted by the myosin motors, the filamentous actin buckles and the cortex contracts. In vitro, Bendix et al. observed that at a fixed F-actin concentration, contraction only occurred beyond a threshold myosin concentration and only within a narrow range of cross-linker concentrations [91]. In the presence of myosin motors, Ding et al. also realised a non-monotonic relationship between cortex contractility and the concentration of cross-linkers. Quantifying these findings through simulation it was found that as the number of connections in the network increases, contractility also increased until a threshold was reached, beyond which contractility was impeded. At this threshold cross-linker concentration, the number of connections in the network is abundant and as a result the network becomes stiff and resistant to deformation [92]. Contractility is favoured at optimal levels of connectivity, enabling the cortex

to propagate forces. These results indicate that the cross-linking of filamentous actin is the fundamental mechanism that allows for the propagation of forces across the cortex.

Able to undergo stress relaxation, the cortex is responsive to forces within the network and is therefore able to tune force transmission [88]. The presence of anisotropies of active tension within the cortex results in both local and long-range material flows [93]. The mechano-chemical properties of the cortex define the ability of the cortex to fulfil its role in many developmental processes, for example the propagation of long-range flows for successful polarity establishment. Severson et al. showed that in the case of the *C. elegans* zygote, the formation of cortical actin microfilaments is highly dependent on the actin-binding profilin, with mutant zygotes exhibiting diminished cortical flows and failing to undergo successful polarisation. The observed reduction in cortical flow speeds were similarly recognised in embryos treated with microfilament depolymerising drugs [94], indicating a key role for cortical architecture in efficient translocation of substances along the embryo. Through deletion of plastin, Ding et al. perturbed the activity of crosslinkers effectively reducing the connectivity of the actin meshwork. Through establishment phase, the group no longer observed the formation of dense myosin foci reported by Mayer et al. and observed that cortical flows were weakened [92]. Together, these results highlight the importance of cortical architecture in deriving the mechanical properties of the cortex leading to functionality, for example the propagation of long-range flows that have been illustrated to be indispensable for the translocation of membrane proteins in polarity establishment.

Computational modelling of acto-myosin dynamics has been implemented to further distil the mechanistic origins of cortical reorganisation observed *in-vivo*. Luo et al. modelled the cellular cortex as a contractile coherent network encapsulating actin filament polymerisation, cross-linkers and NMY-2 driven filament sliding. The contractile action of the myosin motors resulted in actin asters becoming densely enriched towards a single point; a result that could be recapitulated in experiment through applications of high concentrations of the actin-monomer-binding drug Latrunculin A. Together, the growth of actin filaments, the stabilisation of actin asters through cross-linking and their ran-

domised movements through myosin activity faithfully reproduced patterning effects seen in experiment [95].

2.1.2 Cellular flows arise as a result of mechanical forces in the acto-myosin cortex

Cortical flows are a key component in establishing cell polarity, breaking symmetry within the cortex and reorganising membrane components. Prior to fertilisation, NMY-2 (non-muscle myosin) foci are distributed isotropically throughout the acto-myosin cortex. At the position of sperm abuttal, the sperm MTOC acts to disrupt local contractility and focus formation, endowing the system with a polarising asymmetry. As a result, the formation of new NMY-2 foci is immediately inhibited in the region proximal to the sperm MTOC. There is a relaxation of cortical tension in the posterior pole and existing foci move away from the MTOC toward the anterior pole. Migrating away from the sperm MTOC, NMY-2 foci continue with their coherent pulsating dynamics, giving rise to visible cortical 'ruffling' [96]. Comparatively, the non-contractile posterior zone is smooth in appearance. Small filaments within this zone coalesce only at the anterior-posterior boundary and move to narrow the egg circumference leading to pseudo-cleavage [45].

There has been significant research evidencing that disruption of the cellular cortex and hence obstruction of both chiral and polarity driving flows results in unsuccessful polarisation and cell development. Munro et al. observed that in embryos depleted of the spindle protein spd-5, and therefore lacking a functional centrosome and the associated ability to nucleate microtubules, the characteristic NMY-2 foci patterning was not observed. In early pseudo-cleavage, Hill and Strome disrupted microfilament growth observing polarity and patterning defects in subsequent development [97]. Similar perturbations, by treatment of the microfilament inhibitor cytochalasin D, were carried out by Hird et al. who directly observed that microfilament inhibition disrupted cortical flows and resulted in embryos being unable to complete pseudo-cleavage and divide normally [96].

Initiated by the sperm-donated cue, the polarisation of cortical tension has long

been hypothesised to be the functional mechanism that gives rise to flows in the cortex [80]. Modelling the cortex as a thin-film active fluid, Mayer et al. moved to quantify the relationship between cortical tension of cellular flows in vivo, demonstrating that the cortex must be sufficiently viscous in order to support long-range flows [98]. Through laser ablation, they investigated tension in the cortex both parallel and orthogonal to the anterior-posterior axis. It was found that in the NMY-2 enriched anterior domain, cortical tension in the direction orthogonal to the anterior-posterior axis was nearly double that of the posterior domain. Under treatment of spd-5, myosin remained enriched throughout the cortex and cortical tension was equalised across the cortex, revealing observation alike those of Munro et al. Further, it was found that in the direction parallel to the polarity axis, cortical tension was much weaker than its orthogonal counterpart. On the contrary, in mutant spd-5 (RNAi) embryos which lack the ability to break symmetry, tension was found to be isotropic. This indicated that the underlying properties of the cortex were indeed isotropic and that tension anisotropy arose as a result of cortical flows.

Myosin activity closely regulates all flows arising within the cellular cortex. In 2014, Naganathan and colleagues investigated chiral cortical flows that acted orthogonally along the anterior-posterior axis, counter rotating the anterior and posterior domains. Upon RNAi of the myosin regulatory light chain (mlc-4), myosin activity was disrupted and a reduction in velocity of the chiral counter rotating flows was observed. It was found that myosin activity produced active torques and coupled with the myosin gradients along the anterior-posterior axis, this gave rise to a counter-clockwise flow in the posterior cortex [99]. Parallel to the anterior-posterior axis, Mayer et al. measured that polarising cortical flows are at a peak velocity of $7.66(100)\,\mu\mathrm{m\,min}^{-1}$. The position of this peak flow was observed in the posterior region of the cell and decreased along the axis towards the anterior pole, implying the cortex is under compression [45]. Through fluorescent tagging of actin, Reymann et al. observed that after cortical flows had ceased, the actin filaments aligned circumferentially at the position of ingression where pseudo-cleavage and cytokinesis will occur. Alike in the work of Salbreaux et al., the cortex was modelled as a thin film of active fluid, and through comparison with experiment it was concluded

that this filament alignment is attributed to a peak compression rate due to cortical flows along the anterior-posterior axis [100], [99]. Further, modelling the cortex as a coupled phase-field model Aras and colleagues demonstrated that the depth of the pseudo-cleavage ingression was governed by the balance of contractility arising between the cross-linked and aligned acto-myosin. In turn, the depth of the furrow-ingression determined the time of polarisation [101]. Taken together, these results provide evidence of the positive-feedback loop between acto-myosin architecture and cellular flows, the interactions within which exert spatio-temporal control over polarisation in the cell.

2.1.3 Feedback between the cellular cortex, its regulators and the PAR proteins

Reorganisation of the cortex produces mechanical asymmetries across the cell. These asymmetries produce cellular flows which localise the PAR proteins and therefore cortical reorganisation is a key process in polarity formation. As a result of acto-myosin inhomogeneity, at the end of establishment phase the posterior domain is non-contractile, and the anterior domain contractile. This contractile polarisation of the cortex occurs in a congruent fashion to the polarisation of the PAR proteins, evidencing an association between the two processes [102].

Regulation of contractility during establishment phase is controlled through kinase activation, mediated by the small GTPase Rho. Initially uniform on the cortex, RhoGEF ECT-2 catalyses the dissociation of Rho from GDP, freeing the small GTPase to bind to GTP where it activates. In its active form, Rho is then able to promote the assembly of contractile acto-myosin filaments. Concentrated by the sperm centrosome, the activity of AIR-1 in the posterior works to stimulate GTP hydrolosis of the active Rho GTPase, inhibiting contractility [103] [104]. Inhibition of contractility in the posterior results in asymmetric pulling forces and the receding of the contractile acto-myosin network toward the anterior pole (Jenkins). The migration of NMY-2 correlated with the formation of the posterior domain [105]. Embryos that were unable to clear NMY-2 from the posterior resulted in cytoplasmic PAR-2, evidencing that clearance of the contractile network in this way allows PAR-2 to bind in the posterior. As a result, AIR-1 is considered a localised

polarising cue [104][106]. A schematic detailing the proposed mechanism by which the sperm polarises the cortex can be found in fig. 2.2.

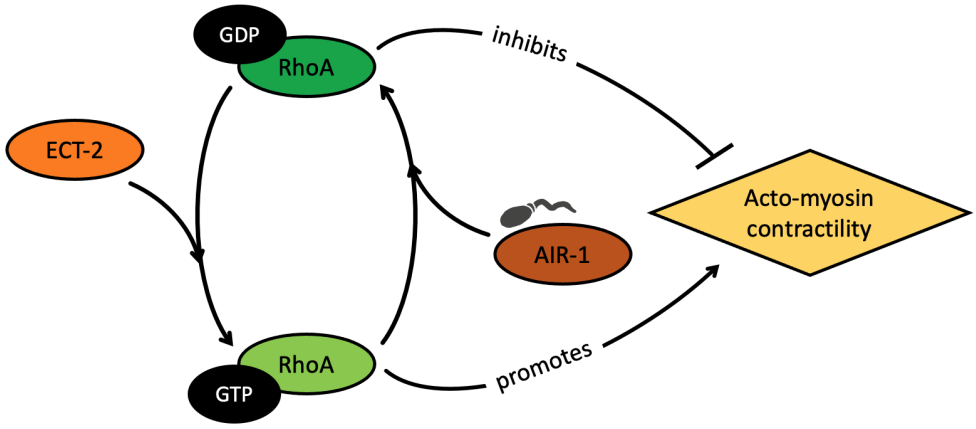


Figure 2.2: Activity of the small GTPase Rho regulates contractility The Rho GTPase switches between an active and inactive state. In the active, GTP bound form, Rho promotes cortical contractility. In the inactive, GDP bound form contractility is inhibited. AIR-1 is concentrated by the sperm-derived centrosome and inhibits Rho activity, inhibiting contractility. In turn, the RhoGEF ECT-2 catalyses dissociation of Rho and GDP, promoting contractility.

Perturbation experiments have evidenced essential roles for ECT-2 and RHO-1 in the control of polarity establishment. As reported by Shonegg and Hyman, depletion of these contractility regulators results in embryos that were unable to complete acto-myosin reorganisation processes and polarise effectively [105]. It was observed that embryos lacking RHO-1 and ECT-2 exhibited NMY-2 defects: NMY-2 foci were smaller with no interconnections, resulting in a non-contractile cortex. Similar results were reported in the work of Motegi et al, with ECT-2 (RNAi) and RHO-1 (RNAi) embryos lacking cortical ruffling and posterior smoothing. In the RNAi experiments of Jenkins and colleagues, the inactivation of ECT-2 produced domains where PAR-6 and PAR-3 were improperly localised across the cortex, likely through improper segregation by flows [107].

A key role of RHO-1 is that of anterior localisation of a key downstream effector of polarity development; the GTPase CDC-42. Unlike the observed phenotypes of RHO-

1/ECT-2 RNAi experiments, embryos lacking the cell division control protein CDC-42 remain able to produce cortical contractions, exhibiting both cortical ruffling and posterior smoothing. Therefore, whilst RHO-1 and ECT-2 play an important role in regulation of the actomyosin cortex, it is instead considered that the rho GTPase CDC-42 acts differentially to control polarisation [108]. Whilst able to recapitulate the characteristic patterning of myosin foci during establishment phase, it was found in CDC-42 RNAi embryos that the NMY-2 at the anterior cap was unstable, with bright foci moving back towards the posterior during pseudocleavage regression [105]. As such, CDC-42 activity is required for the stability of the anterior acto-myosin cap. Notably, CDC-42 also appears to form a positive feedback loop, promoting ECT-2 enrichment which in turn enhances its local concentration [108].

Of particular interest to this thesis, the GTPase CDC-42 has been shown to be indispensable for proper PAR segregation, playing a particularly important role in localising a well-documented complex comprising PAR-6/PAR-3/CDC-42 [109]. Aceto et al used to show that the CRIB domain of PAR-6, that which interacts with CDC-42 is crucial to maintain high-levels of PAR-6 asymmetry during maintenance phase [62]. Through establishment phase, embryos with reduced CDC-42 activity are unable to clear PAR-2 from the cortex. Schonegg and Hyman showed that the PAR-2 localisation defects seen in CDC-42 RNAi embryos arise as a result of PAR-6 being unable to localise on the cortex and without PAR-6 present on the membrane, there is no antagonistic partner present to maintain PAR-2 polarity [105]. However, localisation of PAR-6 to the cortex during establishment phase is not dependent on CDC-42. Rather it has been hypothesised that the contractility modulating PAR-3 complex is instead necessary for efficient PAR-6 localisation during this earlier stage of polarisation [110]. Using depletion by RNAi, Gotta and colleagues observed that, similarly to rundown of ECT-2, in the absence of CDC-42 the anterior PAR-3 failed to properly localise in the cortex [111]. In PAR-3 RNAi mutant embryos, Munro et al. observed attenuated flows of NMY-2 during establishment phase and improper segregation of PAR-6. These results show that PAR-3 directly interacts with the cortex, modulating its architecture to promote its own transport. The crucial

role of PAR-3 in polarity establishment has been widely investigated, details of which are discussed in detail in the upcoming sections. The interaction of PAR-3 and cortical flows form the investigative basis for the first part of this thesis.

2.1.4 The role of the scaffold protein, PAR-3

Able to respond to flows within the cortex, the scaffold protein PAR-3 plays a fundamental role in the effective localisation of other membrane-bound anterior proteins. A key feature of the PAR-3 makeup is its N-terminal conserved region, CR1, which allows it to undergo multivalent interactions and homo-oligomerisation [112]. Whereas high valence interactions such as those seen in the formation of the cytoplasmic p-granules undergo a phase-transition process, the low valency interactions that are undergone via the CR1 domain instead favour the formation of clusters of a finite size [113][114]. The presence of oligomeric PAR-3 on the membrane is observed as membrane puncta, with cluster size and number becoming upregulated during establishment phase of polarisation [60]. Through interactions with the acto-myosin membrane, the anterior PARs amplify their effective localisation in a positive feedback loop. This relationship has recently been delineated in the work of Wang and colleagues, who highlight a key role for the cortex in remodelling the PAR proteins by means of cortical clustering. Alike previous work, it was observed that the majority of membrane localised PAR-3 was present in the form of clusters, which enhanced in size through establishment phase. Notably, once cortical contractions cease, the PAR-3 clusters decrease in both number and intensity. Utilising spinning-disk-confocal microscopy the group observed that NMY-2 foci did not co-localise with PAR-3, indicating that PAR-3 must instead interact indirectly with the acto-myosin cortex. Goehring et al provide further evidence for this indirect interaction, finding that PAR proteins remain localised on the cortex even when actin is depolymerised [115]. Inhibition of the NMY-2 contractility through application of blebbistatin gave rise to a PAR-3 cluster population that was reduced in both intensity and number. To increase cortical tension a hypotonic buffer treatment was then applied to cells, and the number and intensity of PAR-3 clusters grew thus indicating a direct link between the physical properties of the acto-myosin cortex and the control of PAR-3 cluster formation [72].

Implementing a single-cell biochemistry approach, Dickinson et al. quantified the size and distribution of PAR-3 clusters during establishment phase. Utilising microfluidics and pull-down assays they noted an indispensable role for PAR-3 cluster formation in sensing cortical flows. Dickinson et al. found that bright PAR-3 clusters exhibited directed motion along the cortex. Whilst all PAR-3 clusters exhibited biased motion toward the anterior, dimmer clusters were not observed to undergo strong directed motion as they were limited by their shorter membrane lifetime [60]. As clusters increase in size, they become increasingly spatially localised due to their decreased motility which works to strengthen PAR-3 anterior localisation as the protein is less able to diffuse away from the anterior pole. Wang et al hypothesised a 'clustering and stabilisation' model, whereby cortical clusters enhance advection by flow and reduced membrane turnover increases the levels of spatial information for downstream binding events. Segregation of PAR-3 to the anterior is upregulated by the inhibitory kinase action of the posterior PAR-1. In wild-type embryos during maintenance phase, Sailer et al. observed that PAR-3 clusters were anteriorly localised, with weak signalling of single-molecule PAR-3 in the posterior. However in PAR-1(RNAi) embryos, clusters were sparsely distributed indicating that PAR-1 could inhibit PAR-3 oligomerisation [65]. Discussed further in section 4.1, a reactionary network of this kind was modelled by Dawes and Munro, who found that PAR-3 clustering coupled with PAR-1 antagonism is sufficient to maintain polarity and concluded that PAR-3 clustering acts to stabilise polarisation in the embryo [116].

2.1.5 Open Questions

PAR-3 clustering is a requisite for proper localisation of the anterior PAR proteins [60]. Oligomerisation is an example of a positive feedback - a motif of patterning networks that enhances sensitivity to a patterning cue. In the context of polarisation of *C. elegans*, this patterning cue is the cortical flows that arise as a result of symmetry breaking in the acto-myosin architecture. Acto-myosin flows are coupled to physical contraction of the cortex and as a result, proteins embedded in the cortex are susceptible to the mechanical forces arising from flows. As shown by Wang et al., PAR-3 clustering is indirectly enhanced when cortical tension increases. This leads us to question - can local compression

enhance PAR-3 clustering also? Alternatively, as proposed by Rodriguez et al., larger PAR-3 clusters, like large sails in the wind, may be more efficiently translocated by flows in their environment due to their increased size. Theoretically, larger clusters would be more closely coupled to the cortex and as a result would be able to 'sense' cortical flows better. Alternatively, like a stone in a river, their increased size may instead impede advection by flows [78]. The first section of this thesis aims to address these alternate perspectives on the relationship between PAR-3 cluster formation, enlargement and cortical flows present during polarity establishment phase.

Does cortical clustering occur to increase efficiency of translocation to the anterior?

- We investigate whether larger clusters are more able to sense local cortical flows and whether this translates to more effective mobilisation to the anterior pole. Created by Rukshala Illukkumbura of the Goehring lab, we analyse microscopy images from dual-line (NMY-2::mcherry, PAR-3::GFP) embryos, allowing us to directly compare flows in the cortex and PAR-3 trajectories. We combine Particle Image Velocimetry (PIV) with single-particle tracking to quantify PAR-3 movement in response to cortical flows. On a local scale, we take inspiration from methodologies implemented by Dickinson et al. and investigate coupling between PAR-3 cluster and cortical flows. As a complement, we probe the relationship between cluster size and response to flows on a global scale, investigating the relationship between cluster size and efficiency of translocation to the anterior pole [78].

Is clustering instead a by-product of physical contraction within the cell?

- We look to address whether cluster size enhancement is a result of physical interaction of PAR-3 with the contracting acto-myosin cortex. To create a picture of contraction within the cortex we calculate the divergence – a measure of expansion and compression – of the cortical flow field using measurements obtaining from PIV. We look for correlation between cortical contractions and cluster size through-

out establishment phase, aiming to quantify the effect of physical forces on PAR-3 oligomerisation.

2.2 Image analysis of PAR-3 clusters *in-vivo*

2.2.1 PAR-3 cluster movement is closely associated to anteriorly directed myosin flows in the cortex

Long-range global flows towards the anterior pole have been identified as a key process for polarisation, working to rearrange membrane-bound polarity determinants. Able to respond to cortical flows, the scaffold protein PAR-3 has been identified as indispensable for polarity establishment. To quantify the nature of PAR-3 translocation along the anterior-posterior axis during establishment phase we moved to characterise the global flow of the membrane bound PAR-3 population, comparing features of the flow profile to the flow of cortical NMY-2. PAR-3 flow speeds have been previously measured directly from kymographs describing the spatio-temporal trajectories of membrane-bound clusters *in-vivo* [45]. Instead, we utilise the approach of Mayer et al. and implement Particle Image Velocimetry (PIV) on the microscopy images of dual-labelled (NMY-2, PAR-3) embryos using the methodology as described in section 2.4.3 [98]. As we are interested in the translocation of PAR-3 and NMY-2 to the anterior pole during establishment phase, we collapse the 2D flow field ascertained from PIV analysis into a 1D approximation along the anterior-posterior (A-P) axis. This enables us to distil a spatially averaged global flow profile, representing the global flow of components during establishment phase section 2.4.4.

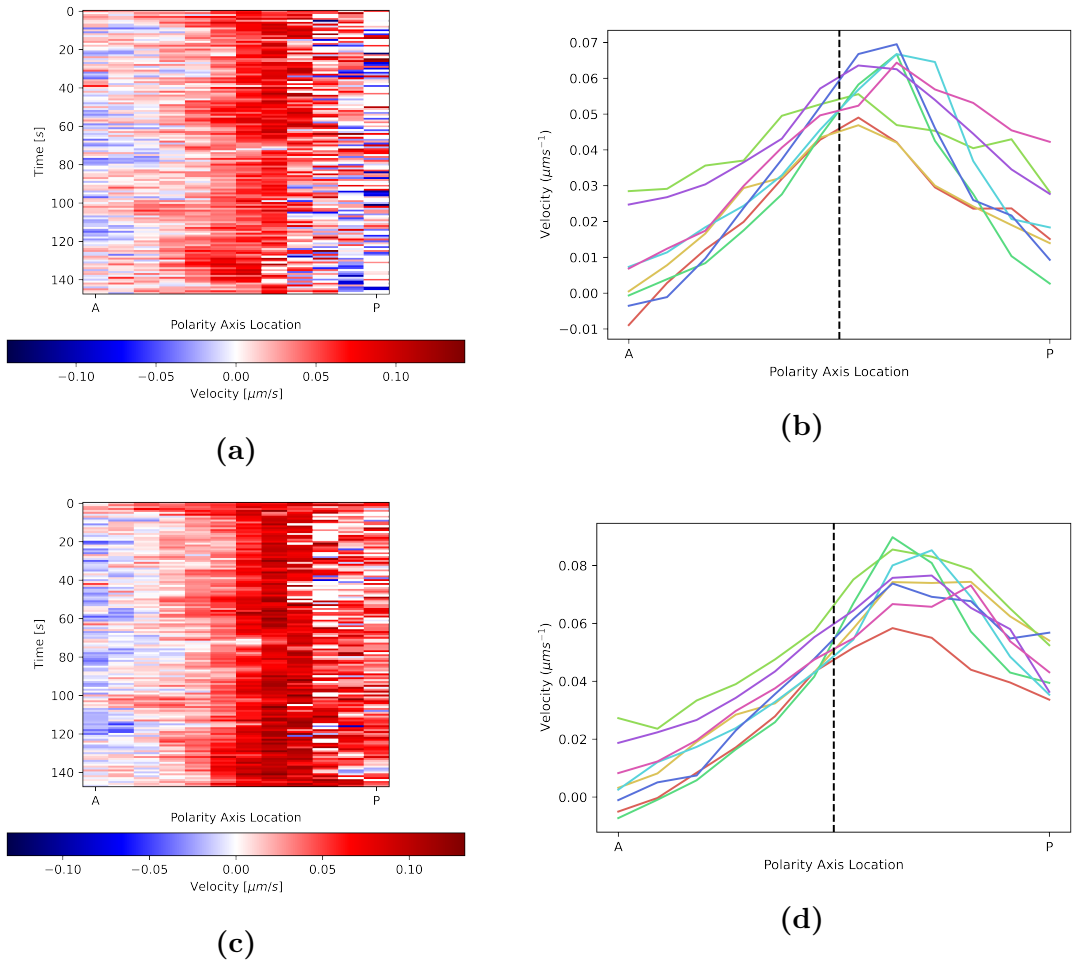


Figure 2.3: Global flow of PAR-3 closely matches that of cortical NMY-2. Kymographs of the global flow along the anterior-posterior axis reveal that **(a)** PAR-3 and **(c)** NMY-2 flows are closely coupled. Time averaged global flow profile of **(b)** PAR-3 and**(d)** NMY-2 flow illustrate a persistent peaked profile with an apex the posterior domain. Coloring indicates individual embryos ($n = 8$). Example kymographs shown for $n = 1$ embryos.

The kymographs representing the spatio-temporal evolution of this flow profile along the A-P axis over time for both PAR-3 and NMY-2 are shown in fig. 2.3a and fig. 2.3c respectively. Both kymographs indicate a strong anteriorly directed flow in the mid-posterior region for the duration of flow. Towards the anterior, flows diminish and at the extremal positions become retrograde. Notably, towards the anterior pole the strength of NMY-2 flows diminishes at a slower rate than that of the PAR-3 clusters, indicating that NMY-2 flows are the driver of PAR-3 translocation.

Figure 2.3b and fig. 2.3d represent the 10 s temporally averaged profiles for PAR-3 and NMY-2 respectively. The time averaged profiles show that through the imaged pe-

riod of 'peak' flow, the shape of the flow profile along the anterior-posterior axis remains consistent for both PAR-3 and NMY-2. The magnitude of flow speeds initially increases, reaching a peak before subsiding. Whilst this is in agreement with previous observations, the exact characterisation of this amplification is individual to the period of flow observed [70]. Notably, the width of the peak of the PAR-3 flow profiles becomes broader as flows subside. Differentially, NMY-2 flows remain under tight spatial control, with an average flow peak in the mid-posterior. The position of NMY-2 peak flows is located more posteriorly than our observed PAR-3 movement - a result expected in a model where a retracting acto-myosin cortex acts to advect membrane-bound protein. Having evidenced the close relationship between global cortical flows and the global flow of PAR-3, we next looked to probe the local dynamics of membrane-bound PAR-3 clusters. PAR-3 movement is composed of two types of motion, the bulk transport arising from interaction with cortical flows and lateral diffusion within the cortex. To quantify these individual contributions, we adopted the methodology of Dickinson et al. which enables the separation of advective and diffusive contributions to motion [60]. PAR-3 cluster tracks were mapped onto the flow-field of NMY-2, attributing each particle position an advective velocity due to flows in the membrane. This representative path through the advective flow field was used to calculate a theoretical trajectory of movement for the PAR-3 cluster. Should the PAR-3 cluster be perfectly coupled to flow within the cortex, this path represents the trajectory the cluster would have followed should its movement only be a result of cortical flow. Under this assumption and by comparison of our theoretical and measured trajectory, we can decompose PAR-3 motion and isolate the contributing dynamics - inherent diffusivity and advection as a result of cortical flows. Decomposition of total movement in this way enables reliable calculation of small diffusion constants. Independently, the small displacements resulting from such small diffusivities would be indistinguishable due to tracking becoming diffraction limited. By measuring flows on the cortex and utilising our knowledge that PAR-3 dynamics occur as a result of either advection by flow or diffusion. In this way, we use a non-contradiction principle to assign movement that is not a result of measured flow as being a result of diffusion, hence overcoming the barrier of

the diffusion limit. See section 2.4.5 for full methodological details.

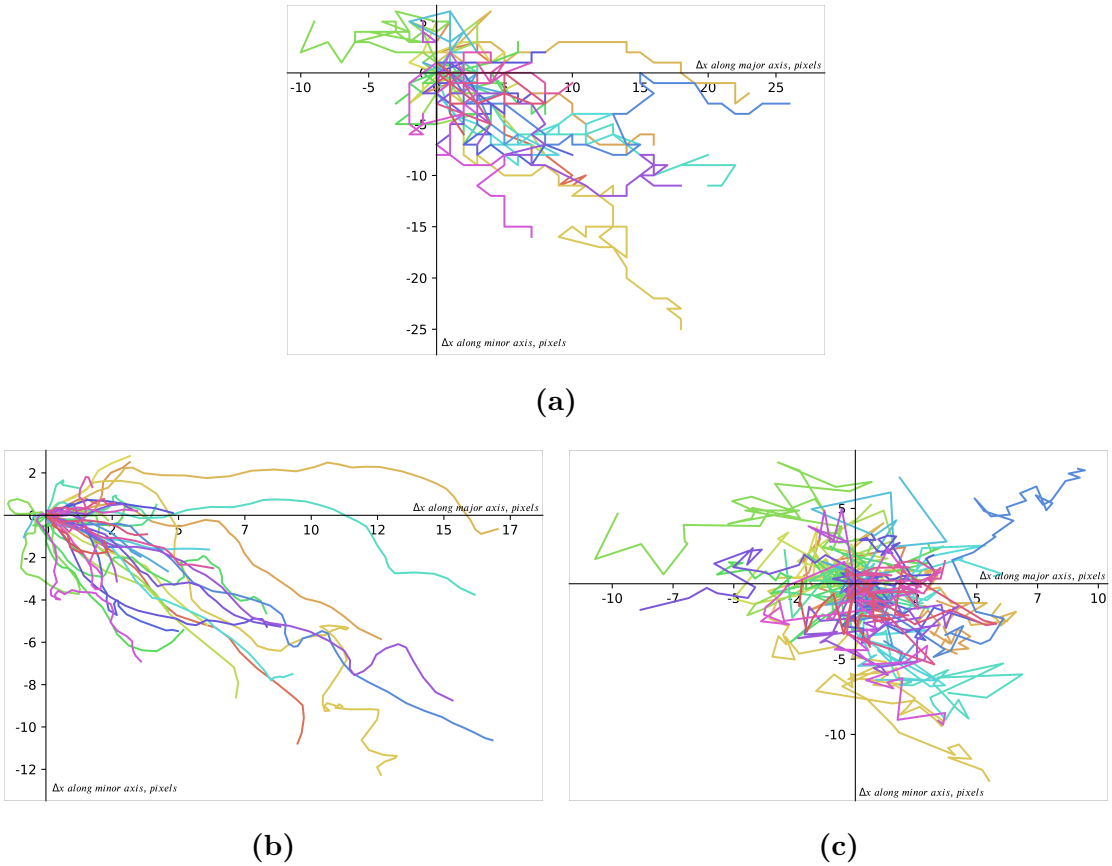


Figure 2.4: PAR-3 motion can be decomposed into constituent advective and diffusion components. (a) Trajectories of PAR-3 motion. **(b)** Advective contributions to PAR-3 motion. **(c)** Diffusive contributions to PAR-3 motion. Shown are n=45 of 228 tracks. Example shown for $n = 1$ embryos.

In fig. 2.4 we show the measured (fig. 2.4a) and calculated single-particle tracks that result from our initial separation of the dynamic contributions to PAR-3 cluster motion. The advective motion, fig. 2.4b, of PAR-3 is strong and directed with much of the total movement being accounted for by this bulk transport. As expected, the diffusive motion of individual PAR-3 clusters (fig. 2.4c) are characterised by tracks composed of randomly oriented movements in the membrane. As such, the ensemble of tracks spread outwards in all directions from the origin. If this motion was perfect diffusion, there would be no bias in directional preference of tracks [117]. However, fig. 2.4c shows a slight bias in the direction that bulk motion is oriented and this is more prevalent for longer tracks. This deviation from perfect diffusion can be attributed to two sources. Firstly, tracking of PAR-3 trajectories - and consequently analysis of flow - may become distorted close to

the embryo boundary and hence tracks originating from that region maybe give rise to random errors. Secondly, systematic errors manifesting as a directed population bias in (C) can be attributed to cumulative errors in the theoretically predicted track. The global flow profile in NMY-2 (see fig. 2.3) shows strong anteriorly directed flows in the posterior that become dampened as the proximity to the anterior pole reduces. If a high proportion of the cluster track is through a high-flow region, the accumulation of errors could lead to a reduced calculated bulk motion. With total motion comprising only of advective and diffusive flow, this underestimation manifests itself as an anteriorly-directed bias in the diffusive profile.

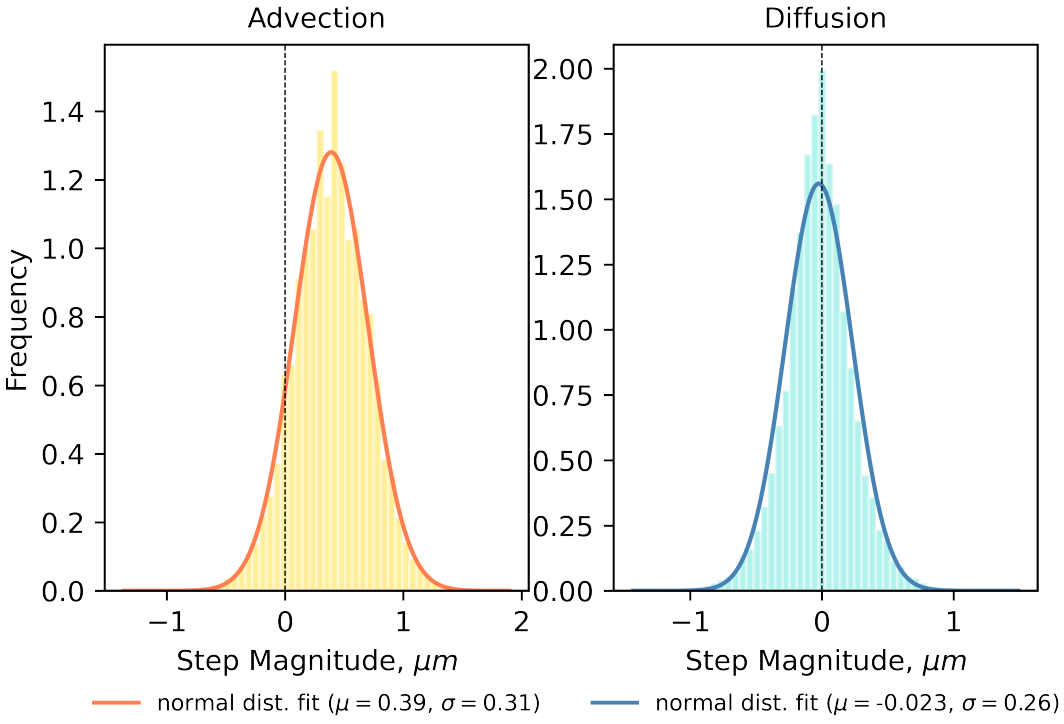


Figure 2.5: Advective and diffusive contributions to motion of the PAR-3 population. The contributions of diffusive and advective motion can be used to calculate their average flow-speed and diffusivity. This reveals that PAR-3 clusters are well coupled to local flows and diffuse slowly. $n = 8$ embryos.

With the dynamic components of PAR-3 motion segregated, we looked to quantify the advective and diffusive components of motion of membrane-bound PAR-3 at a population level. To this end, we use the representative diffusive and advective tracks of PAR-3 motion to calculate the distance travelled by each PAR-3 in a time-period, τ. In

order to minimise noise arising from short-lived particles, tracks of less than 10 consecutive frames were negated. All possible tracks representing a duration of $\tau = 10\,\mathrm{s}$, a time period selected to balance the need to minimise noise but maintain locality in the flow field, were utilised in analysis. The aggregated results in fig. 2.5 illustrates these parallel and perpendicular contributions to motion for $n = 6$ embryos. Advective motion is represented by a shifted Gaussian, representing directed motion. The mean, μ of the this Gaussian represents the average distance a PAR-3 cluster has advected in the time frame. Using the conversion , $\bar{v} = \frac{\mu}{\tau}$, it is found that on average PAR-3 clusters advect with speed $\bar{v} = 0.04\,\mu\mathrm{ms}^{-1}$. This average flow speed is comparable to the flow speeds measured in the cortex in fig. 4.4, evidencing that the PAR-3 clusters are coupled closely to local flow in the cortex. As expected, at a population level, the diffusive motion can be represented with a Gaussian centered around zero. An average diffusion coefficient can be calculated using the standard deviation σ of this centered distribution, using $\bar{D} = \frac{\sigma^2}{2\tau}$. Diffusion of PAR-3 is characterised by a coefficient of $\bar{D} = 0.003\,\mu\mathrm{m}^2\mathrm{s}^{-1}$. This reveals that PAR-3 clusters diffuse more slowly than their anterior partner (PAR-6, $\bar{D} = 0.28\,\mu\mathrm{m}^2\mathrm{s}^{-1}$) likely due to their increased size [118].

2.2.2 PAR-3 cluster size does not affect its efficiency of translocation towards the anterior

With the knowledge that PAR-3 clusters remain closely coupled to local flows, we next moved to address the hypothesis that larger clusters are better able to 'sense' flow and are translocated more efficiently to the anterior pole. Tracks representing PAR-3 cluster motion on the cortex for a time period $\tau = 10\,\mathrm{s}$ were therefore grouped into those belonging to the smallest and largest 10% cluster sizes, based on their average cluster size. Figure 2.6 shows the relationship between speed of translocation of PAR-3 clusters to the anterior and their cluster size. Notably, the transport velocities for both the largest and smallest cluster sizes are similarly distributed. Using the mean and standard deviation from a fitted Gaussian, a student's t-test was carried out to distinguish the mean velocity of the largest and smallest clusters. With $t = 0.489766$ and $p = 0.625372$, we can reject the null hypothesis that there is a difference between the average velocities of the larger and

smaller clusters and conclude that all clusters are equally coupled to flows within the cortex and therefore cluster size is a dispensable for flow 'sensing'.

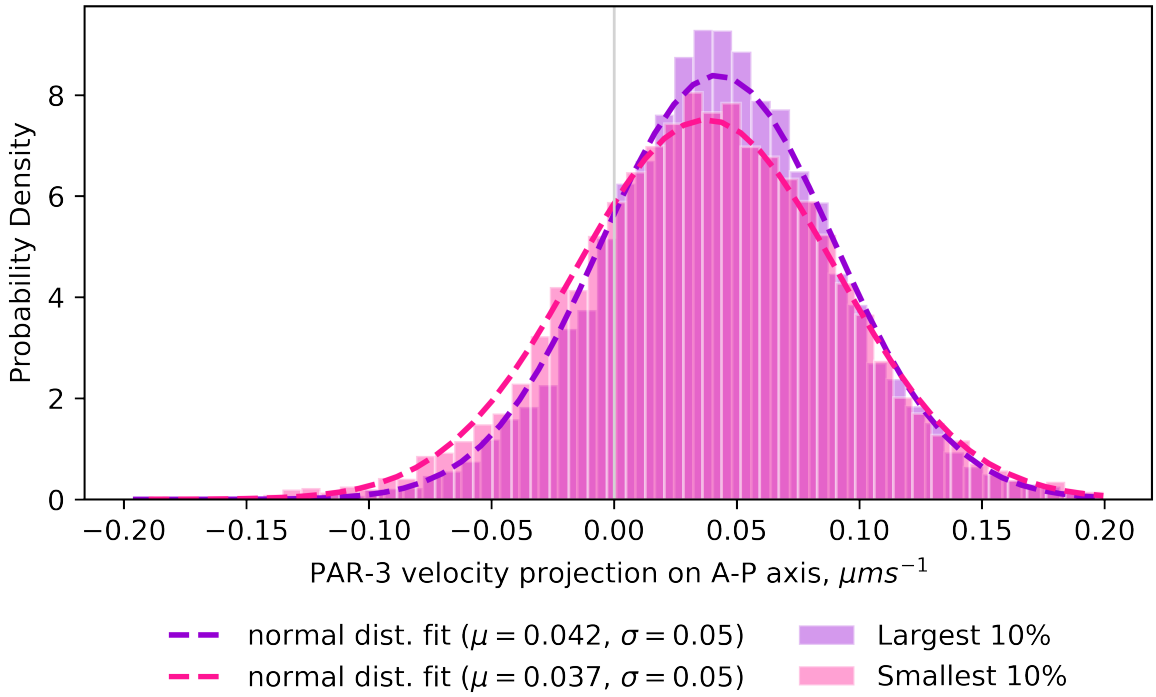


Figure 2.6: Larger PAR-3 clusters do not translocate to the anterior with greater efficiency. Shown is the average velocity of PAR-3 motion in direction of the anterior pole for the largest and smallest 10% of clusters. Cluster sizes are calculated based on the average cluster size for the duration of the particle track. All possible tracks of length 10 s were considered. $n = 8$ embryos.

2.2.3 PAR-3 clusters are not enlarged as a direct by-product of cortical contractions

The cortex is a highly-dynamic contractile framework that reorganises in response to internal and external mechanical stresses. An increase in indirect cortical tension has been shown to rescue PAR-3 clustering, highlighting the action of mechano-chemical feedback in the cortex [72]. Microscopy observations of single-cells during establishment phase have widely documented visible 'ruffling' in the cell surface as a result of cortical flows. These surface invaginations represent deformations in the cortex, contractions within which would bring membrane-bound components into closer physical proximity. Together, these observations lead us to consider whether cluster size could be directly

affected by cortical contraction. We considered whether regions of the cortex undergoing contraction gave rise to larger PAR-3 clusters. The divergence of the global flow field was calculated; negative divergence indicated convergent flows and were considered to therefore indicate contractile regions of the cortex. We considered the largest and smallest 25% of cluster sizes at any instance. Shown in fig. 2.7 is the distribution of the PAR-3 cluster sizes and the instantaneous divergence of the global flow field at the location of the cluster. There is an overall bias towards negative divergence, indicative of a contractile cortex, but there is no discernible bias towards larger clusters being more frequently found in areas of negative divergence.

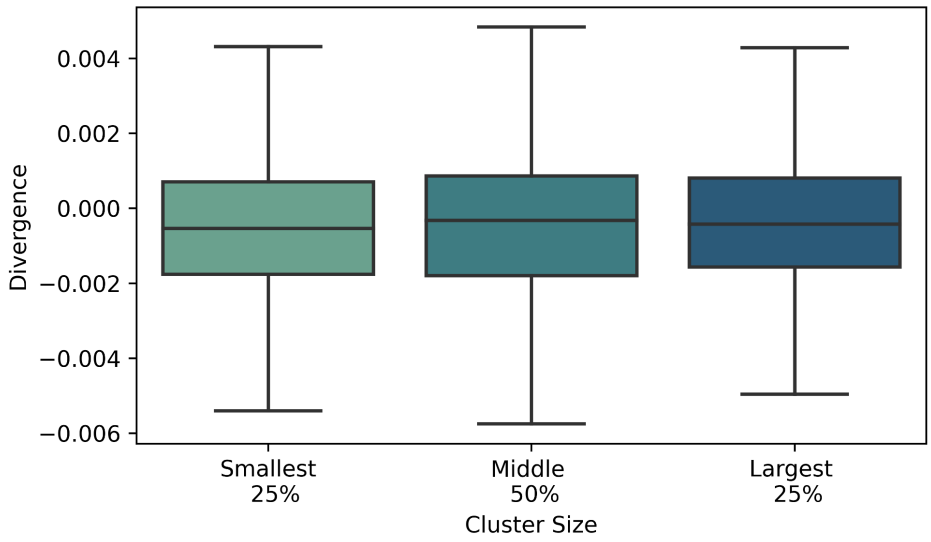


Figure 2.7: Larger PAR-3 clusters are not localised preferentially in areas of local contraction. $n = 2538$ clusters.

We next investigated whether PAR-3 clusters underwent a period of growth whilst residing in a contractile region. fig. 2.8 shows the change in total integrated brightness for PAR-3 clusters emerging from a region of positive (extensile) or negative (contractile) divergence. Clusters both increased and decreased in size after emergence from either region, with no favourable behaviour for cluster growth after residence in a contractile region. Therefore, we cannot conclude that PAR-3 cluster sizes are enhanced as a direct by-product of cortical contraction and physical rearrangement of the cortex.

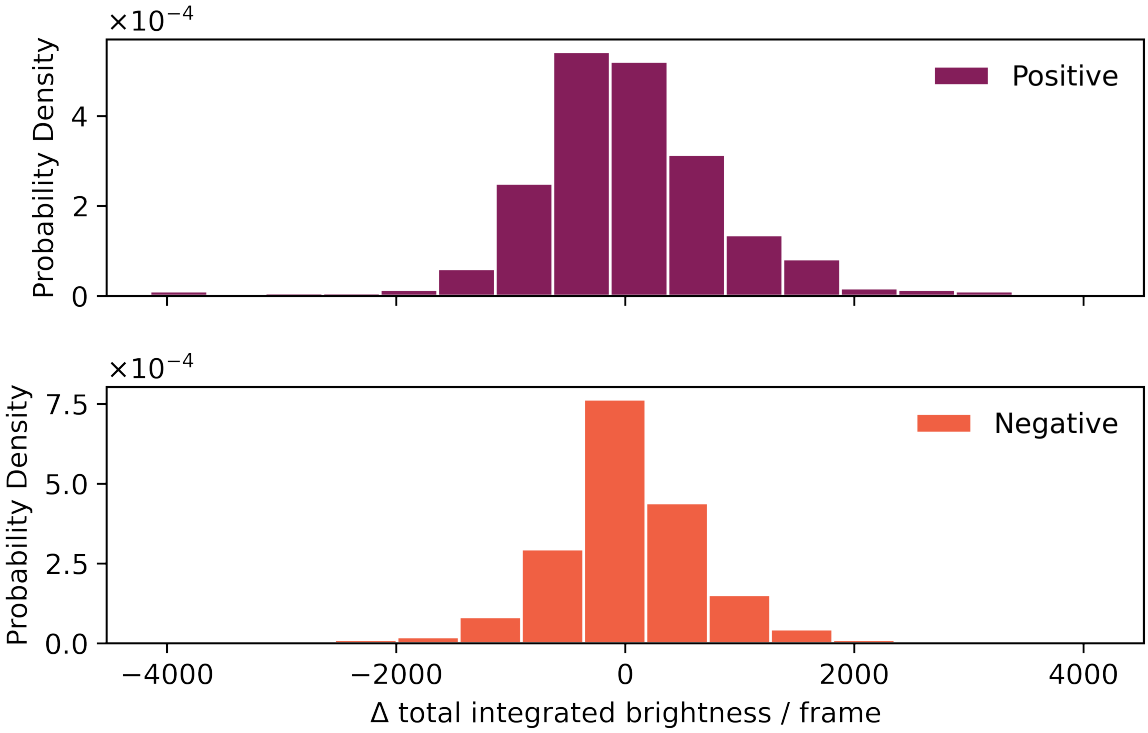


Figure 2.8: PAR-3 clusters do not undergo preferential size enhancement after localisation in a region of contraction. PAR-3 clusters were preferentially located in regions of contraction ($n = 2386$) as opposed to expansion ($n = 557$ tracks). $n = 8$ embryos. However clusters appeared to show no favourability of size enhancement after localisation in a region of contraction.

2.3 Discussion

Motivated by the recent experimental observations of PAR-3 clusters, we sought to investigate recent hypothesis to functionally explain the increase in both number and intensity of PAR-3 clusters during establishment phase. There is a wealth of evidence readily available that links PAR-3 transport to cortical flows (see section 2.1.4 for exploration of this topic). However, open questions remained as to whether PAR-3 clusters form to increase sensitivity to such cortical flows or whether they are a simple by-product of direct interaction with the contractile cortex.

Initially, we applied single particle tracking and Particle Image Velocimetry to microscopy images of dual-labelled (PAR-3:GFP x NMY-2:mKate) embryos, allowing us to track motion of the cortex and PAR-3 clusters in tandem. Qualitatively consistent flow profiles through establishment phase demonstrated the global coupling of PAR-3 and the

cortex, in agreement with the previous experimental observations of Munro et al. and Wang et al. [45][72]. We employed similar methodology to Dickinson et al., segregating advective and diffusive components of PAR-3 movement to probe local coupling of PAR-3 to cortex. Results demonstrated that on average, PAR-3 flowed at a speed $0.04\,\mu\mathrm{ms}^{-1}$, with a diffusion coefficient of approximately $0.003\,\mu\mathrm{m}^2\mathrm{s}^{-1}$. This average flow speed is less than the maximum flow speed of NMY-2 found in both this work (fig. 2.3c) and the previously measured values of Mayer et al. [98]. However, this is expected as cortical flows attenuate towards the anterior pole and as a result, once PAR-3 cluster translocate to this domain their movements will be significantly reduced. Additionally, our observations of the global flow field in the cortex indicate that the position of peak flow in the cortex remains spatially localised throughout establishment phase. Therefore, it is unsurprising that as PAR-3 clusters move through this location and become anteriorly bound, we obtain an average flow speed that is below the maximum flow speed of the cortex.

A key question raised in the experimental work of Rodriguez et al. is whether larger clusters are better able to 'sense' flows and therefore undergo more efficient translocation to the anterior pole. To investigate this hypothesis, we categorised cluster tracks by their average intensity and compared the movement of the largest and smallest clusters in the direction of the polarity axis. Through this comparison, we found no correlation between cluster size and ability to flow to the anterior and so conclude that the functional role of larger clusters is not to promote more efficient polarisation through sensitivity to flows. As a caveat to this conclusion, Dickinson et al. reported the finding that PAR-3 clusters had a larger Peclet number and were thus more efficiently moved by advective transport. An appropriate hypothesis that would satisfy both these conclusions is that larger PAR-3 clusters must instead diffuse more slowly. This investigation is outside the scope of this thesis. Additionally, Dickinson et al. found that larger clusters had an increased membrane lifetime which could contribute to efficient anterior translocation simply by an increased duration of advection by flow. Therefore, whilst larger clusters are not more sensitive to flows, their increased size and thus membrane lifetime may work to aid

polarisation through increased exposure to cortical flows. Additionally, larger clusters have been observed to undergo slowed diffusion which could favour advective motion and hence provide increased efficiency of translocation to the anterior [118].

The enhancement of PAR-3 clusters through establishment phase could occur as a by-product of physical contraction of the cortex. Wang et al. reported that PAR-3 clustering in non-contractile embryos could be rescued through artificially increasing tension in the cortex – here through application of hypotonic buffer treatment. To further investigate the hypothesis that cortical forces directly induce PAR-3 clustering, we investigated the relationship between both cluster size and the contractile motion of the cortex. Taking the divergence of the NMY-2 flow field as an indicator of compressive or extensile motion, we found no relationship between enhanced PAR-3 cluster size and location in a contractile region of the cortex. Assuming de novo clustering, we probed whether cluster size was preferentially enhanced after dwelling in a contractile region - again, we found no preference for cluster size enhancement. As a caveat to this conclusion, it is likely that our analysis would not observe cluster merging events due to contraction. Additionally, acto-myosin foci undergo pulsatile dynamics with a periodicity on the order of $\sim 10s$ and therefore our instantaneous analysis of NMY-2 and PAR-3 may not fully capture the interaction between clusters and cortical contraction [119]. Recently published work from Chang and Dickinson provides evidence that PAR-3 clusters are not directly embedded in the cortex and instead larger clusters are transported through viscous friction [118]. Our analysis of PAR-3 clustering as a direct response to local contraction in the cortex assumes tPAR-3 clusters are directly embedded in the cortex. This new work therefore supports our findings that contraction of the cortex did not directly enhance cluster size as it reveals that our assumption of binding does not hold. Additionally, this reinforces the validity of the modelling choice – PAR-3 translocation by passive advective transport – that underlies investigations of the subsequent chapter in this thesis.

2.4 Methods

2.4.1 Experimental Imaging

Imaging of *C. elegans* zygotes was carried out by R. Illukkumbura of the Goehring polarity laboratory of the Francis Crick Institute. Dual lines, PAR-3:GFP (green) x NMY-2:mKate (red) were created using the NWG150 worm line. Green, red and dic images were acquired sequentially. Images were acquired at 10% laser power, with an exposure time of $80\,\mu$s and $100\,\mu$s for the green and red channel respectively. The time interval between frames was 1 s. The embryo was imaged for the duration of establishment phase, where cortical flows were at their peak.

2.4.2 Single particle Tracking

Single particles tracking was carried out by R. Illukkumbura of the Goehring polarity laboratory of the Francis Crick Institute using TrackPy software.

2.4.3 Particle Image Velocimetry

Particle Image Velocimetry (PIV) is a widely used technique implemented to quantify fluid flow within a material, from which a visualisation of the global flow field can be constructed [120]. The technique was initially implemented within the field of engineering, with 'tracer' particles illuminated within a fluid and recorded over a time period. Individual frames would then be split into spatial 'interrogation windows'. Correlation functions are then computed between sequential frames for each interrogation window. The correlation function is used to find the location of the displacement peak, from which a velocity vector is calculated that represents the average linear motion for the region of space the interrogation window represents. When viewed in series, the global picture of these linear velocities in space represents the fluid motion within the material.

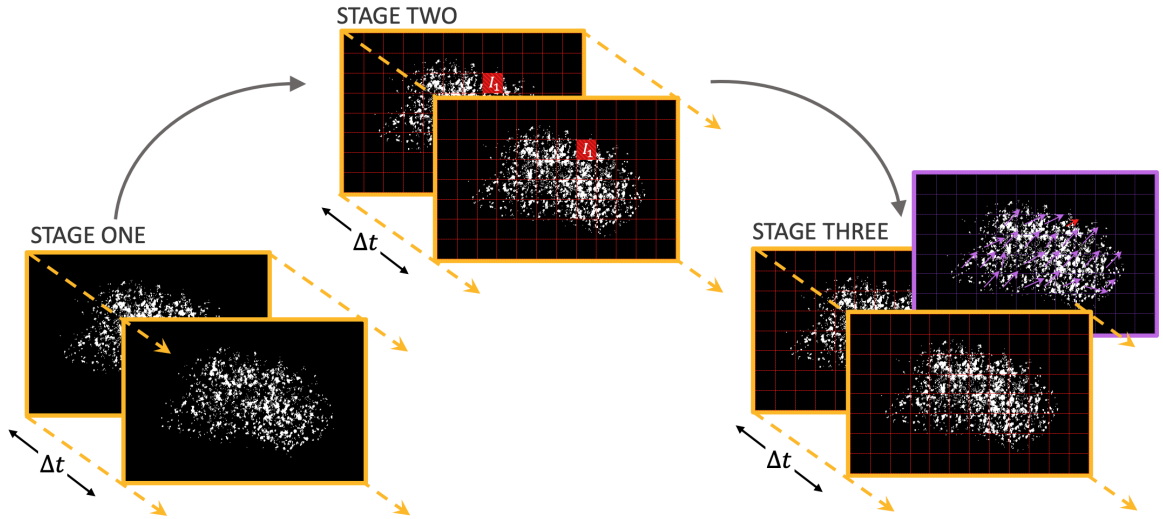


Figure 2.9: A schematic representing the PIV process. Tracer particles are observed in the fluid of interest in 'Stage One'. Each image is split grid-wise into interrogation windows in 'Stage Two'. Correlation functions between $I_{1,t}$ and $I_{1,t+1}$ are calculated. In 'Stage Three', the displacement peak of the correlation function is calculated and a velocity vector attributed to the space the interrogation window represents (purple). A global picture of the spatio-temporal fluid flow is built through the combination of these local linear velocity approximations.

Assumptions of PIV are; that fluid motion is linear within an interrogation window, that tracer particles are homogeneously distributed and that tracer particles within an interrogation window follow the flow exactly. These assumptions place limitations on method implementation. A higher particle number within an interrogation window reduces the signal-to-noise ratio and the associated error in locating the peak displacement from the correlation function [121]. This limits the granularity of the overall flow-field, as a window size can be minimised only until a threshold particle density is reached, below which a high valid detection probability can no longer be achieved. Further, it is recommended to limit the interrogation window size to ensure that particle motion between frames remains within the search window, again ensuring a high valid detection probability [122]. This leads to the below recommended constraints for the particle number per window, N and the interrogation window size D_I;

1. $N \sim 6$

2. $D_I > 4|\Delta x|$

where Δx is the expected in-plane motion of a tracer particle.

PIV analysis was carried out on both tagged NMY-2 and PAR-3 particles, using images from the single particle tracking microscopy experiments of R. Illukkumbura of the Goehring Laboratory. These dual-tagged lines enabled us to probe both the flows of the cortex and the motion of the membrane-bound PAR protein respectively. PIV was carried out using the MATLAB package, PIVlab [123]. The images were initially sharpened using a high-pass filter with 100 pixel kernel size. PIV was carried out using a multi-pass FFT window deformation algorithm within PIVlab. ImageJ was used to create binary masks of the zygotes, which were in turn used to eliminate spurious PIV data that did not pertain to the tagged particles. To create the mask, the embryo edge was hand drawn and an ellipse fitted to the selection and binarised. The masked vector field then underwent vector validation to further remove erroneous vectors; any vector with a magnitude larger than $0.15\,\mu\mathrm{ms}^{-1}$ was discarded [98]. Due to the interrogation window size, resultant PIV vectors are separated by 8 pixels. To obtain a full picture of the flow field, the 'between' pixels were populated through bi-cubic interpolation.

2.4.4 Global flow along the anterior-posterior axis

Individual embryos were approximated as an ellipse using the ellipse fit tool in ImageJ. The extremal points of major axis of the fit were used to denote the anterior and posterior poles, and the major axis the polarity axis. This axis was then divided into 13 orthogonal sections. The processed velocity vectors from Particle Image Velocimetry (see fig. 2.9) were then assigned to corresponding bins and an average vector calculated. Bins with less than three vectors were disregarded. This affected polar regions due to the reduced area as a result of the elliptical boundary. This projection of this average velocity vector was then used to calculate a representative global flow in the direction of the anterior pole for the axis section. This methodology is similar to that used in the work of Mayer et al. [98]. The projection of the vector can be calculated using:

$$proj_u v = \left(\frac{v \cdot u}{|u|} \right) \tag{2.1}$$

where u is the vector in the direction along the polarity axis and v is the velocity vector.

2.4.5 Local flows of PAR-3 clusters on the membrane

PAR-3 clusters were imaged and tracked as described in section 2.4.1 and section 2.4.2. PAR-3 tracks of less than 10 continuous frames in length were discarded and the remaining tracks were split into 10 frame sections on a rolling basis. Each position along the track was then matched with the corresponding velocity vector from the interpolated NMY-2 global velocity field calculated using PIV (see section 2.4.3). A theoretical track, denoting the path travelled had the cluster's motion only been a result of cortical flows, was calculated from the matched velocity vectors. Positional vectors were calculated from the origin to the final position of both the observed and theoretical tracks. These resultant vectors were then compared to calculate the advective and diffusive components of PAR-3 movements, as in fig. 2.10. The projection of the observed vector onto the theoretical vector gives rise to the movement of PAR-3 due to advection by cellular flows. Correspondingly, the rejection of the observed vector to the theoretical vector denotes the diffusive component on movement.

$$s_{advection} = \left(\frac{s_{observed} \cdot s_{theoretical}}{|s_{theoretical}|} \right) \tag{2.2}$$

$$s_{diffusion} = \left(\frac{s_{observed} \cdot s^{\top}_{theoretical}}{|s_{theoretical}|} \right) \tag{2.3}$$

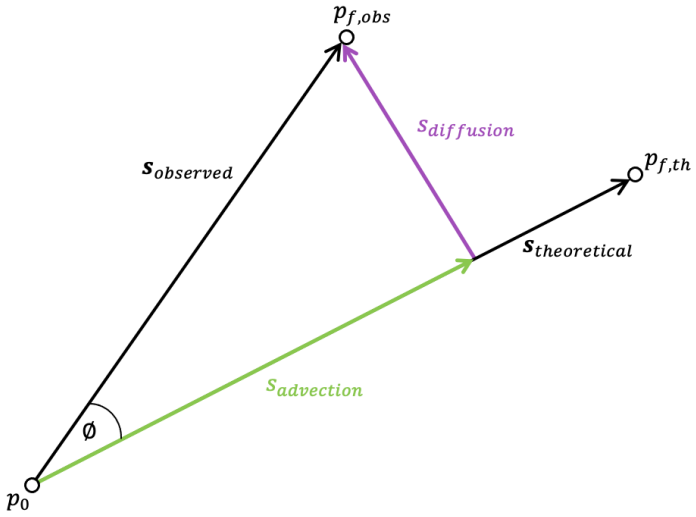


Figure 2.10: Decomposition of a vector of motion into contributions of advective and diffusive motion. Assuming perfect coupling, we can compare local motion of PAR-3 directly to NMY-2 flows in the cortex to reveal diffusive and advective contributions to motion. The projection of the displacement vector representing observed motion ($s_{observed}$) and the displacement vector representing theoretical motion ($s_{theoretical}$) if perfectly coupled to NMY-2 flows reveals the PAR-3 motion as a result of flows ($s_{advection}$). The rejection of these two vectors represents PAR-3 motion as a result of diffusion ($s_{diffusion}$).

Using the Gaussian fit of the distribution composed from the diffusive contributions to motion, the PAR-3 diffusion coefficient D_{A3} can be calculated using:

$$D_{A3} = \frac{\sigma^2}{2\tau} \tag{2.4}$$

where σ is the standard deviation of the normal distribution of diffusive vector lengths and τ is the elapsed time. Similarly, a value for the expected velocity for a PAR-3 cluster can be calculated using the mean of the Gaussian fit to the distribution of advective vector lengths:

$$v_{A3} = \frac{\mu}{\tau} \tag{2.5}$$

where μ is the mean of the normal distribution.

2.4.6 Divergence of the cortex at the position of a PAR-3 cluster

The divergence of the cortical flow field was calculated using the interpolated PIV profile, V, of the embryo:

$$\nabla \cdot V = \frac{\partial V_x}{\partial x} + \frac{\partial V_y}{\partial y} \tag{2.6}$$

Using the interpolated flow field allowed for each pixel image to be allocated a divergence value. Areas of negative divergence indicate regions of compression, positive divergence that of expansion and zero divergence indicates parallel flow through an area (see Figure 2.11). PAR-3 image positions were matched with their corresponding position in the divergence field, allowing each PAR-3 cluster over time to be mapped with the corresponding divergence in the NMY-2 cortex. Some PIV vectors are erroneous and discarded from analysis, see section 2.4.3. To ensure continuity in analysis, a binary mask indicating the position of erroneous vectors was produced for each image in the NMY-2 movies. PAR-3 cluster positions that matched with 'missing' NMY-2 flow data were correspondingly discarded from analysis. In some cases, this leads to shortening of analysed track lengths as these will be ''cut' as a result of this process.

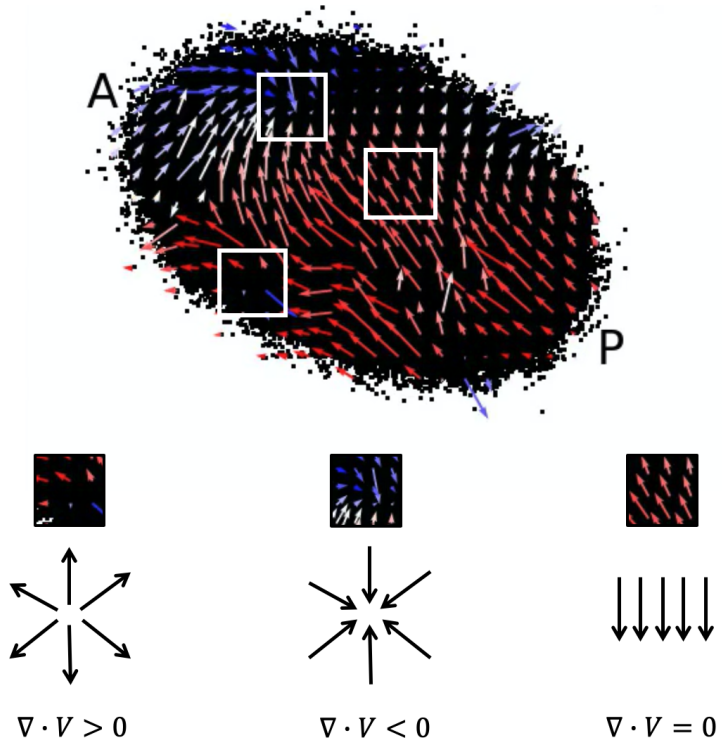


Figure 2.11: Divergence in the global flow field of NMY-2 The global flow field resulting from our PIV analysis reveals areas of positive, negative and near zero divergence. Negative divergence relates to flow compression and positive divergence flow expansion. Zero divergence indicates correlated, directed flow through a region.

Chapter 3

Tables (Image Analysis)

Supporting data for image analysis procedure on the NWG-180 set.

Embryo (n)	Frames (n)	Perimeter (μm)	Major Axis (μm)	Minor Axis (μm)
1	151	116.45	44.48	28.79
2	177	120.84	47.18	28.58
3	138	110.27	40.14	29.64
4	148	127.43	49.01	31.09
5	137	126.83	48.26	31.58
6	49	114.64	44.11	27.96
7	195	121.46	46.77	29.56
8	238	119.85	45.18	30.37

Table 3.1: Dimensions of embryos used in analysis, produced using the Ellipse Fit function within ImageJ.

Embryo (n)	Minimum Velocity A-P Projection ($\mu m s^{-1}$)	Maximum Velocity A-P Projection ($\mu m s^{-1}$)	PIV vectors (n)	PIV vectors accepted (%)
1	-0.1221	0.1315	42431	48.67
2	-0.1311	0.1315	47259	49.44
3	-0.0752	0.1265	36156	62.74
4	-0.1296	0.1431	54464	50.75
5	-0.1440	0.1415	52471	55.51
6	-0.0926	0.1344	13328	55.11
7	-0.1182	0.1315	67080	50.02
8	-0.1438	0.1468	84490	48.99

Table 3.2: Vector results of Particle Image Velocimetry analysis of PAR-3 clusters. Produced using the PIVlab package in Matlab.

Embryo (n)	Minimum Velocity A-P Projection (μms^{-1})	Maximum Velocity A-P Projection (μms^{-1})	PIV vectors (n)	PIV vectors accepted (%)
1	-0.0831	0.1301	42431	60.73
2	-0.0899	0.1407	47259	57.15
3	-0.0490	0.1417	36156	65.20
4	-0.0857	0.1322	54464	57.37
5	-0.1040	0.1304	52471	62.94
6	-0.0724	0.1323	13328	59.28
7	-0.0822	0.1302	67080	58.60
8	-0.0733	0.1323	84490	57.94

Table 3.3: Vector results of Particle Image Velocimetry analysis of cortical NMY-2. Produced using the PIVlab package in Matlab.

Embryo (n)	PAR-3 Tracks (n)	Tracks accepted (%)
1	1209	97.85
2	1600	95.88
3	916	97.82
4	1904	93.64
5	2581	98.06
6	764	96.73
7	2546	95.60
8	2889	94.36

Table 3.4: PAR-3 single particle tracks used in local flow analysis.

Chapter 4

Reaction-diffusion modelling to uncover the design principles of polarity development in the *C. elegans* zygote

4.1 Reaction-diffusion models describing of the PAR proteins and cellular cortex

Reaction-diffusion modelling has long been implemented to gain mechanistic understanding of polarity development and pattern formation. Ranging from simple single-species models to more complex network structures, mathematical models of this kind have contributed significantly to understanding underlying design principles. In this section, we review some of the key works that contribute to our toolkit of design components, enriching our fundamental understanding of polarisation in the *C. elegans* zygote.

Tostevin and Howard first modelled polarity establishment in *C. elegans* using a reaction-diffusion system to address complex, co-dependent and sometimes redundant biochemical polarity pathways in vivo. It was known that through dynamic remodelling, the acto-myosin architecture was able to influence its own mechanical properties. As a result of such cortical contraction, acto-myosin flows occurred which were linked to polar-

ity establishment [45]. However, questions remained as to the exact relationship between cortical flows, the acto-myosin cortex and the PAR proteins. Addressing this question, the model introduced by Tostevin and Howard sought to decipher whether a reaction-diffusion model coupled directly with a model of acto-myosin contractility could establish polarity. Taking a physical perspective of acto-myosin dynamics, the cortex is modelled as a simple elastic spring which interacts mechano-chemically with the PAR proteins. Integrating the exclusionary dynamics observed by Cuenca et al., the PAR proteins were modelled as two antagonistic groups which bind to the membrane, diffuse, and eventually unbind to re-join the cytoplasmic pool. Further experimental work by Goehring et al. has since affirmed this mutually antagonistic behaviour, with FRAP experiments revealing spatial regulation of protein binding affinities within domains [115]. An increase in the density of the acto-myosin cortex, which initially broke symmetry through down-regulation at the posterior, resulted in upregulated anterior membrane binding. In turn, the elastic properties of the acto-myosin cortex are modulated by the anterior protein, reflecting the experimental observation that anterior PAR upregulates its own translocation by cortical flows. The model recapitulated polarity establishment, able to replicate both cortical flow speeds and final cortical distributions of PAR protein. Importantly, through alteration of the anterior binding rates, the model could successfully reproduce experimentally observed mutant phenotypes. PAR-3 mutant behaviour was recapitulated through prevention of cytoplasmic anterior protein binding to the membrane: the acto-myosin cortex did not retract completely and the final membrane state was uniformly posterior. However, reproduction of some local mechanical aspects of the contractile cortex, such as anisotropies in contraction and observed cortical ruffling were sacrificed in place of modelling simplicity.

This first model of polarisation illustrated that acto-myosin asymmetry was sufficient to trigger polarisation within the *C. elegans* zygote. However, simplifications in the model implementation – such as that of a communal anterior pool through which mutant phenotypes can be replicated by alteration of the binding rates – limit the model applicability. In this sense, an up-regulation of PAR-3 association through establishment phase

would limit the availability of cortical PAR-6 and attenuate its association, an effect not observed *in-vivo*. Further, a model of this kind could not explain some observations in vivo – such as the different localisation profiles of PAR-3 and PAR-6 or cytoplasmic gradients present during polarisation. Crucially, in the absence of acto-myosin dynamics the model presented by Tostevin and Howard was unable to establish polarity through only the PAR interaction dynamics. This is a key limitation to the general applicability of the model as further experimental work indicated that in the absence of cortical flows the PAR network could instead polarise through a secondary, redundant pathway that was independent of the ECT-2 dependent flows. This secondary pathway instead initialises polarisation through localised recruitment of PAR-2 which subsequently excludes the anterior scaffold protein PAR-3. Through this pathway stabilisation, the time to stabilisation of the domain boundary exceeds that of primary polarisation, approximately 40 min in simulations [70]. A negative feedback loop ensues as a lack of cortical PAR-3 down-regulates myosin recruitment which in turn produces cortical flows which act to translocate PAR-3 further from the posterior [124].

Dawes and Munro utilised reaction-diffusion modelling to show that mutually antagonistic dynamics were sufficient to maintain polarised domains if the interactions included a non-linear feedback. Interruption of the acto-myosin cortex *in-vivo* had revealed that whilst the initial perturbation of cortical flows was necessary to establish polarity, the cell could maintain polarity when decoupled from the acto-myosin dynamics [70]. Reflecting this, the model of Dawes and Munro simplified the approach of Tostevin and Howard, by instead requiring that only an initial perturbation was necessary for polarity establishment and that this perturbation could be acto-myosin independent. Congruent to the finding of Tostevin and Howard, when linear mutual antagonism was included in the model only a single homogeneous steady state existed and hence polarisation was unstable. However, stable polarisation could be recovered by the inclusion of dimerisation in the anterior protein. Here, this represented the suspected oligomerisation of the scaffold protein PAR-3 which through biochemical investigation had been revealed to contain the conserved CR1 domain, responsible for self-association [112]. With dimerisation, this

actin-independent model of polarisation instead yielded a bi-stable character and domains were maintained. This work predicted a threshold relationship between the level of anterior PAR on the membrane and successful polarisation, which was subsequently observed in experiment. Interestingly, this loss of polarisation was not predicted when the levels of anterior and posterior protein were reduced synchronously. In experiment, this behaviour is observed when dual run-down of opposing PAR species, for instance PAR-2 and PAR-6, leads to recovery of polarity [125]. The model of polarity presented by Dawes and Munro successfully recapitulated maintenance of polarisation on a biological time-scale. However, the authors note that in the long-term the presence of diffusion results in drifting of the domain boundary. It is noted that whilst this is not an issue on the time-scale of the embryo, there is likely a buffering mechanism that works to stabilise the boundary and increase the robustness of polarisation. One such mechanism that could work to achieve this is the wave-pinning mechanism, first introduced by Mori et al. in a model describing polarisation in motile eukaryotic cells. The study detailed the behaviour of a single Rho protein, cycling between an active, membrane-bound and inactive, cytosolic state. In response to a transient stimulus, the system locally amplified the concentration of membrane-bound protein. Spatial amplification led to a propagating wave across the cell that, differentially to the simulations of Dawes and Munro, eventually stalled or 'pinned' and was indefinitely maintained at this position. To achieve wave-pinning Mori et al. illustrated three necessary qualitative conditions on the model equations describing a patterning system: spatial uniformity in the inactive form - usually achieved through super-fast diffusion in the cytosol, bi-stability in the reaction terms and mass-conservation across the system [126]. This final element, mass-conservation, is ubiquitous among the models discussed in this chapter. This feature of the models invokes a 'limiting pool' whereby progression of a domain front is slowed through reduction in the available cytosolic material available for recruitment to the membrane. Interestingly, recent work by Hubatsch et al. has implicated a critical cell size below which polarisation through a wave-pinning mechanism can no longer be upheld and the cell fails to divide asymmetrically. Coupling reaction-diffusion simulation with experimental observation, it was

found that this critical system size corresponded to the size of the P_3 cell - the first P cell which no longer polarises and divides asymmetrically. Extrusion of material to produce artificially small P_0 cells which then failed to polarise asymmetrically provided further evidence of the dependence on cell size for asymmetric cell division. The breakdown of asymmetric division is intrinsically linked to the diffusivity of the active components and reaction rates, which in turn define size of the domain interface. Below a critical size and with biologically relevant polarisations, Hubatsch et al. illustrated that the cell can no longer support a boundary interface and polarity is lost [127].

The model of polarisation introduced by Goehring et al. implemented a wave-pinning mechanism of the sort introduced by Mori et al. to explain how polarisation could occur through coupling of a reaction-diffusion system to an advective trigger - cortical flows. Through a combination of modelling and experiment, advective triggering was shown to be a sufficient transient stimulus to initialise a polarisation that characteristically represented that observed in the cell. Mutual antagonism with non-linear stoichiometry endows the system with bi-stability and enables a polarised state to be maintained. Stabilisation of the pattern was achieved through a limiting cytoplasmic pool which, as described above, worked to stall domain front propagation. Alike the work of Tostevin and Howard, this model represented the anterior and posterior PARs as two opposing groups. A simplification of this kind enabled the group to focus on the role of cortical flows in establishment phase and demonstrate that passive advective transport, rather than direct interaction with the acto-myosin cortex was sufficient to explain polarisation. As a result, the simplification of the PAR proteins into two opposing groups overlooks the sub-population interactions and the consequences these could have on the robustness of polarisation, particularly if proteins were to be characterised by different dynamic behaviours. As such this work cannot explain the varying degrees of co-localisation between PAR-6/PAR-3 observed *in-vivo* [60].

4.1.1 Modelling the anterior PAR proteins

A clear extension to the model present by Goehring et al. would be one in which the reactions between the dynamically opposed anterior proteins are investigated in finer de-

tail. The model presented by Goehring et al. clearly recapitulated the PAR-6 profile observed *in-vivo* however there was no further description of the anterior PARs known to affect PAR-6 localisation – for instance the scaffold protein PAR-3. Crucially, in the absence of PAR-3, PAR-6 is unable to effectively bind and localise to the anterior pole [76]. Further, the co-localisation experiments of Dickinson et al. indicate that PAR-6 forms different anterior complexes, both dependent on and independent to PAR-3 throughout establishment and maintenance phase [60]. Observations of PAR-6 *in-vivo* indicate the presence of two dynamically opposed PAR-6 complexes: the first PAR-3 associated complex which is able to sense flows and so is crucial for establishment of polarity and the second a diffuse, CDC-42 associated complex necessary for the maintenance of polarity. Tostevin and Howard acknowledged the contrasting effects of the anterior PAR species when modelling mutant phenotypes, implementing the effects of PAR-3 and PAR-6 mutants through differently augmented binding rates of the single anterior pool. However, modelling the membrane-bound protein as a single species omits the different dynamics of these anterior complexes as both proteins are inferred to equally interact with the acto-myosin cortex and diffuse at equal rates.

Seirin-Lee et al. found that PAR interaction with the rho GTPase CDC-42 was indispensable for proper patterning in polarisation [128]. Implementing sensitivity analysis to the parametrisation of multi-component models, the group iteratively modelled both maintenance and establishment of polarisation in networks describing various interactions between CDC-42 and the anterior and posterior PAR proteins. Through evaluation of sensitivity functions, the work highlighted interactions most crucial to polarisation and indicated a key role for the CDC-42/aPAR interaction in both maintenance and establishment phase. Subsequently, pPAR interactions proved to be less critical to polarity maintenance but crucial to polarity establishment. However, modelling assumptions such as the simplification of the PAR proteins to two opposing groups and again not considering their sub-population dynamics limit the applicability of these findings. Further, the interaction with cortical flows is not considered. Inclusion of sub-population dynamics, for instance anterior PARs that respond differentially to flows could affect the outcome

of this analysis. Interestingly, it has been observed that a PAR-6/CDC-42 interaction is required for maintenance of polarity and PAR-3 for polarity establishment - perhaps already indicating how consideration of anterior PAR sub-complexes would inform polarity network design [62].

Recent work by Gesselle et al. modelled the anterior PAR proteins in more detail than previous invocations of the polarity network, turning to focus on the PAR-3/PAR-6/aPKC complex. The model described the scaffold protein PAR-3 binding to the membrane independently where it was able to recruit PAR-6/aPKC, forming the PAR-3/PAR-6/aPKC hetero-dimer which is able to antagonise membrane bound posterior PAR proteins. The posterior protein becomes phosphorylated when antagonised and so must reactivate before being able to rebind to the membrane. Respectively, membrane bound posterior protein antagonises both the PAR-3 protein and the PAR-3/PAR-6/aPKC complex. Differentially, the now cytosolic scaffold protein PAR-3 must dephosphorylate in order to rebind to the membrane, whilst the PAR-6/aPKC complex can rebind to membrane bound PAR-3 immediately. Unlike the models previously discussed, Gesselle et al. modelled the reaction-diffusion system in 3D as the work aimed to uncover the effect of the activation-deactivation cycle on axis selection. The reactivation length, defined by the time to reactivate and the diffusivity of the protein, effectively defined the local concentration of active protein available for rebinding to the membrane. In the case of a prolate spheroid, reminiscent of the shape of the *C. elegans* zygote, should the reactivation length prove too short, the short axis was favoured as a polarity axis. This threshold dependency on reactivation length for successful polarisation was tuned by the ratio of PAR-3 to PKC-3 on the membrane. This bolsters the findings of Goehring et al., who identified a strong dependency on relative protein concentrations on successful polarisation. Additionally, it was found that robust polarisation could not be achieved at low scaffold concentration [48]. This work provided insight into long-axis selection when considering a spontaneously polarising PAR network, identifying constraints on both relative PAR concentrations and relative antagonism. However, it did not consider how these protein concentrations may affect the ability of the cell to respond to a polarising cue,

such as the cortical flows observed *in-vivo*. Spontaneous development through a PAR-2 dependent pathway is redundant and cannot polarise the cell on a biological time-scale, with the time to reach a polarised steady state exceeding 40 minutes [70].

4.1.2 Design principles in reaction-diffusion models of the PAR proteins

Reaction-diffusion modelling has proved a powerful tool to probe the design principles of polarisation. Building on the work of predecessors, the models described above (section 4.1) have uncovered many such principles that lead to successful polarisation:

- Rearrangement of the acto-myosin cortex can provide a sufficient cue to initiate polarisation, through either direct interaction (Tostevin and Howard 2008) or by passive advection through cortical flows (Goehring et al. 2011)
- In a wave-pinning model, mass-conservation enables the system to stall the propagating wave-front through depletion of a cytoplasmic pool (Mori et al. 2008)
- In a wave-pinning model, super-fast diffusion in the cytosol replaces the function of a global inhibitor (Mori et al. 2008)
- The reaction equations must be bi-stable in character, achieved through non-linear feedback. This can be achieved in the stoichiometry of mutual antagonism (Goehring et al. 2011) or integration of a clustering term (Dawes et al. 2011)

A key strength of mathematical modelling is the ability to simplify complex biochemical networks to enable investigation of the effect of a single design motif. However, such simplifications inherently impose limitations in model application. Most prevalently, modelling is constrained to focus on a single cell-cycle phase such as maintenance phase or description of the PAR proteins confined to two homogeneous, opposing groups. Spontaneous pattern formation is a redundant pathway towards polarisation, and so it is crucial that models describing polarity consider polarisation in response to guiding cues such as cortical flows or acto-myosin destabilisation. As a result, consideration of establishment phase - where the pre-pattern for polarisation is made concrete - cannot be

overlooked [71],[70]. With the foundations laid regarding the interaction between anterior and posterior PARs, attention is turning towards more complex models of PAR polarity [48][128]. A particular focus is drawn to the investigation of the anterior PAR dynamics with questions raised such as:

- How does the phosphorylation-dephosphorylation activation cycle affect successful polarisation? [48]
- How do the anterior proteins interact with other antagonistic proteins, such as CDC-42 or PAR-1? [65]
- How do these interactions affect robustness of polarisation? [128]

The models presented above revealed key design principles needed for successful polarisation in a reaction-diffusion model. Each model highlighted characteristic features paving the way for future explorations, with sequential models integrating characteristic findings of their predecessor, allowing new hypotheses to be tested. Mass conservation, bi-stability, uniformity of an inactive species and sensitivity to an initial perturbation are all principles that define successful polarisation in a reaction-diffusion model. Of particular interest is the wave-pinning description introduced by Mori et al. and implemented by Goehring et al. as this recapitulates not only the spatial profile of polarity formation but also faithfully reproduces this pattern on a biological time-scale for polarisation. As a result, a model of the kind implemented by Goehring et al. provides the foundation for the extended modelling in this thesis and is described in detail in section 4.2.

4.2 A 'simple' 2-PAR model of cell polarity

Of particular interest to this thesis is the 'simple' 2-PAR model of cell polarity demonstrated in the work of Goehring et al. The group combined theory and experiment, utilising microscopy techniques to measure key parameters for their polarising model. The work describes the anterior-posterior proteins as two antagonistic groups, mapping group behaviour to the observed dynamics of PAR-6 and PAR-2 respectively. Crucially,

polarisation is initialised through an advective trigger - the action of cortical flows - which causes bulk transportation of the membrane bound protein in the direction of flow.

Pre-polarisation, the anterior PAR-6 is found in a membrane-bound state whilst the posterior PAR-2 remains cytosolic. During establishment phase, the PAR-6 is transported away from the posterior by cortical flows. In par-2(RNAi) mutant embryos, this same segregation is observed indicating that the initial transport is independent of interaction between the opposing PAR groups. However, this segregation is only transient and once flows cease, in the absence of PAR-2, PAR-6 spreads back towards to the posterior pole [57]. Goehring et al. first moved to mathematically describe the PAR-6 fluorescence profiles observed in par-2(RNAi) mutant embryos, asking whether passive advective flows were sufficient to segregate membrane bound PAR-6 to the anterior. Through experimental investigation, it was ascertained that the Peclet number - a value that describes the ratio of advective motion to diffusive motion - of the PAR proteins was of order unity, indicating that both diffusive and advective dynamics contributed to PAR protein motion equally. As such, the mathematical model describing the evolution of PAR-6 over time combined advection, diffusion and reaction terms that followed simple mass action kinetics as seen in eq. (4.1) below.

$$\partial_t A = D_A \partial_x^2 A - \partial_X (vA) + k_{on,A} A_c - k_{off,A} A \tag{4.1}$$

where D_A is the measured diffusion constant for the anterior species, v is the approximated flow profile across the embryo, A_c is the uniform cytoplasmic concentration, $k_{on,A}$ is the membrane association rate and $k_{off,A}$ the corresponding membrane dissociation rate.

The shape of the *C. elegans* embryo is similar to that of a prolate spheroid which was measured using selective plane microscopy. For modelling simplicity, the embryo was represented in 1-D by approximating the length L as the circumference of the ellipse bisecting the spheroid across the poles. A system of this kind was shown to yield qualitatively similar results to that described in 3-D using prolate spheroidal coordinates, showing the effect of curvature is negligible. It was observed in photo-bleaching exper-

iments that cytoplasmic recovery occurred on an a time-scale an order of magnitude greater than that on the membrane [115]. This illustrated that the cytoplasmic pool is well-mixed and therefore can be modelled as a uniform concentration. Total amounts of PAR protein were experimentally measured, showing that over the period of the first cell cycle PAR protein levels remained approximately conserved. As such, the concentration of the cytoplasmic pool was modelled simply as the total protein amount less that bound to the membrane:

$$n_{A,cyt} = n_{A,tot} - n_{A,mem} \tag{4.2}$$

where $n_{A,cyt}$ is the number of cytosolic proteins, $n_{A,tot}$ is the total protein number and $n_{A,mem}$ is the number of membrane bound proteins (of type A). When considering the cell as a prolate spheroid, this would resolve to the following equations of measurable quantities:

$$n_{A,cyt} = V_{cell}\rho_{A,V} = \frac{4\pi}{3}{R_1}^2 R_2 \rho_{A,V} \tag{4.3}$$

and using Knud's approximation for the surface area of an ellipse,

$$n_{A,mem} = S_{cell}\rho_{A,S} = 4\pi\left(\frac{{R_1}^{1.6}.6 + 2{R_1R_2}^{1.6}}{3}\right)^{\frac{1}{1.6}}\rho_{A,S} \tag{4.4}$$

where $\rho_{A,S}, \rho_{A,V}$ are the measured surface and volume densities of protein A respectively and R_1, R_2 is the measured length of the minor and major axes of cell respectively.

A flow profile was approximated from Particle Image Velocimetry analysis of NMY-2 fluorescence images. This cortical flow was then implemented in the simulated establishment phase, with a no-flow regime implemented at any time-point outside this window. In a no-flow regime, the PAR system is instead represented by reaction-diffusion alone. Initialising the system with a uniform distribution of aPAR the reaction-advection-diffusion system described above revealed that cortical flows were sufficient to displace PAR-6, with simulation results matching that observed in the complementary fluorescence experiments. As in experiment, PAR-6 is only transiently displaced in PAR-2(RNAi) mutant

embryos. This can be seen in fig. 4.1: as flows occur aPAR is displaced to the anterior remaining there until flows cease. Following this aPAR expands back towards the posterior, again reaching the initialised uniform steady state as its long term solution.

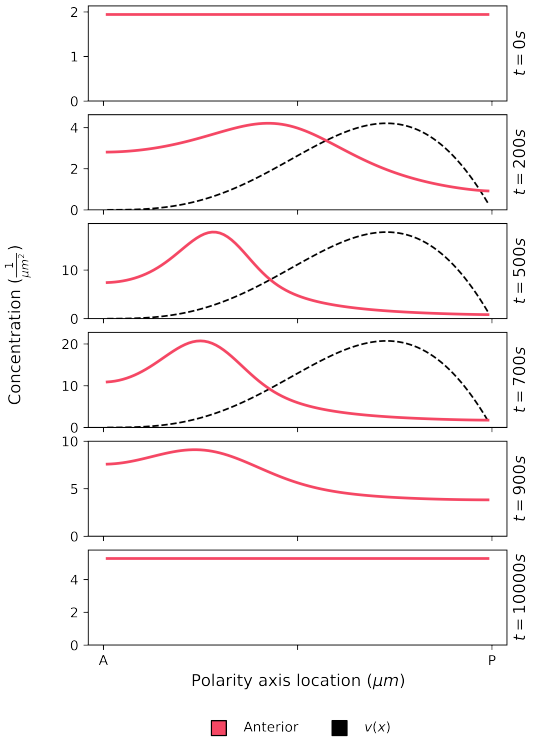


Figure 4.1: The anterior PAR proteins can respond to flows in the absence of posterior PAR proteins.PAR-6 profiles in a simulated par-2(RNAi) mutant embryo. During establishment phase, PAR-6 is segregated to the anterior (middle panels). In PAR-2 mutant embryos, this segregation is transient with PAR-6 spreading back towards the anterior when flows cease (bottom panels).

Having illustrated that cortical flows are sufficient to transiently displace aPAR along the polarity axis, the group next set out to investigate the mechanism by which transient flows can give rise to stable polarisation. In order to achieve this, the anterior system must be coupled with a mutually antagonistic posterior partner - PAR-2. The dynamics of PAR-2 are both observed and modelled to be similar to those of PAR-6: when membrane-bound, the proteins laterally diffuse and respond to cortical flow. As such a mathematical system is set up similarly to that used to describe aPAR. Additionally, both species now interact and compete with each other via mutual antagonism. A schematic describing the PAR reactions can be found below in fig. 4.2.

The system of equations describing the reaction-advection-diffusion model are as

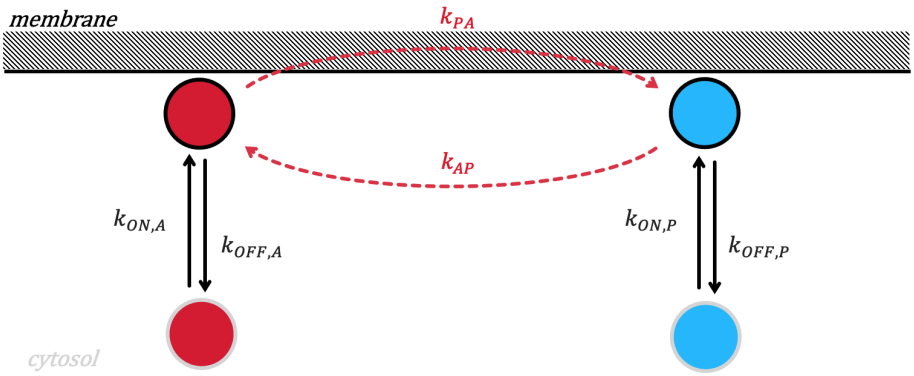


Figure 4.2: Schematic of the 'simple' 2-PAR model Anterior (red) and posterior (blue) proteins bind and dissociate from the membrane with characteristic rates. When bound to the membrane, the proteins freely diffuse. Mutual antagonism enhances dissociation of the opposite species. This interaction is key to enable to maintenance of domain profiles.

follows:

$$\partial_t A = D_A \partial_x^2 A - \partial_X (vA) + k_{on,A} A_c - k_{off,A} A - k_{AP} A P^{\alpha} \tag{4.5}$$

The additional term describes the interaction between A and P with k_{AP} representing the antagonism rate of A by P. The power α (or β, below) describes the stoichiometry of the antagonistic interaction. The corresponding dynamics for the posterior species are described as:

$$\partial_t P = D_P \partial_x^2 P - \partial_X (vP) + k_{on,P} P_c - k_{off,P} P - k_{PA} P A^{\beta} \tag{4.6}$$

The membrane-bound species exchange with their respective cytoplasm, describing a conserved, closed system. The equations describing this exchange are described below:

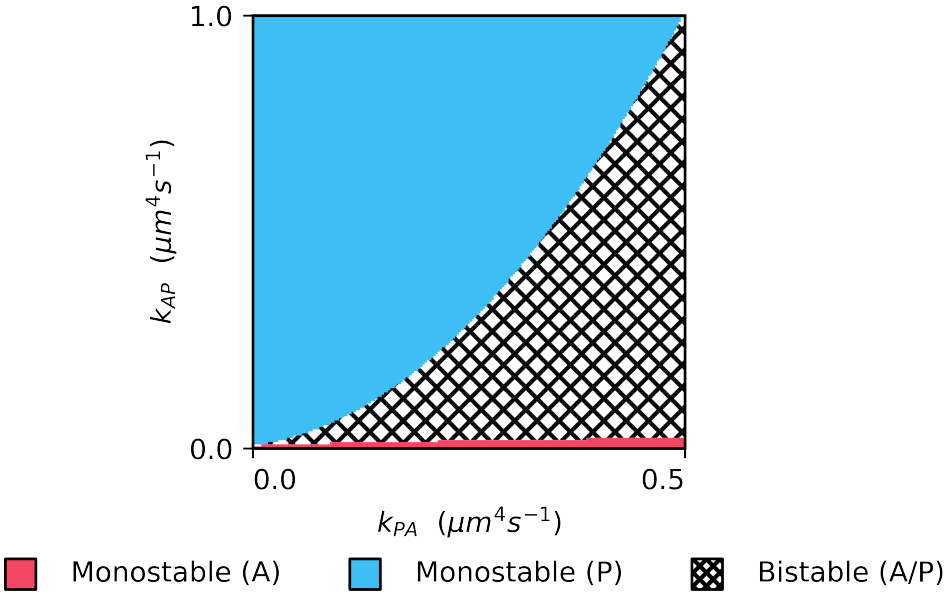
$$\partial_t A_c = D_{A_c} \partial_x^2 A_c - k_{on,A} A_c + k_{off,A} A + k_{AP} A P^{\alpha} \tag{4.7}$$

$$\partial_t P_c = D_{P_c}\partial_x^2 P_c - k_{on,P}P_{cyt} + k_{off,P}P + k_{PA}PA^{\beta} \tag{4.8}$$

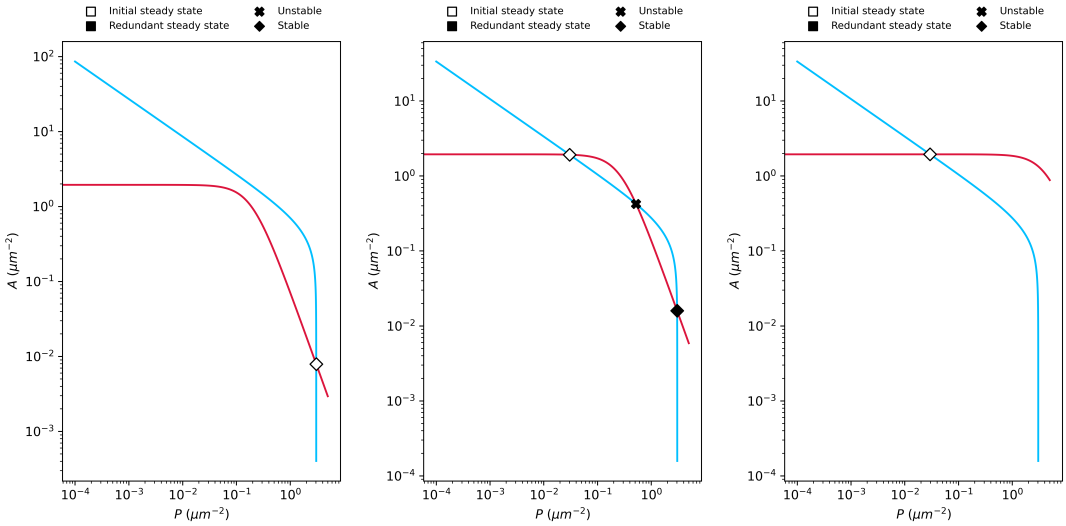
The antagonistic interaction term introduces bi-stability to the system when the stoichiometry is sufficiently non-linear. As a result, the system can maintain multiple steady states; a homogeneous anterior dominant state, a posterior dominant state or a polarised state where anterior dominant and posterior dominant regions are separated in space and share only a boundary. Investigation of the antagonistic parameter space showed that at steady state, the polarisation model described above can support mixed states both mono-stable and multi-stable (see fig. 4.3). Importantly, a region of parameter space could support both a stable anterior dominant homogeneous state and a stable polarised state; reflecting the dynamic states of polarisation in the embryo. The transition between these two states, however, required a perturbation above a certain threshold for which cortical flows were implicated. A threshold perturbation of this kind ensures the system remains robust to small fluctuations, polarising only when the fluctuation exceeds a critical size.

Numerical simulations revealed that cortical flows initially displaced aPAR from the posterior as in Figure 4.1. As a result of this clearance, the otherwise cytosolic pPAR could now bind to the membrane in the region where aPAR had been cleared by flows. This initially small posterior domain then expanded in size throughout establishment phase before relaxing back to steady state throughout maintenance phase, once flows had ceased. This series of events, shown in fig. 4.4a, closely reflected those observed *in-vivo*. It was noted that the system could polarise in the absence of flows, should there be an initial clearance of aPAR from the posterior pole. This represented a redundant 'rescue' pathway observed *in vivo*, where polarisation occurs more slowly. Moreover, polarisation in this manner lacked the hallmark qualities of leading edge enrichment and initial posterior over-expansion, allowing the group to deduce that the pattern of polarisation observed *in vivo* was solely a result of triggering by advective flows.

As demonstrated in Figure 4.4b where the initial state of the system is artificially polarised, the form of the final polarised steady state is independent of the initial pertur-



(a)



(b) **(c)** **(d)**

Figure 4.3: Linear stability analysis reveals the multi-stable character of the 2-PAR model of PAR polarity. **(a)** A phase-space portrait illustrates the stability of the 2-PAR system for a range of k_{AP}, k_{PA} parameterisations. **(b)** The system can yield a mono-stable posterior dominant state. **(c)** Certain parametrisations of the mutual antagonism parameters yield a multi-stable state. Here, both stable posterior and anterior dominant states are achievable. These states are separated by an unstable transient state. **(d)** The system can yield a mono-stable anterior dominant state.

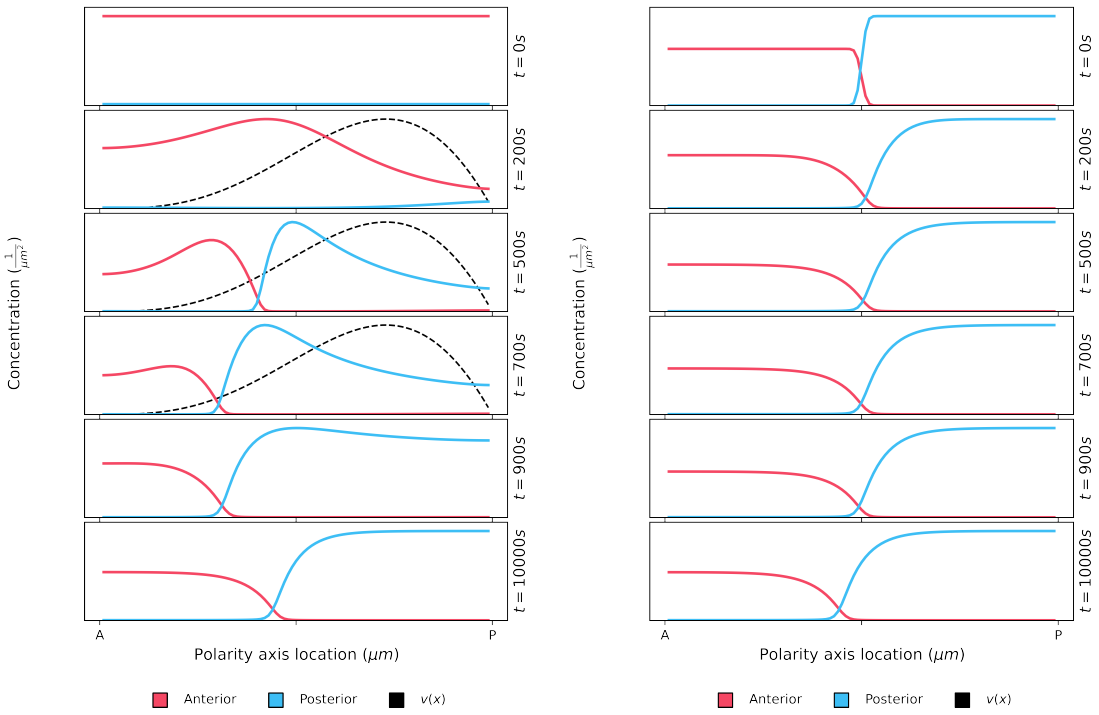


Figure 4.4: The 2-PAR model can both establish and maintain domains. The 2-PAR model is able to **(a)** respond to flows to establish polarity. **(b)** maintain a polarised domain.

bation. Instead, the final steady state was found to depend on front-stalling behaviour as a result of depletion of the cytoplasmic pool and conserved protein amounts. The group confirmed these results by first measuring the fluorescence of PAR-2 in the cytoplasmic pool, observing that cytoplasmic depletion coupled with domain growth. To this end, reduction of overall PAR-6 levels in embryos with only one functional gene copy or over-expression of PAR-2 in mutant wild-type embryos were shown to increased the size of the PAR-2 domain. Using RNAi interference, this level of domain over- or under- expansion could be tuned through adjustment of overall protein expression.

Together, this work demonstrated that cortical flows provided a sufficient cue to break symmetry within the cell, initiating the polarisation process. Polarisation in this way through passive advection couples both the PAR system and the cortex in an actin-independent manner. This is unlike the work of Tostevin and Howard, where polarisation is directly dependent on acto-myosin asymmetry [129]. Following the initial establishment phase, maintenance of polarity is achieved through mutual antagonism of the PAR species.

This reflects the findings of previous experimental work which revealed that PAR proteins exchanged with a well-mixed cytoplasm and diffused laterally on the membrane. In this manner polarisation was maintained through the ability of the PAR proteins to locally modulate the binding affinity of the opposing PAR species. Should the PAR proteins be sufficiently segregated during establishment phase through response to the polarising cue, then this antagonistic behaviour enables domains to prevail. Importantly, for such a process to stably occur then the polarising system must be multi-stable in character. In this work, this is achieved through non-linearity in the stoichiometric terms governing the antagonistic reactions. However, bi-stability can be achieved through other functional mechanisms such as PAR-3 oligomerisation described in the work of Dawes and Munro (see section 4.1 for further details).

4.3 An extended model of cell polarity; the aPKC cycle

Mutual antagonism between the opposing PAR protein groups has been illustrated as a core component for stable polarisation in the PAR system. This interaction is therefore omnipresent in models of cell polarity but is most frequently implemented as a non-linear reaction between two opposing groups representing the anterior and posterior proteins respectively. This simplification has allowed for other key components of cell polarisation to be unveiled, such as the coupling of the PAR proteins to passive advective flows to establish polarisation. With these core principles of polarisation uncovered, future work must turn to modelling the PAR network in increasing detail to distil the design principles that underpin the complex PAR network that is observed *in-vivo*.

The anterior PAR proteins co-localise to varying degrees at different points in the cell-cycle and have been observed to form dynamically opposed PAR-6/CDC-42/aPKC and PAR-6/PAR-3/aPKC complexes. The formation of PAR-3 associated PAR-6/akp-c complex is upregulated during establishment phase and subsequently down-regulated by the polo-like kinase PLK-1 as cortical flows cease [60]. In mutant embryos where PAR-3 is depleted, PAR-6/apkc was no longer observed in oligomeric complexes on the mem-

brane. In wild-type zygotes, the distribution of PAR-6/aPKC oligomer sizes matched the distribution of PAR-3 sizes, indicating that PAR-3 could act to recruit PAR-6/aPKC to the cortex. PAR-3 complexes were brightest during establishment phase and co-localised with PAR-6, consistent the results of Munro et al. [45]. Embryos containing only a monomeric pool of PAR-3 were unable to polarise successfully, and consequently failed to segregate PAR-6 to the anterior pole [60]. Clustering has been to evidenced as a mechanism to enhance stability of polarisation and to modulate the overall dynamics of constituent complexes, primarily through slowed diffusivity [65][116][118]. The PAR-3/PAR-6/aPKC complex has therefore been indicted in the role of a cue-deriving module, with clustering of PAR-3 indispensable for flow-sensing and the propagation of spatial information during establishment phase when the pre-pattern of polarisation is formed.

The work of Gesselle et al. further investigated the role of sub-complexes of the anterior proteins, illustrating how cycling between a phosphorylated (inactive) and desphosphorylated (active) form of the scaffold protein PAR-3 can affect the choice of polarity axis in 3D simulations. Dephoshorylated PAR-3 recruited PAR-6/aPKC to the membrane, in line with the *in-vivo* observations of Dickinson et al. [60]. The PAR-3/PAR-6/aPKC was then phosphorylated by the kinase action of the posterior PAR, causing it to dissociate from the membrane and rejoin the cytosol as its constituent components. In turn, the PAR-3/PAR-6/aPKC complex could phosphorylate the posterior PAR through the kinase action of aPKC, causing its removal from the membrane. However, experiments in-vitro have shown that mammalian PAR-3 instead acts an inhibitor of aPKC activity [59][78]. In the context of the extended anterior polarity model presented by Gesselle et al., this inactivation would render the anterior complex unable to phosphorylate the posterior protein and hence unsuccessful polarisation.

Recent work by Rodriguez et al. has shed light on the activity of aPKC in the context of an extended anterior network, reporting that manipulation of PKC-3 activity biases PAR-6 complex formation to either PAR-3 association or CDC-42 dependent complexes. Imaging of PKC-3 revealed that unlike PAR-3, PKC-3 could form clusters but that there was significant diffuse pool of PKC-3. This observation led to the hypothesis of two

distinct patterning phases for the anterior PARs; the first where PAR-3/aPKC/PAR-6 localise in a clustered formation, undergoing translocation by flows and becoming anteriorly localised. During establishment phase, Rodriguez et al. found that in pkc-3 inhibited zygotes PAR-3 is able to segregate to the anterior pole whilst PAR-6/aPKC remain distributed across the cortex indicating that pkc-3 activity is necessary for tight coupling of PAR-6/PAR-3. Following establishment phase, PAR-3 remains clustered whilst PAR-6/PKC-3 become a diffuse pool that localises with CDC-42. Whilst in this CDC-42 associated complex, aPKC is active and the PAR-6/CDC-42/aPKC complex is able to antagonise the posterior PAR enhancing its removal from the membrane. In CDC-42 depleted zygotes, PAR-6/aPKC segregate to the anterior as in wild-type, however this initial asymmetry is lost throughout maintenance phase [110]. Together these results indicate that both CDC-42 and PAR-3 are necessary for stable association and localisation of PAR-6/aPKC to the membrane throughout polarisation. Cycling of aPKC activity in the manner proposed by Rodriguez et al. would provide a link between the spatial cues derived from PAR-3 cluster segregation and the anterior localisation of aPKC activity which enables domain maintenance - see fig. 4.5.

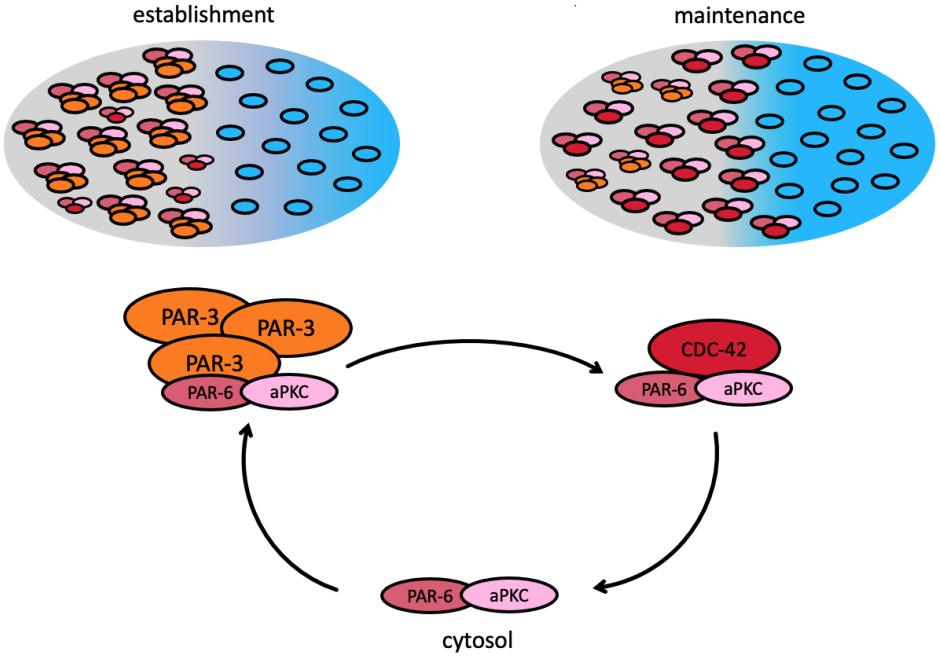


Figure 4.5: Schematic of the aPKC cycle. aPKC cycles between an active and inactive state, where it associates with PAR-6/PAR-3 and PAR-6/CDC-42 to form functionally distinct complexes. Preferential coupling to either heterodimer would enable to cell to favour functionally advantageous states at different times in the cell cycle. In establishment phase, the favouring of the PAR-3 complex could increase sensitivity to the polarising cue. In maintenance phase, upregulation of the active PAR-6/CDC-42 associated complex would enable domain maintenance through antagonism.

4.3.1 Open Questions

Consistent with many of the observed phenotypes in mutant zygotes, the aPKC cycle presented in the work of Rodriguez et al. provides a plausible, coherent network description of polarisation in *C. elegans*. Additionally, the model simplistically describes separate anterior modules that encompass key players in the anterior molecular circuit - PAR-3 and CDC-42. With PAR-3 and CDC-42 proving indispensable in, a model where PAR-6/aPKC cycles between PAR-3 and CDC-42 associated complexes can account for co-localisation observations *in-vivo* [60]. Additionally, there is a clear dynamic conflict in the description of the anterior PARs as a single characteristic group which can be overcome by splitting the segregating dynamic behaviour into the two opposing PAR-3 and CDC-42 associated species.

The ability to respond to flows provides an advantage to patterning through estab-

lishment phase, with PAR-3 clustering observed to be upregulated during this period in the cell cycle. However, increased clustering decreases diffusivity and so a model which is inflexible to down-regulating PAR-3/PAR-6/aPKC in favour of a diffusive, active state (CDC-42/PAR-6/aPKC) is unlikely to prove robust in polarisation [60]. In which case, what design principles underpin a successful PAR polarity network with an aPKC cycle motif? And perhaps more importantly, how do these conditions fit within a polarisation process that is already defined to require; bi-stable reaction terms through mutual antagonism, a sensitivity to a perturbing cue to initialise polarisation and mass-conservation for domain stalling?

This second thesis section aims to compare and contrast two biologically viable, distinct network topologies describing the anterior aPKC cycle. Generally, we aim to uncover the design principles associated with anterior switching between a flow-sensing, inactive and diffuse, active state. Specifically, we address questions pertaining to the design principles of such networks:

Is a polarity model with an anterior aPKC cycle able to polarise in a biologically meaningful way when switching between a flow-sensing and active state?

- Many models of PAR polarity exist, each with varying modelling assumptions or focus on cell-cycle specific phases. These are discussed in detail in section 4.1. The aPKC cycle enables the consolidation of opposing dynamics and functionalities of the anterior complexes through protein cycling. Decoupling the anterior proteins in this way must prove advantageous to the PAR system and as a result, the system must be able to polarise in both establishment (inactive, flow-sensing PAR-3/PAR-6/aPKC upregulated) and maintenance (active, diffuse CDC-42/PAR-6/aPKC upregulated) phase. The features of such a polarisation must recapitulate that observed during polarisation *in-vivo*.

How sensitive are the aPKC cycles to changes in relative diffusion?

- Membrane-bound PAR proteins diffuse laterally across the cortex. During polari-

sation, mutual antagonism between the anterior and posterior proteins maintains the domain boundary as the opposing protein diffuses freely into the domain. The decoupling of active and diffusive behaviours in the aPKC description of the anterior PAR proteins is likely to enhance sensitivity to relative PAR dynamics when considering the stabilisation of the domain boundary.

What are the limitations to success imposed by network design of the aPKC cycle?

- More generally, we look to identify features of the extended polarity networks that enable polarisation. In turn, it is fruitful to identify network limitations particularly from the perspective of integration of network constraints with previously identified polarity design principles: sensitivity to perturbation, mass-conservation and a multi-stable character.

Does the aPKC cycle provide enhancement in robustness of polarisation?

- Polarisation in the *C. elegans* zygote is a process that has been conserved over many generations of development. Additional complexity is costly in a biological circuit and therefore increased complexity is usually attributable to endowing some benefit to the system. We therefore consider whether the addition of the aPKC cycle enhances the robustness of the polarisation process.

4.3.2 Motivation of modelling choices

The 'simple' 2-PAR model (section 4.2) reproduces many of the hallmarks of polarisation in the *C. elegans* zygote, whilst describing the PAR polarity network in a mechanistically simple fashion. As a result, a reaction-advection-diffusion model of this kind forms the basis of the polarity models presented in this thesis. We implement an advectively-triggered reaction-diffusion model of the PAR protein system, passively coupling the reaction network to cortical flows. Unlike the model of Tostevin et al., we do not incorporate feedback between the acto-myosin dynamics and PAR-3 cluster transport within our models of polarisation. This assumption means that during establishment phase, the

cortical flow profile remains fixed and is not locally enhanced in response to an increase in the local membrane concentration of anterior protein.

In our model of cell polarity, we describe the PAR proteins as passively advected, mutually-antagonistic protein groups alike the model introduced by Goehring et al. Additionally, we construct the anterior protein network to represent the hypothesised aPKC cycle of Rodriguez et al.. To this end, we introduce two distinct dynamic complexes to the anterior network, a PAR-3/PAR-6/aPKC complex which can 'sense' and be advected by cortical flows and a CDC-42/PAR-6/aPKC complex which is diffuse and able to antagonise posterior protein.

We motivate our modelling choices as follows:

1. We retain the modelling choice of Goehring et al. that the posterior proteins function as a single group. Sailer et al. find that CHIN-1/PAR-1 act redundantly to maintain PAR-6 asymmetry and it has been shown that PAR-2 works to recruit PAR-1 to the membrane [65]. As PAR-2 diffusion and reaction rates have been explicitly measured, we therefore take the simplification of selecting PAR-2 to represent our posterior species [115][70].

2. Considering the experimental results of Dickinson et al., who observed two distinct PAR-6 populations we choose to extend our modelling to capture the behaviour of these two complexes. We take inspiration from the description of the aPKC cycle presented by Rodriguez et al. whereby PAR-6/aPKC associates with the scaffold protein PAR-3, forming a complex that can respond to flows during establishment phase. Here, aPKC is inactive, suppressed by PAR-3 and as such this complex is unable to antagonise posterior protein. PAR-6/aPKC is then converted to a CDC-42 associated protein where aPKC is activated and therefore this complex becomes antagonistic to posterior protein [78].

3. Our investigation into the role of PAR-3 clusters size for efficient translocation (see chapter 2) highlighted multiple functional aspects of clustering that inform our

modelling. Firstly, it was revealed that cluster size is dispensable for efficiency of translocation to the anterior through establishment phase. Therefore, we choose to confine our model to a mean-field description, with the PAR-3 population sensing flow equally. Secondly, PAR-3 clusters do not appear to grow as a result of the physical forces during contraction of the cortex. This bolsters our decision to passively couple PAR-3 dynamics to flow within the cortex and abandon a model of contraction within the acto-myosin cortex. Taken together, these results enable us to approximate an advective flow profile from our investigations of global flow of PAR-3 along the A-P axis.

4. We choose not to explicitly model the positive-feedback loop of the anterior PAR proteins and the cortical flow, instead taking a more simplistic view of the cortical flow as a constant profile. Our investigation of global flow revealed a persistent flow profile throughout the period of peak flow. Goehring et al. previously integrated a spatio-temporally measured flow profile into their simulations which would intrinsically represent these density dependent changes in cortical velocity. It was noted that the inclusion of this realistic velocity profile did not significantly affect the resultant PAR profiles when considered within the framework of a simplified 1D geometry [70]. For this reason, we passively advect PAR-3 clusters in our model of polarity. Whilst out of the scope of this thesis, direct modelling of the PAR-3/NMY-2 feedback loop could be an interesting future point of research if focus was drawn to simulating the role of the acto-myosin cortex on PAR-3 clustering at a local scale.

4.3.3 Reaction pathways for PAR polarity model with an aPKC cycling motif

The model of aPKC cycling proposed by Rodriguez et al. defines a network where PAR-6/aPKC is able to form functionally specialised complexes with differential dynamic behaviours and activity levels. Such a model conceptually overcomes possible molecular limitations faced by a system in which the anterior components must be sensitive to

perturbation by flow (advective in character) and transduce signals across the membrane (diffuse in character). However, the exact design of this biochemical system remains unclear. In this section, we introduce the reader to two possible network designs to describe the aPKC cycle. The first network - the coupled model - describes a system where PAR-6/aPKC is only able to bind to the membrane via the scaffold protein PAR-3. In this manner, PAR-3 and PAR-6/aPKC are spatially coupled. The second network - the uncoupled model - describes a system where PAR-6/aPKC membrane binding is uncoupled from PAR-3. Unlike the coupled model PAR-6/aPKC is able to form an active complex on the membrane without first conversion from a PAR-3 associated complex, uncoupling the PAR-3 and PAR-6/aPKC dynamics. Rather than gating creation of an active complex on the membrane, the presence of PAR-3 instead works to enhance membrane association of PAR-6/aPKC in an active form. Notably, in both models, PAR-6/CDC-42/aPKC does not undergo bulk motion as a result of cortical flows. In line with our experimental investigations, recent work has indicated that PAR-3 is able to modulate its sensitivity to bulk motion by clustering to slow its inherent diffusivity [118]. Considering the Peclet number - the ratio of advective to diffusive motion it can be concluded that through this mechanism, clustered PAR-3 favours bulk motion. Comparatively, the unclustered fast-diffusing PAR-6/CDC-42/aPKC complex is unable to effectively slow its diffusion and thus remains comparatively insensitive to the advective flows of the cortex.

4.3.3.1 The coupled PAR polarity model

The coupled model represents the simplest extended network investigated in this thesis. This network contains a simple, cyclic topology whereby PAR-6/aPKC is recruited to the membrane solely via PAR-3 before dissociating and forming a complex with available CDC-42 on the membrane, before dissociating from the membrane into the cytoplasm.

The equations below outline the modelled interactions of the coupled model. We model two anterior, membrane bound complexes A_3 (eq. (4.9)) and A_{42} (eq. (4.10)) which represent PAR-3/PAR-6/aPKC (inactive) and CDC-42/PAR-6/aPKC (active) respectively.

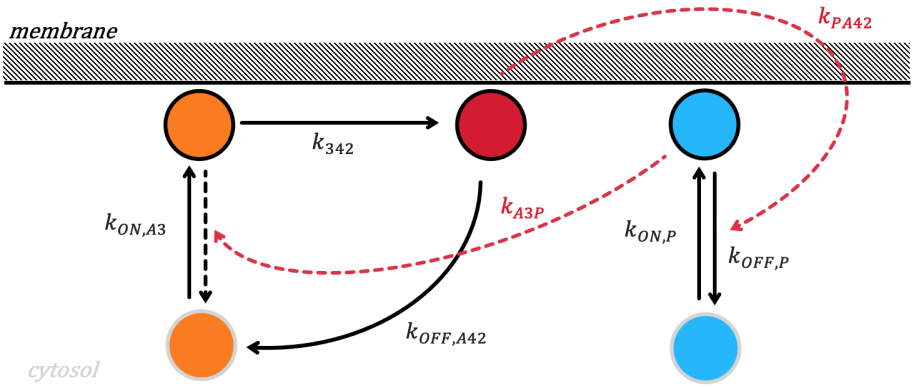


Figure 4.6: Schematic of the coupled PAR model. The PAR-6/aPKC binds to the membrane via the scaffold protein PAR-3 to form the flow-sensing, inactive, anterior complex PAR-3/PAR-6/aPKC (orange). With some characteristic rate, k_{342}, PAR-6/aPKC dissociates from PAR-3 and forms the diffusive, active complex (CDC-42/PAR-6/aPKC) (red) before dissociating back to the cytosol. In this active state, CDC-42/PAR-6/aPKC is able to antagonise the membrane-bound posterior (blue) species. This species binds and unbinds to and dissociates from the membrane with a characteristic rate. In turn, the membrane-bound posterior species is able to antagonise the inactive PAR-3/PAR-6/aPKC complex. When bound to the membrane, all proteins freely diffuse. Only PAR-3/PAR-6/aPKC and pPAR are sensitive to flows during establishment phase.

$$\frac{\partial A_3(x,t)}{\partial t} = D_{A3}\frac{\partial^2 A_3(x,t)}{\partial x^2} - \frac{\partial (v(x)A_3(x,t))}{\partial x} + \psi k_{ON,A3}A_c(x,t) - k_{342}A_3(x,t) - k_{A3P}A_3(x,t)P(x,t)^{\alpha} \tag{4.9}$$

$$\frac{\partial A_{42}(x,t)}{\partial t} = D_{A42}\frac{\partial^2 A_{42}(x,t)}{\partial x^2} + k_{342}A_3(x,t) - k_{OFF,A42}A_{42}(x,t) \tag{4.10}$$

PAR-6/aPKC initially binds to the membrane at rate $k_{ON,A3}$ via a PAR-3 cluster of size n. As the protein binds from the volume of the cytosol to the surface area of the membrane, the normalisation constant ψ represents the surface to volume ratio. When associated with PAR-3, PAR-6/aPKC undergoes bulk motion as a result of the PAR-3 molecule being passively advected by cortical flows. Such bulk motion is represented by

the advective term $\frac{\partial(v(x)A_3(x,t))}{\partial x}$, showing an interaction with the spatially varying velocity. The diffusion on the membrane of the PAR-3 associated molecule is slow (D_{A3} is small) and so the PAR-3 associated molecule provides spatial information to the system as a result of segregation by flows during establishment phase. Endowing the system with the feature of bi-stability, mutual antagonism exists between the anterior and posterior species. When in a complex with PAR-3, aPKC is inactive and so PAR-3/PAR-6/aPKC is to removal from the membrane via an antagonistic interaction with pPAR. The activity of pPAR, k_{A3P} and the stoichiometric term α define the strength of this interaction. When membrane bound, PAR-6/aPKC dissociates from PAR-3 and instead associates with CDC-42 at a rate k_{342}. In this state, CDC-42/PAR-6/aPKC quickly diffuses on the membrane ($D_{A6} > D_{A3}$) before eventually dissociating from the membrane and rejoining the cytosol at a rate $k_{OFF,A42}$.

$$\frac{\partial P(x,t)}{\partial t} = D_P \frac{\partial^2 P(x,t)}{\partial x^2} - \frac{\partial (v(x)P(x,t))}{\partial x} + \psi k_{ON,P} P_c(x,t) - k_{OFF,P} P(x,t) - k_{PA42} P(x,t) A_{42}(x,t)^{\beta} \tag{4.11}$$

With reference to eq. (4.11), we model the posterior protein as associating and dissociating from the membrane with intrinsic rates $k_{ON,P}$ and $_{OFF,P}$. When associated with CDC-42/PAR-6, aPKC is active and therefore this species is able to antagonise the posterior PAR, driving its removal from the membrane with a rate dependent on the activity of aPKC, k_{PA42} and the stoichiometry of this interaction, β. As with the PAR-3 associated complex and similarly to the 'simple' 2-PAR model we choose to model the posterior protein as being sensitive to flows and so include the advective term dependent on the cortical velocity, $v(x)$ [70].

Mass-conservation within the anterior and posterior species means that all protein that dissociates from the membrane rejoins the cytosolic pool of the respective species. This creates the following reaction equations (eq. (4.12), eq. (4.13)) describing the dynamics of cytosolic proteins - where the reaction terms are equal and opposite to the binding/unbinding/antagonistic terms described in the membrane equations above. To

ensure a well mixed cytoplasm, the diffusivities of the cytoplasmic components D_{A_c}, D_{P_c} are super-fast.

$$\frac{\partial A_c(x,t)}{\partial t} = D_{A_c}\frac{\partial^2 A_c(x,t)}{\partial x^2} - \psi k_{ON,A_3} A_c(x,t) + k_{OFF,A42} A_{42}(x,t) + k_{A3P} A_3(x,t) P(x,t)^{\alpha} \quad (4.12)$$

$$\frac{\partial P_c(x,t)}{\partial t} = D_{P_c}\frac{\partial^2 P_c(x,t)}{\partial x^2} + k_{OFF,P} P(x,t) - \psi k_{ON,P} P_c(x,t) + k_{PA42} P(x,t) A_{42}(x,t)^{\beta} \quad (4.13)$$

where the advective flow speed, visualised in fig. 4.9, is denoted by:

$$v(x) = \begin{cases} cx^2 \sin\left(\frac{2\pi x}{L}\right), & \text{if } 120\,\text{s} < t \leq 660\,\text{s} \\ 0, & \text{otherwise} \end{cases} \quad (4.14)$$

4.3.3.2 The uncoupled PAR polarity model

When describing the anterior PAR dynamics in the uncoupled model, the dependence on PAR-3 for the creation of active CDC-42/PAR-6/aPKC is relaxed. Instead, PAR-6/aPKC binds to the membrane independently but the rate of this association is enhanced in the presence of PAR-3.

The equations below outline the modelled interactions of the uncoupled model. We again model two anterior, membrane bound species: A_3 denotes PAR-3 on the membrane (eq. (4.16)) and A_6 denotes the active CDC-42/PAR-6/aPKC complex (eq. (4.15)). PAR-6/aPKC membrane binding is upregulated in a manner dependent on the concentration of membrane-bound PAR-3.

$$\frac{\partial A_6(x,t)}{\partial t} = D_{A6}\frac{\partial^2 A_6(x,t)}{\partial x^2} + \psi^{-1} k_{ON,A6} A_3(x,t) A_{c6}(x,t) - k_{OFF,A6} A_6(x,t) \quad (4.15)$$

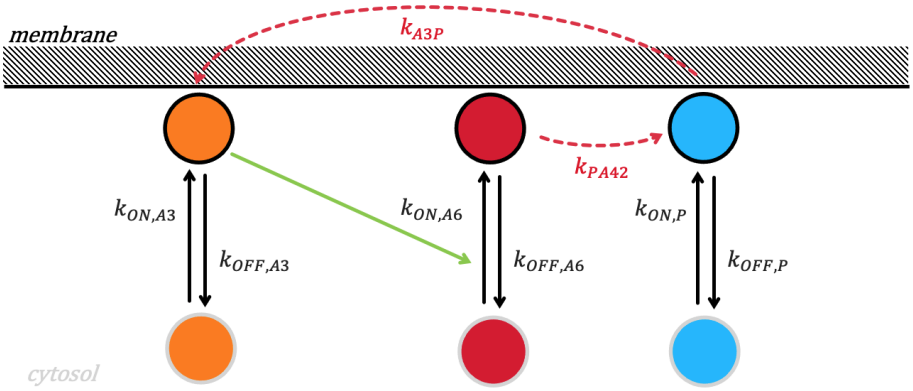


Figure 4.7: Schematic of the uncoupled PAR model. PAR-6/aPKC binds to and dissociates from the membrane with a characteristic rate. When membrane-bound, it forms an active complex with CDC-42 (red). This complex is able to antagonise the membrane-bound posterior species (blue). The posterior species binds and unbinds from the membrane with a characteristic rate. When membrane-bound, pPAR is able to antagonise the clustering PAR-3 species (orange), up-regulating its removal from the membrane. Membrane bound PAR-3 acts to enhance PAR-6/aPKC membrane binding. When bound to the membrane, all proteins freely diffuse. Only PAR-3 and pPAR are sensitive to flows during establishment phase.

$$\frac{\partial A_3(x,t)}{\partial t} = D_{A3}\frac{\partial^2 A_3(x,t)}{\partial x^2} - \frac{\partial (v(x)A_3(x,t))}{\partial x} + \psi k_{ON,A3}A_{c3}(x,t) - k_{OFF,A3}A_3(x,t) - k_{A3P}A_3(x,t)P(x,t)^{\alpha} \tag{4.16}$$

PAR-6/aPKC binds to the membrane at rate $k_{ON,A6}$, where it quickly diffuses and dissociates with an intrinsic rate $k_{OFF,A6}$. As the protein binds from the volume of the cytosol to the surface area of the membrane, the normalisation constant ψ represents the surface to volume ratio. In the presence of PAR-3, association of PAR-6 to the membrane is enhanced. PAR-3 forms clusters of size n which bind to the membrane with rate $k_{ON,A3}$. PAR-3 clusters undergo bulk motion which is represented by the advective term $\frac{\partial (v(x)A_3(x,t))}{\partial x}$, showing an interaction with the spatially varying velocity described in eq. (4.14). The diffusion on the membrane of the PAR-3 clusters is slow ($D_{A3} < D_{A6}$)

and so the PAR-3 associated molecule provides spatial information to the system as a result of segregation by flows during establishment phase. PAR-3 eventually dissociates from the membrane with intrinsic rate $k_{OFF,A3}$. Additionally, PAR-3 is susceptible to antagonism by pPAR which enhances PAR-3 dissociation from the membrane back into the cytoplasmic pool. The activity of pPAR, k_{A3P} and the stoichiometric term α again define the strength of this interaction.

$$\frac{\partial P(x,t)}{\partial t} = D_P \frac{\partial^2 P(x,t)}{\partial x^2} - \frac{\partial (v(x)P(x,t))}{\partial x} + \psi k_{ON,P} P_c(x,t) - k_{OFF,P} P(x,t) - k_{PA42} P(x,t) A_6(x,t)^{\beta} \tag{4.17}$$

With reference to eq. (4.17), we model the posterior protein as associating and dissociating from the membrane with intrinsic rates $k_{ON,P}$ and $_{OFF,P}$. When associated with CDC-42/PAR-6, aPKC is active and therefore this species is able to antagonise the posterior PAR, driving its removal from the membrane with a rate dependent on the activity of aPKC, k_{PA42} and the stoichiometry of this interaction, β. As with the PAR-3 associated complex and similarly to the 'simple' 2-PAR model we choose to model the posterior protein as being sensitive to flows and so include the advective term dependent on the cortical velocity, $v(x)$ [70].

Mass-conservation within the anterior and posterior species means that all protein that dissociates from the membrane rejoins the cytosolic pool of the respective species. This creates the following reaction equations (eq. (4.18), eq. (4.19), eq. (4.20)) describing the dynamics of cytosolic proteins - where the reaction terms are equal and opposite to the binding/unbinding/antagonistic terms described in the membrane equations above. To ensure a well mixed cytoplasm, the diffusivities of the cytoplasmic components $D_{A_c}3$, $D_{A_c}6$, D_{P_c} are super-fast. Differentially from the coupled model, there are two anterior cytosolic pools describing both cytosolic PAR-3 (A_{c3}) and cytosolic PAR-6 (A_{c6}).

$$\frac{\partial A_{c3}(x,t)}{\partial t} = D_{A_{c3}} \frac{\partial^2 A_c(x,t)}{\partial x^2} - \psi k_{ON,A3} A_{c3}(x,t) + k_{OFF,A3} A_3(x,t) + k_{A3P} A_3(x,t) P(x,t)^{\alpha} \tag{4.18}$$

$$\frac{\partial A_{c6}(x,t)}{\partial t} = D_{A_{c6}} \frac{\partial^2 A_{c6}(x,t)}{\partial x^2} - \psi^{-1} k_{ON,A6} A_3(x,t) A_{c6}(x,t) + k_{OFF,A42} A_6(x,t) \tag{4.19}$$

$$\frac{\partial P_c(x,t)}{\partial t} = D_{P_c} \frac{\partial^2 P_c(x,t)}{\partial x^2} + k_{OFF,P} P(x,t) - \psi k_{ON,P} P_c(x,t) + k_{PA42} P(x,t) A_6(x,t)^{\beta} \tag{4.20}$$

Again the advective flow speed, visualised in fig. 4.9, is denoted by:

$$v(x) = \begin{cases} cx^2 \sin\left(\frac{2\pi x}{L}\right), & \text{if } 120\,\text{s} < t \leq 660\,\text{s} \\ 0, & \text{otherwise} \end{cases} \tag{4.21}$$

4.3.3.3 Other plausible models of cell polarity

Experimental observation has revealed distinct populations of anterior protein which are upregulated at different phases of the polarity process: a flow-sensing, slowly diffusing pool is favoured during establishment phase and a quickly diffusing population through maintenance phase. Dickinson et al. probed these populations, observing that PAR-6 localised with the clustered species PAR-3 to form the slowly diffusing population during establishment phase and favoured a CDC-42 associated complex during maintenance phase whilst PAR-3 clusters were downregulated. Crucially, in the absence of PAR-3, PAR-6 cannot localise on the membrane [60]. The spatiotemporal profiles of these sub-populations constrain the possible network topologies that can describe the polarity process.

Previous modelling work, discussed in section 4.1 has outlined overarching network principles underpinning successful polarisation of the *C. elegans* zygote, but none have investigated the networks underpinning the sub-populations of the anterior proteins and the effect of the network design on robust polarisation. Therefore, armed only with temporal observations of anterior sub-populations and the knowledge that PAR-3 is the cornerstone to PAR-6 localisation the design of the protein network remains fairly un-

constrained. Wary of overfitting sloppy parameters (those which have little effect on the behaviour of the system) and given the number of unmeasured and unknown parameters a more complex model would involve we take a cautious approach to our polarity model extensions and choose instead to focus on comparing the suitability of two distinct and fundamental network motifs [130].

Each model features a plausible but uninvestigated mechanism through which the cell would be able to flexibly favour dynamic populations at different times in the cell cycle. Our first model, the coupled model draws on the proposed direct cyclic network put forward by Rodriguez et al. [78]. The second uncoupled model imposes a similar simplistic network design which differentially does not feature the direct cycling proposed by Rodriguez et al. There theoretically exists other, more complex models which would plausibly generate distinct anterior populations. For instance, a combination of the coupled and uncoupled model - where PAR-3 clusters bind independently, whose membrane density drives the binding of PAR-6 to the membrane via a cyclic loop could plausibly describe the observations of PAR-6 sub-populations on the cortex. However with many unknowns, we take the reductionist approach and choose to constrain our investigation to simple models which will inform more complex modelling initiatives and experimental design in the future. The additional extension of the posterior sub-populations remains outside the scope of this thesis, but would form an interesting direction of future research [65].

4.3.4 Parametrising the extended models of polarity formation

For numerical tables of model parameterisations please see section 4.3.4.9. See below for more detailed explanations motivating parameter choices.

4.3.4.1 System parameters

The polarisation of the *C. elegans* zygote was modelled using a 1-D system akin to that discussed in Section 4.2. In this manner the embryo was approximated to be a prolate spheroid where the length, L, of the circumference along the direction of the major axis defined the size of the 1-D system. In this description, previous measurements have

revealed the principle radii of the *C. elegans* zygote to be approximately $27 \times 15 \times 15 \mu m$. This produces a system length, L, of approximately $134.6\,\mu\text{m}$. Equivalent to traversing this circumference, periodic boundary conditions were imposed at $\pm\frac{L}{2}$. Within this system $x = 0$ and $x = \pm\frac{L}{2}$ denoted the anterior and posterior pole respectively.

4.3.4.2 PAR concentrations

In line with experimental observation, PAR protein concentrations remained constant throughout the modelled period of polarisation. Mass conservation therefore imposed that:

$$X_c = \rho_X - \frac{\psi}{L}\int_{-L/2}^{L/2} X_{mem}\,dx \tag{4.22}$$

where X signifies a PAR protein species, L is the system length and ρ_X the total protein concentration. ψ denotes the surface to volume ratio of a prolate spheroid - the geometry we approximate the *C. elegans* to have. As $D_{X,cyt} >> D_{X,mem}$, the cytosolic PAR concentration is assumed to be well-mixed and therefore uniform at all times. Total PAR concentrations were set to the normalised concentrations used in the modelling work of Goehring et al. Based on discussion with the Goehring lab and their experimental observation (2017), total PAR-3 concentration was set to be around half of that of PAR-6.

For homogeneous initial states the initial domain profile $f(x_0)$ was set to be:

$$f(x_0) = X_{ss,hom} \tag{4.23}$$

For polarised initial states the initial domain profile $f(x_0)$ followed the form of a sum of error functions. This describes an initial profile that replicates perfect segregation of protein by cortical flows, where the height of the domain is double that of the homogeneous steady state value.

For the anterior species, the initial profile, $f(x_0)$ was set to be:

$$f(x_0) = A_{ss,hom}\left(Erf\left[x_0 + \frac{L}{4}\right] - Erf\left[x_0 - \frac{L}{4}\right]\right) \tag{4.24}$$

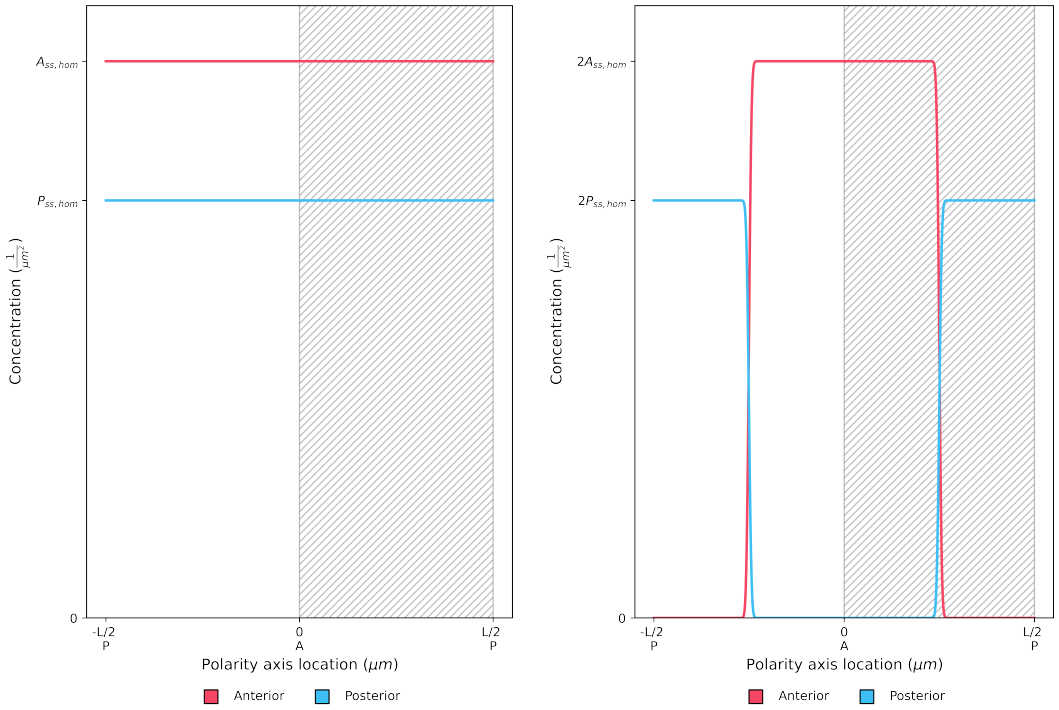
For the posterior species, the initial profile, $f(x_0)$ was set to be:

$$f(x_0) = P_{ss,hom}\left(2 - Erf\left[-x_0 + \frac{L}{4}\right] + Erf\left[-x_0 - \frac{L}{4}\right]\right) \tag{4.25}$$

across the domain

$$\frac{-L}{2} \leq x_0 \leq \frac{L}{2} \tag{4.26}$$

The functional forms of these profiles can be seen in fig. 4.8 below. Both profiles exemplify a system at steady state, where $A_{ss} > P_{ss}$.



(a) **(b)**

Figure 4.8: Initial simulation states for the single cell. Domain profiles for the **(a)** homogeneous and **(b)** polarised initial states. The homogeneous initial state is utilised when simulating establishment and maintenance phase. The polarised state represents perfect segregation by flow and is therefore used to simulate maintenance phase. Simulations are carried on a domain length L, with periodic boundary conditions. The grey shaded area represents the profile shape along the length of the anterior-posterior axis.

4.3.4.3 Diffusion of membrane bound species

The diffusion constants for PAR-2 and PAR-6 species were experimentally measured using FRAP in earlier work of Goehring et al. These diffusion constants were then utilised in

their later modelling work which forms the foundation of this research. As such, we take the order-of-magnitude approximation to those utilised in the modelling work of Goehring et al. using the PAR-6 diffusion coefficient to represent the PAR-6/CDC-42 species and the PAR-2 diffusion coefficient for the pPAR species [70]. To this end:

$$D_{A6}, D_P = 0.1\,\mu\mathrm{m}^2\mathrm{s}^{-1} \tag{4.27}$$

We approximated the slower diffusing PAR-3 species to have a characteristic diffusion constant:

$$D_{A3} = 0.01\,\mu\mathrm{m}^2\mathrm{s}^{-1} \tag{4.28}$$

This slower diffusion coefficient is consistent with the recent experimental measurements of Chang and Dickinson [118].

4.3.4.4 Diffusion of cytosolic species

In line with the assumptions of a well-mixed cytoplasm made in the modelling work of Goehring et al. we similarly approximated super-fast diffusion coefficients for cytosolic species. For all cytosolic species:

$$D_{X,c} = 2000\,\mu\mathrm{m}^2\mathrm{s}^{-1} \tag{4.29}$$

As the cytoplasm is well-mixed and therefore uniform in space at all times, there is no necessity to model the cytoplasm using an explicitly defined partial differential equation. The cytoplasm could instead be modelled as an ordinary differential equation, varying only over time. Whilst this would be more computationally efficient, we have instead chosen the partial differential approach to simplify the design integration of the cytosol into our custom numerical solver.

4.3.4.5 Membrane association rates

PAR-6 and PAR-2 association rates were taken to be the same as those previously experimentally estimated by Goehring et al. [70]. The association rate of the PAR-3 was

parametrised based on discussion with the Goehring lab (2017).

4.3.4.6 Membrane dissociation rates

Through image analysis of single-particle tracking experiments, we approximated that PAR-3 membrane lifetimes ranged up to 100 s. Species lifetimes can be related to membrane dissociation rates through:

$$\tau = \frac{1}{k_{OFF}} \tag{4.30}$$

From this, we estimate:

$$k_{OFF,A3} = 0.01\,\mathrm{s}^{-1} \tag{4.31}$$

4.3.4.7 Mutual antagonism

Reflecting the clustering of the PAR-3 species, we increased the non-linearity of the antagonism response through the stoichiometric term. Therefore:

$$\alpha, \beta = 2 \tag{4.32}$$

The range of antagonism of A by P (k_{AP}) was kept approximately constant, ranging between $0\,\mu\mathrm{m}^4\mathrm{s}^{-1}$ and $1\,\mu\mathrm{m}^4\mathrm{s}^{-1}$.The region of antagonism phase-space to be explored was then set through qualitatively matching the characteristics of the bifurcations lines in parameter space, across models and parameter instantiations. Given the range of k_{AP}, the range of k_{PA} was set by equating the lowest value explored to that of the lowest value where bi-stability occurred and the highest value as the point where the posterior-bi-stable boundary intersected with $k_{AP} = 1$.

4.3.4.8 Transition rates in the aPKC cycle

Within the 'coupled model' description of the aPKC cycle, PAR-6/aPKC binds to the membrane through association with PAR-3, before becoming a CDC-42 associated complex governed by a transition rate, k_{342}. Utilising the PAR-6 dissociation rate in the work of Goehring et al. the effective PAR-6/aPKC dissociation rate was approximated

to be $k_{OFF,EFF} = 0.005\,\mu\text{ms}^{-1}$. The CDC-42/PAR-6/aPKC complex dissociates from the membrane with rate, $k_{OFF,A42}$. Taking the harmonic mean of k_{342} and $k_{OFF,A42}$ to be equivalent to the effective dissociation rate, $k_{OFF,EFF}$, we can therefore show that:

$$\frac{2}{\frac{1}{k_{342}} + \frac{1}{k_{OFF,A42}}} = k_{OFF,EFF} = 0.005\,\mu\text{ms}^{-1} \tag{4.33}$$

which can be simplified to denote a curve from which $(k_{342}, k_{OFF,A42})$ parameter combinations can be chosen. This enabled us to tune our model system to either represent an enhanced 'flow-sensing' PAR-3 state ($k_{OFF,A42} > k_{342}$), an enhanced 'diffuse' CDC-42 state ($k_{OFF,A42} < k_{342}$) or a 'balanced' state ($k_{OFF,A42} = k_{342}$).

To parametrise an enhanced 'flow-sensing' and 'active' state in the uncoupled model, we varied ($k_{ON,A3}$, $k_{ON,A6}$). Regimes were selected based on the ratio of the amount of membrane-bound active CDC-42/PAR-6/aPKC to membrane-bound flow-sensing PAR-3.

4.3.4.9 Parameter regimes for the extended aPKC models of cell polarity

Complete tables of the parameter regimes used in numerical modelling can be found in appendix A.

4.3.5 Advection along the anterior-posterior axis

The global flow of PAR-3 clusters along the A-P axis was investigated in section 2.2.1. Importantly, an increase in PAR-3 cluster size did not result in the enhancement of sensitivity of the cluster to move with the cellular flow (see section 2.2.2). With the knowledge that cluster response is equivalent across the PAR-3 population, we therefore choose to advect PAR-3 by a global flow profile along the anterior-posterior axis. In previous models, flow fields along the A-P axis were initially sampled and implemented at each time-point within a simulation, but this was found to be ineffective in clarifying qualitative behaviour of the system and only served to be computationally expensive. Paired with our results in section 2.2.1, which show the global flow profile of PAR-3 to be consistent throughout establishment, we moved to take a simple approximation of this flow profile and implemented this single profile for the duration of the advective portion

of the simulation. This flow profile, $v(x)$ is expressed as;

$$v(x) = \frac{-8}{60}\frac{1}{1439.07}x^2 \sin\left(\frac{2\pi x}{L}\right) \tag{4.34}$$

where L is the total perimeter of the embryo. The leading constants are chosen such that the maximum flow value is consistent with that seen in experiment [98]. Importantly, this equation falls to 0 and is rotationally symmetric at the poles. This ensures that in the simulation with periodic boundary conditions, flow is always anteriorly directed.

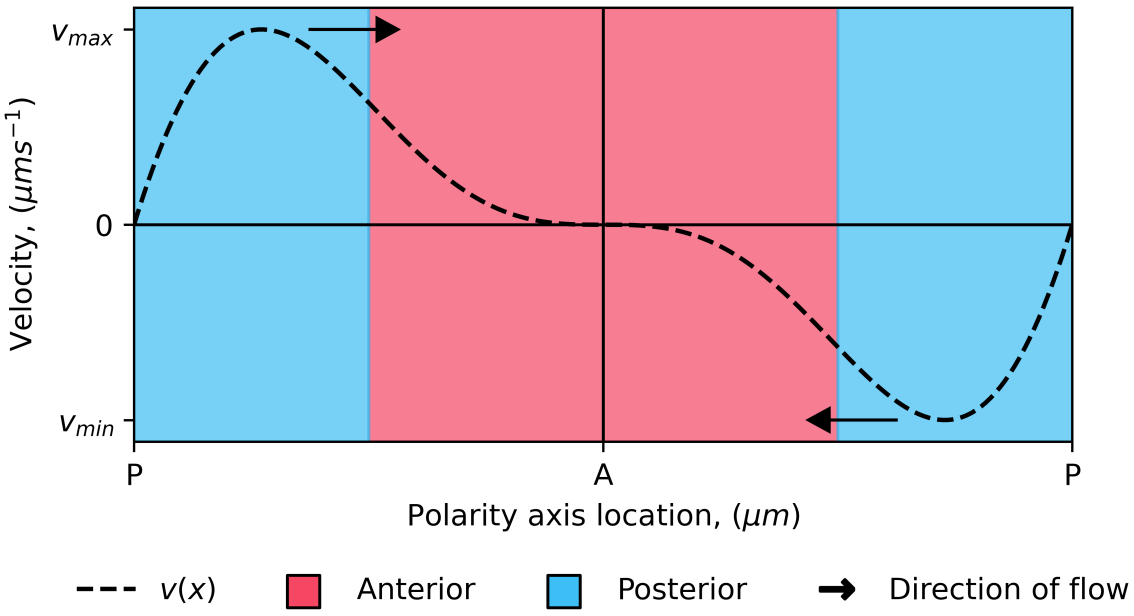


Figure 4.9: Velocity profile implemented in the reaction-advection-system. Approximated from the experimentally observed global flow profile in the *C. elegans* zygote, flow rates fall to zero at the poles and the peak flow rate is located in the posterior pole. The function is continuous across the periodic boundaries of the simulated system.

4.4 Stability and the characteristics of polarisation in the extended models of the aPKC cycle

4.4.0.1 Multi-stability in the extended polarity models

With the knowledge that multi-stability is a key design feature of PAR polarity networks, we initially explored each of the extended models at steady state to determine

the characteristics of stability in the antagonism (k_{A3P},k_{PA42}) phase-space [126]. When considering these models, the aPKC cycle transition rates were chosen that the system was 'balanced' - where at steady state, the membrane-bound anterior protein population is equal part in a PAR-3 associated 'flow-sensing' state and a 'cue-sensing' diffuse, CDC-42 associated state. As outlined in section 4.3.4.7 we choose to set $0 \leq k_{A3P} \leq 1\mu m^4 s^{-1}$, instead varying k_{AP42} such that the lower bound denotes the point of emergence of the bi-stable region and the upper bound the value when the posterior-bi-stable boundary intersects $k_{A3P} = 1\mu m^4 s^{-1}$. We performed linear stability analysis on both the coupled and uncoupled models to ascertain if the models were multi-stable in character and if so, under what conditions multi-stability could be achieved. The shape of bifurcations in phase-space are influenced by the stoichiometry of the antagonistic reactions. As a result, the characteristic regions of phase-space are coherent across the coupled and uncoupled model - see fig. 4.10.

Both the coupled and uncoupled model require a stronger imbalance in the $k_{A3P} : k_{PA42}$ activity ratio than the 'simple' 2-par model (see fig. 4.3d) to support bi-stability. In the case of the coupled model (fig. 4.10), this imbalance is strongest, requiring a 10 fold increase in the activity of the anterior active species to support bi-stability. In the uncoupled model, the constraints on activity imbalance between the anterior and posterior active species are relaxed. As a result, though compressed in comparison to the posterior monostable region, the uncoupled model can support an anterior monostable region. Strikingly, the coupled model is hyper-sensitive to the activity of the posterior species and is only able to produce an infinitesimally small anterior mono-stable region. This illustrates a deviation in the characteristic stability of the coupled model as compared to both the 'simple' and uncoupled models.

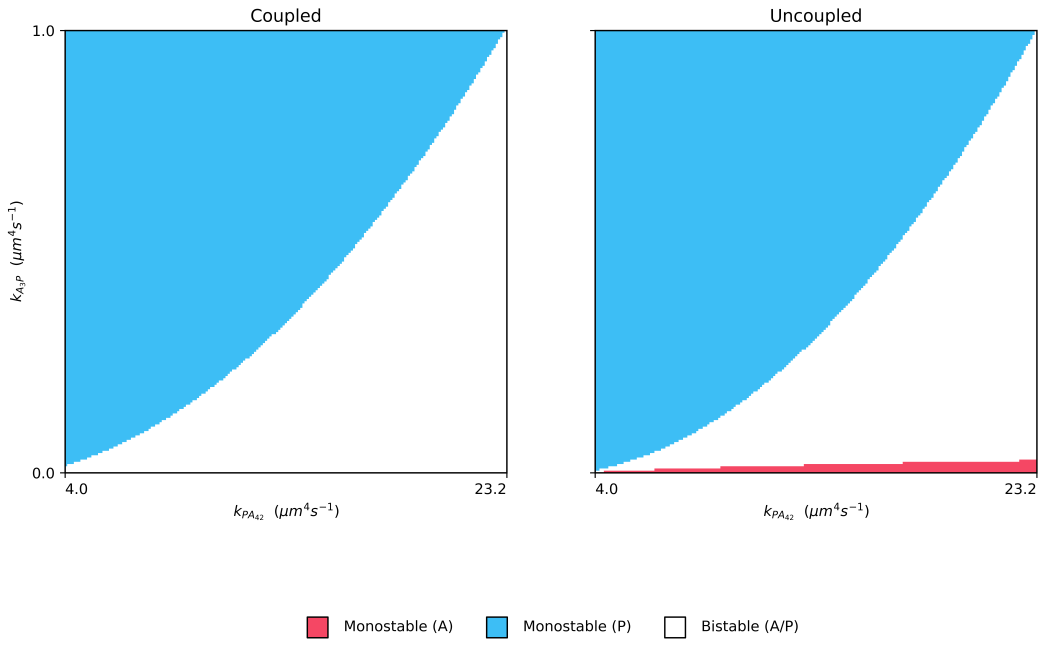


Figure 4.10: The extended aPKC models are bi-stable in nature and are therefore able to polarise. Regions of antagonism phase-space that permit mono-stable and multi-stable steady states for the **(A)** coupled and **(B)** uncoupled model. Both models produce a posterior mono-stable (blue) and a multi-stable (hatched) state. Only the uncoupled model appears to be able to produce an anterior mono-stable state (red). Governed by the stoichiometry of the mutually antagonistic species, the character of the antagonism phase-space is consistent across models.

4.4.0.2 Polarisation in the extended polarity models

We next asked whether the extended models of cell polarity could both establish and maintain domains. From our stability analysis, it is expected that anterior mono-stable regions will give rise to anterior homogeneous domains and for posterior mono-stable regions to give rise to posterior homogeneous solutions. In the multi-stable region, should the perturbation by flows be sufficient, it is expected that a polarised state will exist.

Initially, we explored antagonism phase-space uniformly, carrying out reaction-advection-diffusion simulations parametrised through a grid-search of parameter sets. Simulations were initialised from an artificially polarised state to isolate maintenance phase and the ability of the model to stably retain polarised domains. Additionally, an initially homogeneous state replicated the establishment (and subsequent maintenance) of domains from the anterior dominant state that is observed in vivo. Similarly to that

observed *in-vivo*, advection by cortical flows was simulated between $t = 120\,\mathrm{s}$ and $t = 660\,\mathrm{s}$ [70]. With the knowledge that a key indicator of successful polarisation is domains that are approximately equal in size, we then ranked the final outcome of polarisation based on the position of domain intersection section 4.6.2.1. The 'best-fit' outcomes were selected to initially assess whether the coupled and uncoupled models of cell polarity could polarise successfully.

With reference to fig. 4.11, it can be seen that both extended polarisation models are able to establish and maintain domains. Importantly, the final state in fig. 4.11a shows that the coupled model is less able to respond to the advective trigger, a characteristic that is demonstrated by the shallower anterior profile during establishment phase. As a result of the system being less able to clear anterior protein from the posterior pole during polarity establishment, the posterior domain forms more slowly. Though the posterior protein is able to bind to the membrane from the clearance of the posterior pole, the delay in domain formation means the system does not develop the hallmark over-expansion of the posterior domain. Additionally, the anterior domain concentration remains reduced as compared to the posterior domain. Comparatively, the uncoupled model is successful in clearance of the anterior protein from the posterior domain at the onset of flows - see fig. 4.11c. This enables the over-expansion of the posterior domain, before retraction back to the embryo mid-line. Unlike the coupled model, the final domain profile reached by the uncoupled model exhibits balanced domain concentrations with a posterior concentration approximately twice that of the anterior domain - a characteristic that is observed in vivo [70].

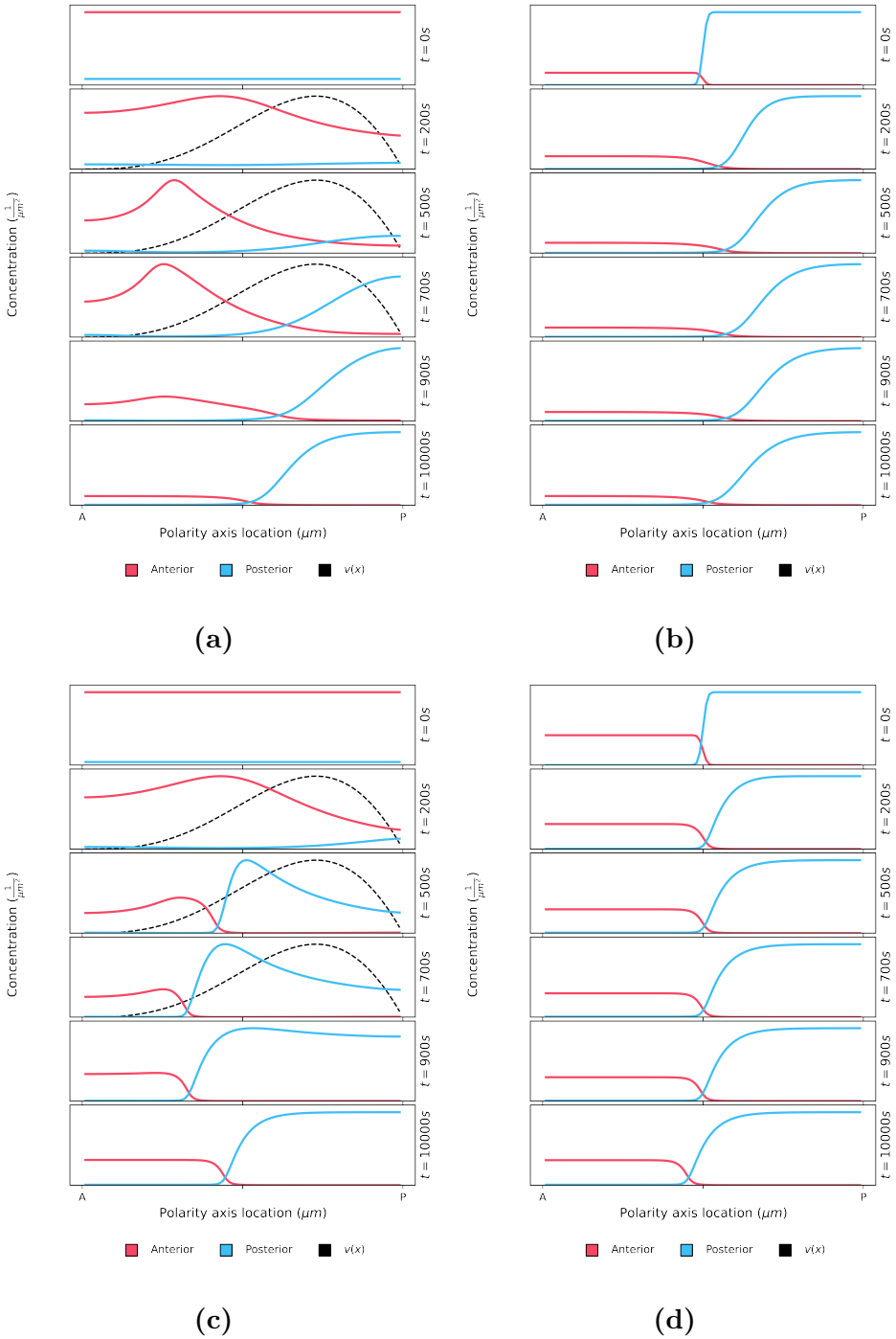


Figure 4.11: The extended models of cell polarity can respond to a polarising cue to establish and maintain polarity. Time-series of polarisation for exemplary parameterisations of the **Top - (a),(b)** coupled and **Bottom - (c),(d)** uncoupled model. Shown are total concentrations of the opposing PAR groups, anterior PAR (red) and posterior PAR (blue). **Left - (a), (c)** Simulations initialised with the anterior dominant homogeneous state represent establishment and maintenance phase *in-vivo*. A global velocity profile is implemented during establishment phase (black dashed line) which acts to transport the flow-sensing anterior protein. **Right - (b), (d)** Simulations initialised with an artificially polarised state represent proxy maintenance phase *in-vivo*. Indicated in the bottom panel is the long-term behaviour of the system. For each model, this same state is attained when initialised with either an artificially polarised or anterior homogeneous state.

4.4.0.3 The effect of relative antagonism on relative domain sizes

After verification that the extended models of cell polarity could indeed form a biologically viable domain, we next considered how the characteristics of the final domain state are altered in antagonism phase-space. Simulations were initialised from the anterior dominant homogeneous state and run for $t = 10000\,\mathrm{s}$ and therefore represent the long term behaviour of the system following establishment of polarity in response to flows. Again, flows were implemented between $t = 120\,\mathrm{s}$ and $t = 660\,\mathrm{s}$. Measured domain profiles *in-vivo* reveal that the concentration of the anterior domain is approximately half that of the posterior domain [71]. Therefore, we score the simulation outcomes based on the relative length and relative concentrations of the domains - see section 4.6.2.1 for details.

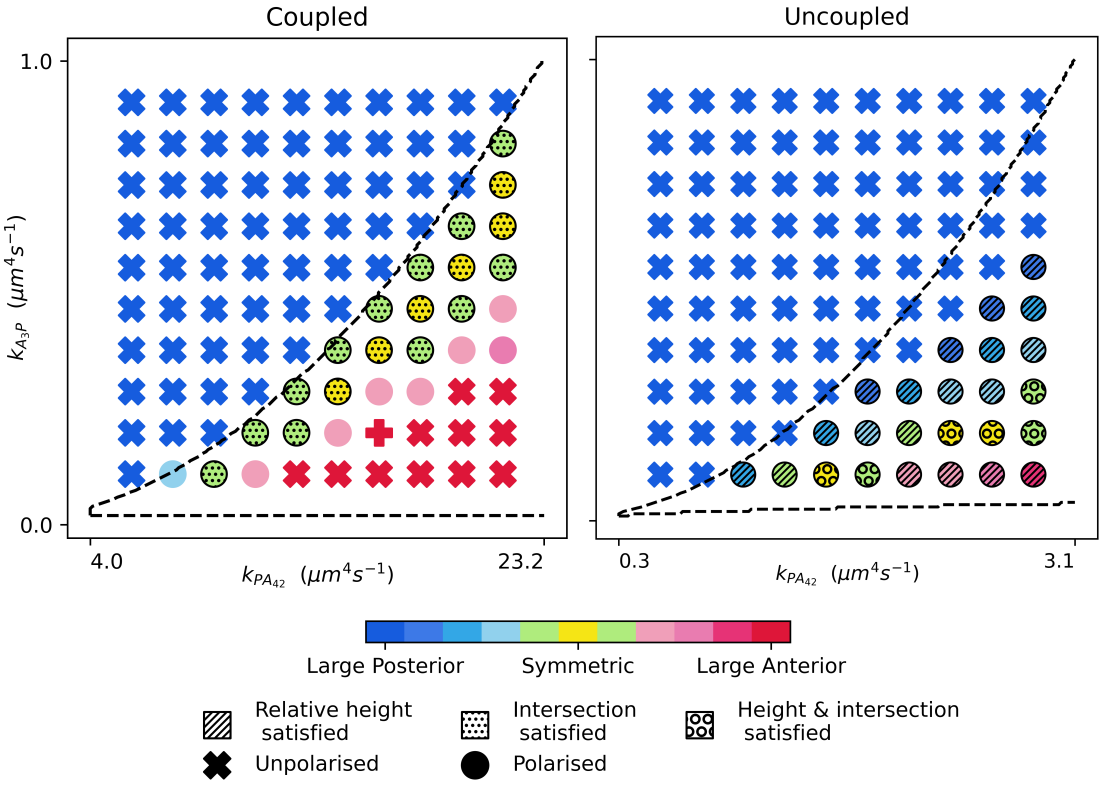


Figure 4.12: Poised at the edge of bi-stability, polarisation in the coupled model is sensitive to perturbation of relative antagonism. Simulation outcomes for extended models in a balanced state for varying relative antagonism parameterisations. Simulations were initialised from an anterior dominated homogeneous state and therefore represent long term solutions following establishment phase. Crosses indicate homogeneous solutions. Circles indicate polarised solutions. Dots indicate polarised solutions with approximately equal domain lengths. Stripes indicate polarised solutions with biologically viable relative domain concentrations. Spots indicate polarised solutions that fulfil both relative domain length and concentration requirements. Colouring indicates the extent to which a domain is dominant with yellow indicating equally sized domains.

It can be seen from fig. 4.12, that the response of each of the extended models to perturbation of relative antagonism is distinct. Interestingly, though the linear stability analysis of the coupled model in antagonism phase-space predicts an infinitesimally small anterior mono-stable region, much of the bi-stable region results in an anterior unpolarised state. In the coupled model at low k_{A3P} and high k_{PA42}, the posterior is unable to bind to the membrane and form domains. As discussed in section 4.4.0.2, this is due to an insensitivity of the anterior species to flow and thus an improper clearance of the posterior domain. Polarity in the *C. elegans* zygote relies on both a cortical cue (flows)

and a posterior guiding cue (posterior antagonism) [71]. When k_{A3P} is low, pPAR is unable to clear the posterior pole and the posterior guiding cue is absent - the 'barrier to polarisation' is not overcome and the cell falls back to an anteriorly homogeneous state.

Domains of approximately equal size can only be produced when the activity of the posterior is maximised as compared to the activity of the anterior active species, indicated in the proximity of this region to the posterior-bi-stable boundary. This proximity indicates that the region of successful polarisation lies in a delicate balance as if posterior activity exceeds that needed to polarise, the system readily moves to a polarised state characterised by a vastly over-expanded posterior domain. Across all domain forming sets, the coupled model is not able to sufficiently balance domain concentrations, with the posterior protein being strongly over-expressed.

Notably, within the domain forming region in the uncoupled model, all parameter instantiations are able to produce domains that are balanced in concentration (see fig. 4.12). Unlike the coupled model, this indicates that perturbation of the activity of the antagonistic species mainly to alter the position of the domain boundary. As opposed to the coupled model, the region where equal-sized domains are formed lies centrally in the bi-stable region. This positioning in phase-space indicates little bias towards the activity of either active species in the production of biologically viable domains. As a result, it is to be expected that the uncoupled model will be less sensitive to perturbation of the relative antagonism of the active species. This reduced sensitivity is apparent in the expansion of the region of phase-space that can maintain domains of any size as compared to the coupled model where polarity is readily lost. Together, these results indicate that the uncoupled model is likely a more suitable candidate for controllable, robust polarisation.

4.4.1 The effect of the relative proportion of active and flow-sensing anterior protein on polarisation of the extended polarity models

We have previously outlined the relationship between the activity of the extended models' active species and the qualitative effect this has on the final state reached in the polarisation process. In a system state where the initial proportion of anterior protein in a flow-sensing (PAR-6/PAR-3) state is equal to that of an active (PAR-6/CDC-42) state we found that the coupled model is sensitive to perturbation of relative activity as a result of its reliance on posterior activity to compensate for an insufficient response to polarising flows. This is reminiscent of the redundant pathway to polarity observed by Goehring et al. [70]. Comparatively, the uncoupled model sufficiently responded to flows and so posterior antagonism remained less critical to successful domain establishment.

An advantage of the proposed aPKC cycle is the separation of PAR-6/aPKC into functionally distinct complexes, endowing the system with a control mechanism by which to favour advantageous functional complexes at different times in the cell cycle. This would enable the system to shift between a cue-deriving state where PAR-6/aPKC association to PAR-3 clusters is upregulated during establishment phase. Following this, up-regulation of PAR-6/aPKC to a CDC-42 associated active, diffuse state would enable the system to efficiently maintain domains. We next moved to assess whether the proposed biochemical networks could fulfil such functionality. To this end, we investigated how the proposed model networks are affected when considering the each model system in a biased anterior configuration, favouring either active or flow-sensing protein.

4.4.1.1 Polarisation in the extended models when favouring a 'cue-sensing' or 'active' state

We again applied linear stability analysis to assess how favouring one functional protein over another may affect the region of antagonism phase-space that can give rise to bi-stability. As can be seen in fig. 4.13, moving towards an active state increases the size of the anterior mono-stable region in both the coupled and uncoupled model. This

effect is more pronounced in the coupled model, where an effective reduction in PAR-3/PAR-6/aPKC lifetime both reduces exposure to antagonism by the posterior species and increases the antagonistic ability of the anterior population. This effect is reversed when the system is configured to favour the flow-sensing state, requiring around 100-fold increase in activity of the antagonistic anterior species to produce bi-stable states. Unlike the coupled model, the uncoupled phase-space remains characteristically similar across all flow-sensing, balanced and active states. Importantly, the uncoupled model is multi-stable in character when the activity of the antagonistic anterior species remains comparable to that of the posterior active species. Coherence in the characterisation of stability in antagonism phase-space across system configurations indicates that the region of successful polarisation will be stable in the uncoupled model.

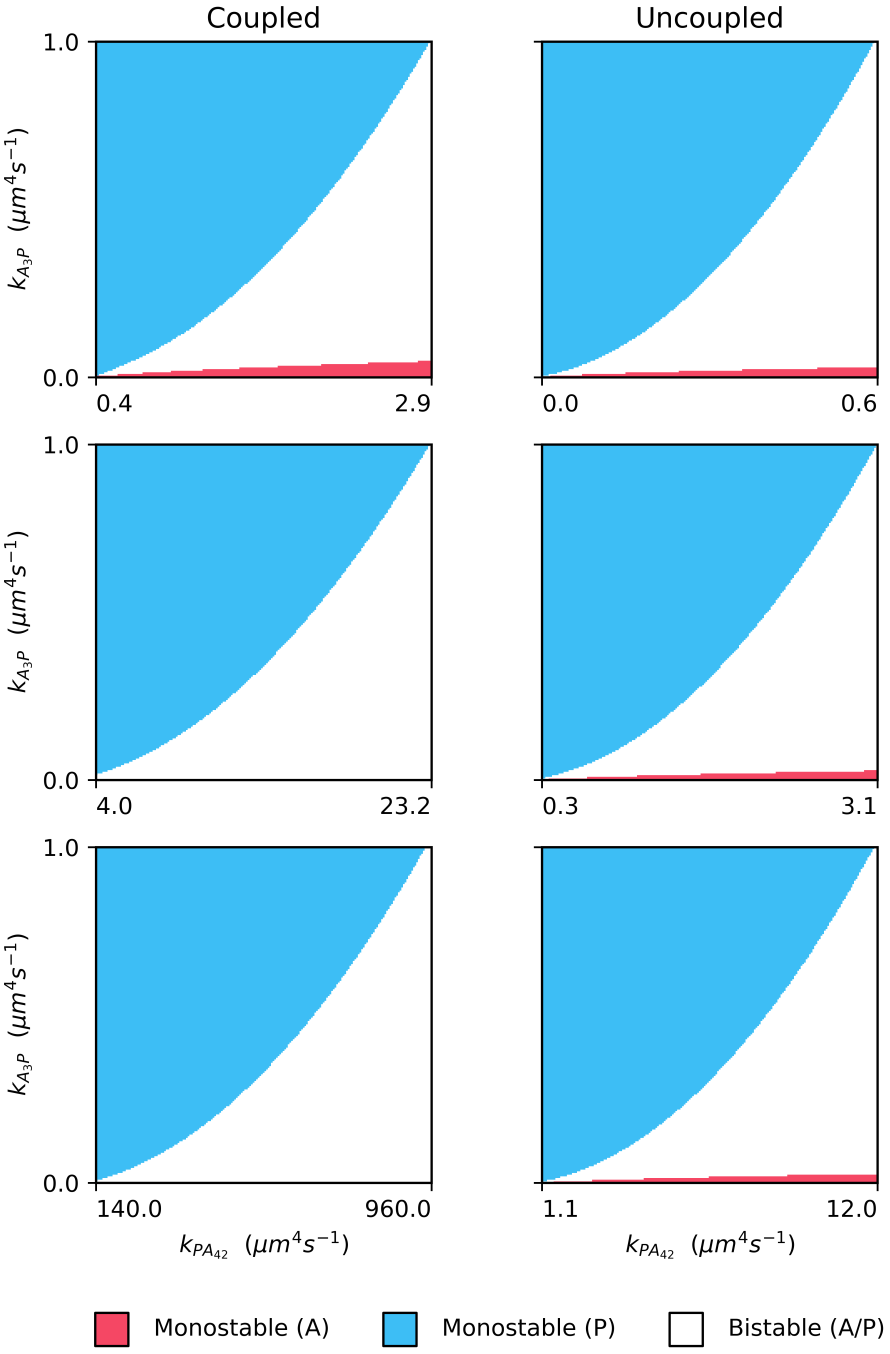


Figure 4.13: The coupled model requires an unviable reconfiguration of relative antagonism to achieve bi-stability when switching between an active and flow-sensing anterior membrane system configuration. bi-stability for the extended aPKC models in a **Top** Active **(Middle)** Balanced and **(Bottom)** Flow-sensing, inactive system configurations. The characterisation of bi-stability in antagonism phase-space remains consistent across all system configurations of the uncoupled model. The coupled model remains hyper-sensitive to antagonism - when in a flow-sensing configuration (bottom, left) bi-stability is only achievable when aPAR activity is strong.

Next, we moved to characterise the domain states produced by each model in the active, balanced and flow-sensing states. As per our ranking system outlined in section 4.6.2.1 we again show the 'best-fit' simulations for the coupled and uncoupled models in fig. 4.14 and fig. 4.15 respectively. Both extended models are able to produce a domain state in both the 'active' and 'flow-sensing' biased population initialisations. Similarly to the unfavoured anterior configuration in section 4.4.0.2, the coupled model remains unable to produce biologically viable domain concentrations in both the active and flow-sensing system configurations.

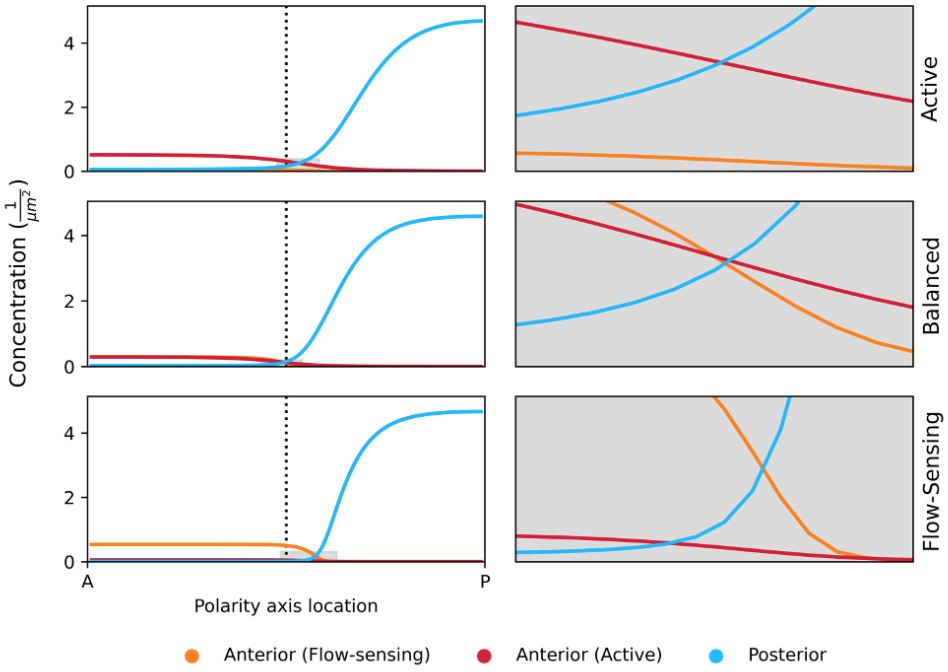


Figure 4.14: The coupled model cannot produce biologically viable domains when favouring any functional configuration of the anterior proteins. Simulation outcomes for the 'best-fit' parameterisations of the coupled model in the 'active', 'balanced' and 'flow-sensing' system configuration. The coupled model cannot balance domain concentrations in any configuration. Shown are the concentration profiles for posterior PAR (blue), CDC-42/PAR-6/aPKC (red) and PAR-3/PAR-6/aPKC (orange) complexes. The right hand panel shows a magnified view of the domain intersection (highlighted grey in the corresponding left-hand panel).

Perhaps unexpectedly, the gradient of the domain intersection is most shallow when the system lies in the active state, and steepest when in the flow-sensing state. This effect

arises as a result of the decoupling of the antagonistic interactions between a fast-diffusing antagonistic protein and a slow-diffusing antagonised protein in the aPKC cycle of the coupled model. Here, the available membrane-bound pool of slow-diffusing PAR-3/PAR-6/aPKC is low whilst the pool of active CDC-42/PAR-6/aPKC is high: the model benefits from neither a large slow-diffusing membrane pool nor large pools of mutually antagonistic protein - either of which would result in a steep domain boundary [115]. The effect of diffusive rate on boundary steepness can be seen in the balanced coupled model, where at the point of intersection, the fast-diffusing CDC-42/PAR-6/aPKC species (red) forms a shallower boundary than the slow-diffusing PAR-3/PAR-6/aPKC (orange). In the active state, the majority of the membrane-bound anterior protein is in a fast-diffusing antagonistic state which readily invades the posterior boundary, effectively spreading to create a shallower domain boundary. Conversely, in the flow-sensing state the significant pool of slow-diffusing PAR-3/PAR-6/aPKC protein creates a steep anterior boundary. Here, the lifetime of the active CDC-42/PAR-6/aPKC state is short and so this active protein remains spatially coupled to the PAR-3/PAR-6/aPKC species. As a result, the active anterior protein is unable to invade the posterior domain beyond the extent of the PAR-3/PAR-6/aPKC domain. To compensate for the low concentration of active protein, the antagonistic CDC-42/PAR-6/aPKC complex requires a significantly increased activity in order to maintain a domain state (see fig. 4.13) and as a result of this requirement, the posterior profile is readily attenuated by the anterior active protein. Coupled with the relatively low dissociation rate of the posterior PAR, this attenuation leads to a similarly steep posterior domain. The total anterior protein concentration remains consistent for all system configurations and is a result of the cyclic motif underpinning the anterior reactions in the coupled network design.

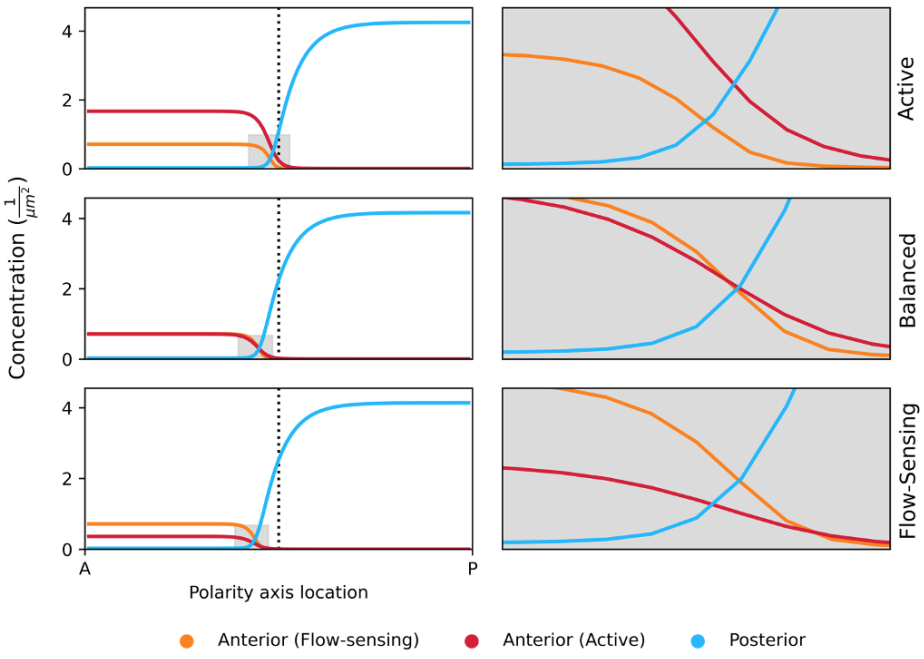


Figure 4.15: The uncoupled model can produce biologically viable domains when favouring any functional configuration of the anterior proteins. Simulation outcomes for the 'best-fit' parameterisations of the coupled model in the 'active', 'balanced' and 'flow-sensing' system configuration. Shown are the concentration profiles for posterior PAR (blue), CDC-42/PAR-6/aPKC (red) and PAR-3 (orange) complexes. The right hand panel shows a magnified view of the domain intersection highlight grey in the corresponding left-hand panel.

Unlike the coupled model, the uncoupled model produces domain profiles that are characteristically similar across the flow-sensing, balanced and active system states (see fig. 4.15. This is a result of the relaxation of the constraint imposed by the cyclic motif and mass-conservation in the coupled model. In the uncoupled model, PAR-6/aPKC can bind to the membrane independently of PAR-3 and therefore production of the active CDC-42/PAR-6/aPKC complex does not rely on the dissociation of PAR-6/aPKC from PAR-3 and the conversion of membrane-bound PAR-3/PAR-6/aPKC. Therefore, the PAR-3 profile concentration remains constant across all system states, acting to provide spatial information to the anterior system through establishment. As the flow-sensing protein, PAR-3 defines the patterning template for polarisation and therefore these system states all possess similarly shaped domains. When in the active state, the upregulated pool of active protein is able to effectively antagonise the posterior protein through expansion

beyond the PAR-3 boundary. Differentially, when in the flow-sensing state the active protein has a reduced membrane lifetime and so is again constrained by the PAR-3 domain. In this way, alteration of the proportion of active CDC-42/PAR-6/aPKC on the membrane acts to shift the anterior/posterior boundary which leads to an over-enlarged posterior domain in the flow-sensing state. This shift of domain boundary in response to over/under-expression of active material is an effect observed *in-vivo* [62].

4.4.1.2 The effect of relative antagonism on the extended models of cell polarity favouring a 'cue-sensing' or 'active' state

Having explored the form of polarised states that are produced by both the coupled and uncoupled model, we again returned to investigate how the domain profiles were affected by relative antagonism of the active species. Importantly, in this view, the sensitivity of the coupled model to antagonism is amplified.

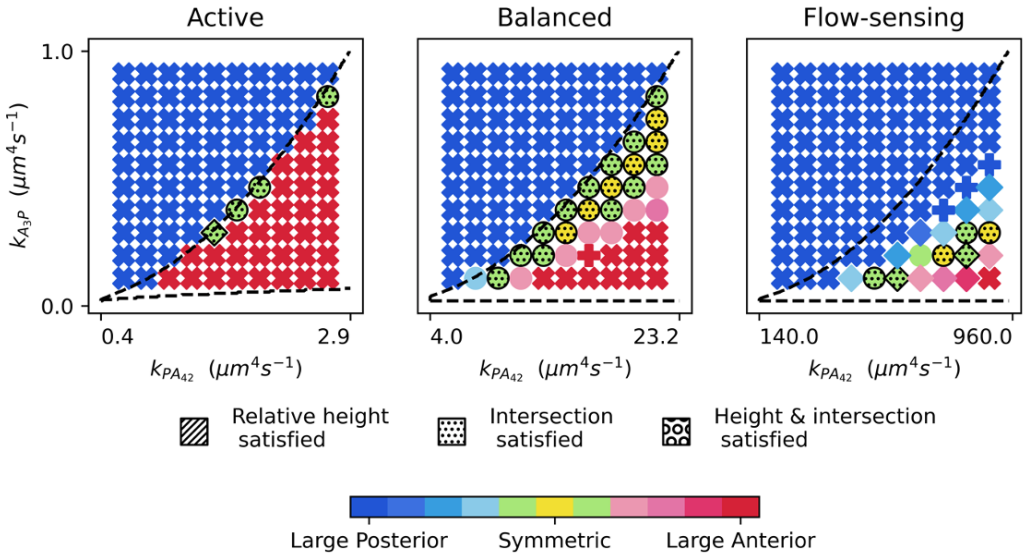


Figure 4.16: The hyper-sensitivity of the coupled model to relative antagonism is amplified when favouring both a 'cue-sensing' and 'active' anterior state. Simulation outcomes for the coupled model in an 'active', 'balanced' and 'flow-sensing' system configurations for varying relative antagonism parameterisations. Simulations were initialised from an anterior dominated homogeneous state and therefore represent long term solutions following establishment phase.

With reference to fig. 4.16, it can be seen that a shift between the active and flow-sensing state imposes opposing conditions for the antagonistic interaction of the active

species. When in the active state the large pool of weakly active protein pushes the system to a hyper-sensitive state whereby domains can only form in the region of phase-space at the edge of the bi-stable-posterior boundary. In this state, a short PAR-3/PAR-6/aPKC lifetime results is a reduced pool of flow-sensing material and a reduced response to symmetry-breaking flows. Hence polarisation is strongly reliant on the PAR-2 cue and clearance of the posterior through antagonism. Here, the system is unable to produce equally-sized domains: to enlarge the posterior domain would require a decrease in the activity of the anterior species. However, the coupled model is hyper-sensitive to antagonism and so such a decrease would instead result in the posterior domain expansion and resultant loss of an anterior domain. Similarly, any amplification or reduction of the ability of the posterior protein to antagonise the anterior protein forces the system to an anterior mono-stable state.

Conversely, in the flow-sensing state there is a reduced pool of antagonistic protein of enhanced activity. In this state, the overall antagonistic ability of the anterior protein is balanced through this upregulated activity. As a result of this balance, the constraints on the system relax and the region of phase-space where equal sized domains are produced shifts back towards the centre of the bi-stable region. However, this relaxation comes at the potential cost of unviable rates of activity for the active CDC-42/PAR-6/aPKC complex.

The observed hyper-sensitive behaviour of the coupled model when favouring either a 'cue-sensing' or 'active' state is overcome by the decoupling of CDC-42/PAR-6/aPKC from PAR-3 in the uncoupled model. With reference to fig. 4.16, when switching between functional states the polarisation outcomes remain consistent in phase-space. In the flow-sensing state, the system in less able to balance relative domain heights for high $k_{PA_{42}} : k_{A_3P}$, likely due to the shift in activity of the reduced anterior 'active' pool needed to support polarisation.

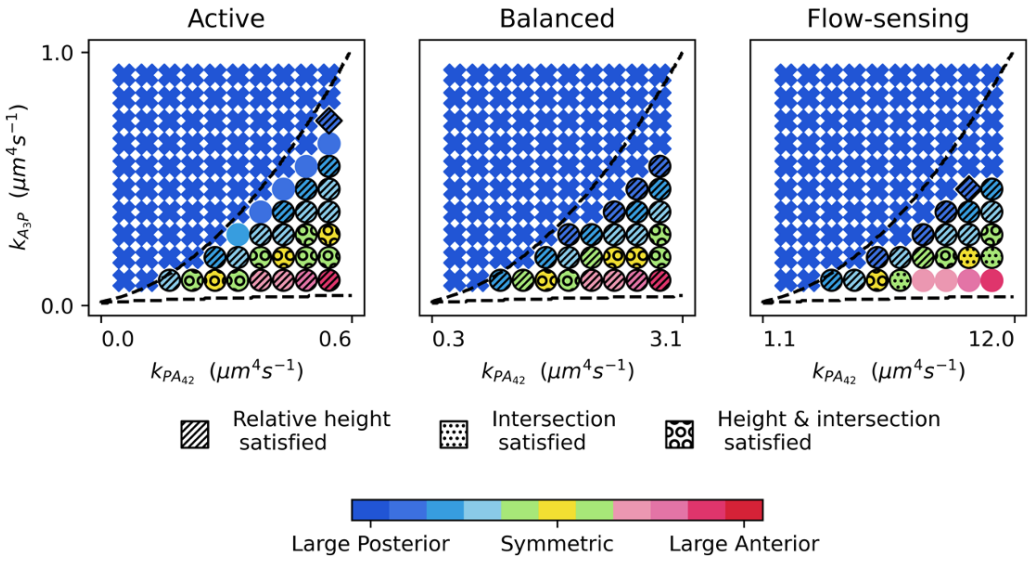


Figure 4.17: Polarisation outcomes remain stable when switching between a 'cue-sensing' and 'active' state in the uncoupled model. Simulation outcomes for the uncoupled model in an 'active', 'balanced' and 'flow-sensing' system configuration for varying relative antagonism parameterisations. Simulations were initialised from an anterior dominated homogeneous state and therefore represent long term solutions following establishment phase.

4.4.2 The effect of the relative diffusivity of active protein on polarisation of the extended polarity models

In section 4.4, we explored the extended aPKC models and the effect of alteration of system characteristics on the models' ability to polarise. Importantly, we highlighted the constraining effect that the imposition of mass-conservation has on the ability of the coupled model to polarise. Crucially, the diffusivity of the active protein dictates the relative gradient of the domain profile and as a result contributes to domain stability [116]. We therefore looked to quantify the effect of relative diffusivity in the context of relative antagonism on the position of the domain boundary. As a comparison, we calculated the position of domain equality predicted from the reaction nullclines, as in section 4.6.1.3. This allows us to isolate the contribution of species dynamics from the contribution of the reactions.

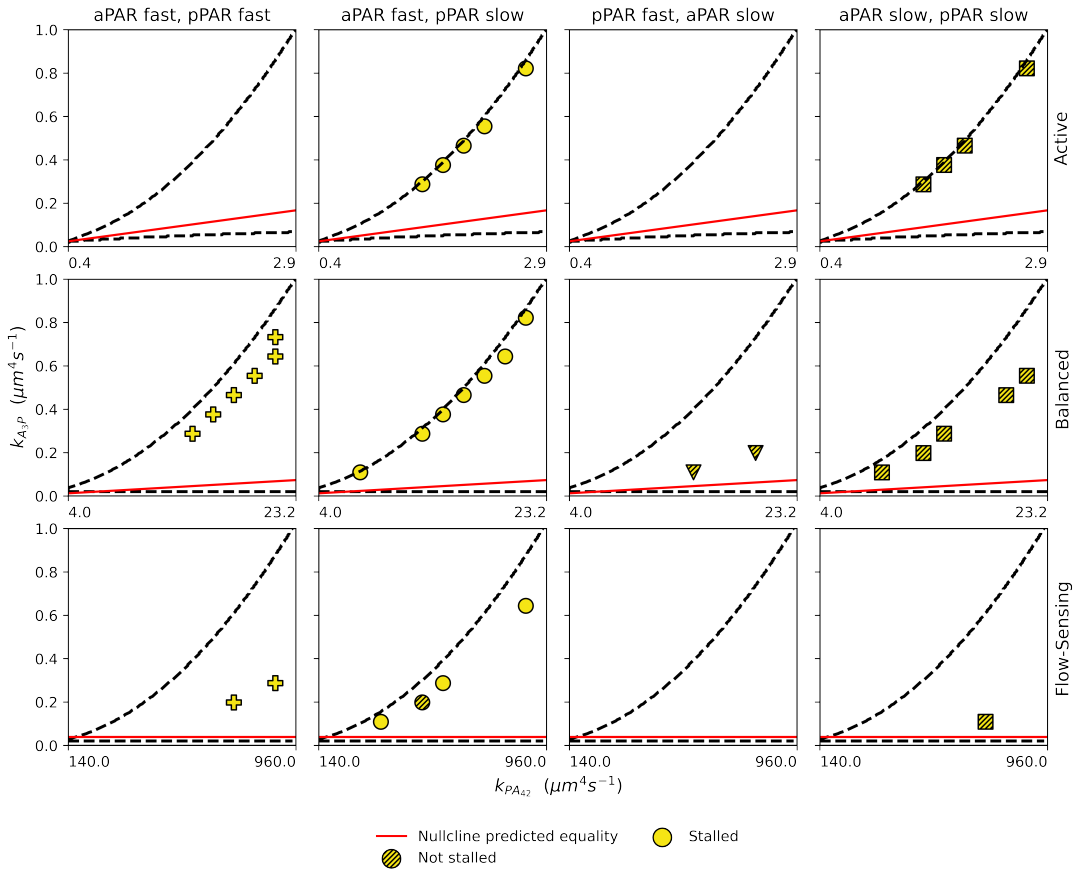


Figure 4.18: In the coupled model, the anterior system configuration has a strong effect on the requirements for polarisation unless the diffusivity of *pPAR* is slowed. The location in antagonism phase-space of parameterisations of the coupled model that result in approximately equal domain formation. Simulations were initialised from an anterior dominated homogeneous state and therefore represent long term solutions following establishment phase.

Nullcline analysis predicted that in the absence of protein dynamics the position of domain equality in the coupled model would reside close to the bi-stable/anterior monostable boundary, with proximity to the boundary increasing as the system moved to a flow-sensing state - see fig. 4.18. However, when simulating the polarity establishment process, the region of domain equality did not align with that predicted by nullcline analysis. In the active state, the coupled model only produced equally sized domains when the diffusivity of the posterior species was slowed and the position of domain equality was conversely located close to the bi-stable/posterior monostable boundary. For each diffusive regime, the necessity to maximise the antagonistic ability of the posterior species is relaxed as the system moves from an active to a flow-sensing state - indicated through the movement of the region of domain equality away from the posterior-monostable boundary.

In the active state, equal domains form only when the diffusivity of the active posterior species is slowed in comparison to the active anterior state. Here, the anterior protein is poorly segregated during establishment and so polarisation relies on increased activity of the posterior protein in order to clear the domain of anterior protein. Increasing the diffusivity effectively increases the ability of posterior protein to invade the anterior boundary which in this regime leads to destabilisation of the system. Conversely, in the flow-sensing state, decreasing the relative diffusivity of the posterior species leads to the relaxation of the requirement of maximising posterior activity. When the diffusivity of both active species are slowed, the system relaxes to steady state more slowly than in the fast-diffusing regime as each species is less able to invade the opposing domain. Notably, in the active state the final domain profile retains a larger anterior domain and is devoid of the characteristic over-expansion of the posterior profile. This reflects the fact that the slow-diffusing posterior is now less able to clear the pole of residual anterior protein that resulted because of improper segregation by flows.

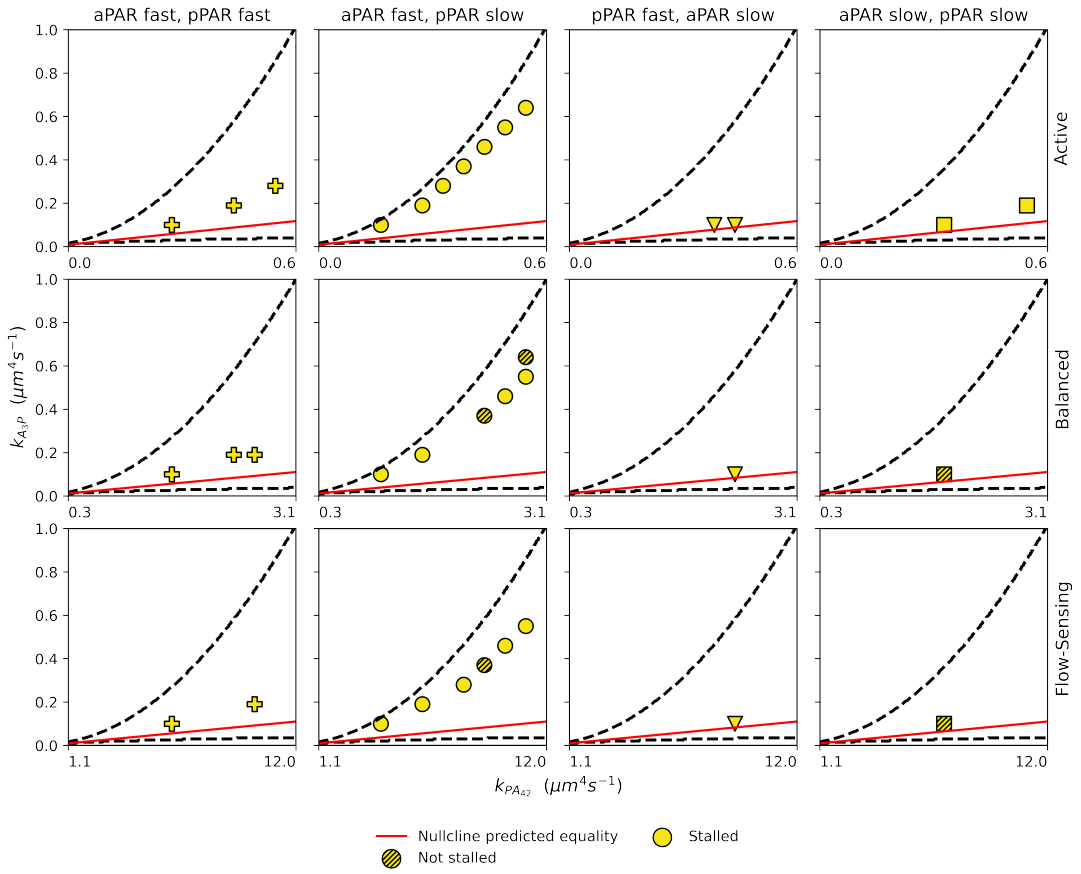


Figure 4.19: In the uncoupled model, the dynamic regime dictates the outcomes of polarisation and not the anterior system configuration. Destabilisation of polarisation occurs when $D_{A42} > D_P$ is slowed. The location in antagonism phase-space of parameterisations of the uncoupled model that result in approximately equal domain formation. Simulations were initialised from an anterior dominated homogeneous state and therefore represent long term solutions following establishment phase.

Similarly to the coupled model, nuclline analysis of the uncoupled model again predicted domain equality close to the bi-stable/anterior-monostable boundary - see fig. 4.19. Differentially, for a given diffusive regime, the uncoupled model is able to maintain a consistent region of domain equality across active, flow-sensing and balanced system states. Similarly to the coupled model, reducing the diffusivity of only the active posterior species requires the relative activity of the posterior species to increase in order to form biologically viable domains. This effect is most prominent when in the active state, where the levels of membrane bound flow-sensing anterior protein is reduced and as such, segregation by flows is less effective during establishment phase. When the diffusivity of the anterior active protein is slowed, the uncoupled model is able to achieve domain equal-

ity in a region of antagonism phase-space close to that predicated by nullcline analysis. Taken together, these results indicate that the uncoupled model represents a more stable network design for polarisation.

4.4.3 The effect of network topology in a mass-conserved model of the aPKC cyle

We next looked to explore why the uncoupled model appears more stable to perturbation than the coupled model. Specifically, we examined the limitations of the coupled model induced by the cyclic topology of the aPKC cycle. To do this, we simulated a symmetric coupled model as in fig. 4.20 - for more detailed model information see appendix A. The model was initialised to be symmetric in design of the interaction network and both the dynamic and reactive parameters. As such, the model describes a circuit where both anterior and posterior species are recruited to the membrane solely through a clustering, flow-sensing species. When bound to the membrane, the anterior/posterior protein dissociates and forms a complex that is diffusive and antagonistic to the opposite flow-sensing species. To isolate the effect of antagonism and diffusion on the success of polarisation, we parametrise protein concentrations to be correspondingly equal section 4.3.4.1.

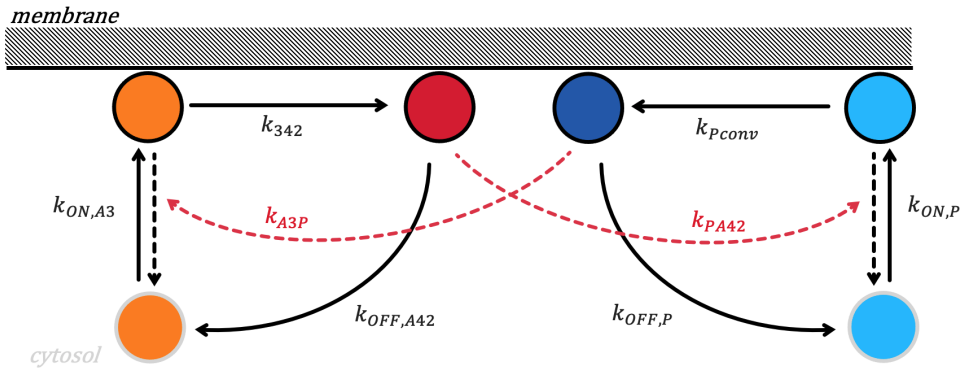


Figure 4.20: Schematic of the 'symmetric' PAR model. The PAR-6/aPKC binds to the membrane via the scaffold protein PAR-3 to form the flow-sensing, inactive, anterior complex PAR-3/PAR-6/aPKC (orange). With some characteristic rate, k_{342}, PAR-6/aPKC dissociates from PAR-3 and forms the diffusive, active complex (CDC-42/PAR-6/aPKC) (red) before dissociating back to the cytosol. In this active state, CDC-42/PAR-6/aPKC is able to antagonise the membrane-bound inactive, flow-sensing posterior species (light blue). In this symmetric model, the flow-sensing posterior PAR forms an active complex (dark blue) with characteristic rate k_{P342}. This species is able to antagonise the (PAR-3/PAR-6/aPKC) complex before dissociating from the membrane with a characteristic rate. When bound to the membrane, all proteins freely diffuse. Only PAR-3/PAR-6/aPKC and the inactive pPAR are sensitive to flows during establishment phase.

Initially, we considered whether the symmetric model was able to maintain an initially polarised state. With reference to fig. 4.21, nullcline analysis of this symmetric model predicted domain equality along the bisection of antagonism phase-space. As expected, in regimes where the diffusivity of the active species were equal the region of domain equality coexisted with that predicted by nullcline analysis. Around this nullcline, the width of the region that can maintain domains is dictated by both the diffusivity of the active species and the proportion of the conserved system in the active or flow-sensing state. In the former case, when the diffusion is fast the system is unable to stabilise domains when there is an imbalance in antagonism as both species readily invade the opposite domain. Contrarily, when diffusion is slowed the domain boundary is sharper and over the time period of polarisation the system can stabilise domain profiles

of varying asymmetry. An imbalance in diffusivity of active species requires the system to compensate by way of altering the relative antagonism of the species in order to produce domains. When in a flow-sensing state, the degree to which the system needs to compensate is reduced, with the region of domain equality positioned more closely to that predicted by nullcline analysis. When moving to an active state, the system becomes more sensitive - when the relative diffusivity of the anterior active species is high the increased relative activity of the posterior species is amplified which manifests in a shift in polarising region towards the posterior-monostable boundary. These effects are reciprocated in the regime where the posterior active species diffuses more quickly than the anterior species. Notably, in all but the slow-diffusing regime, moving to an active state causes a constriction of the domain-forming region.

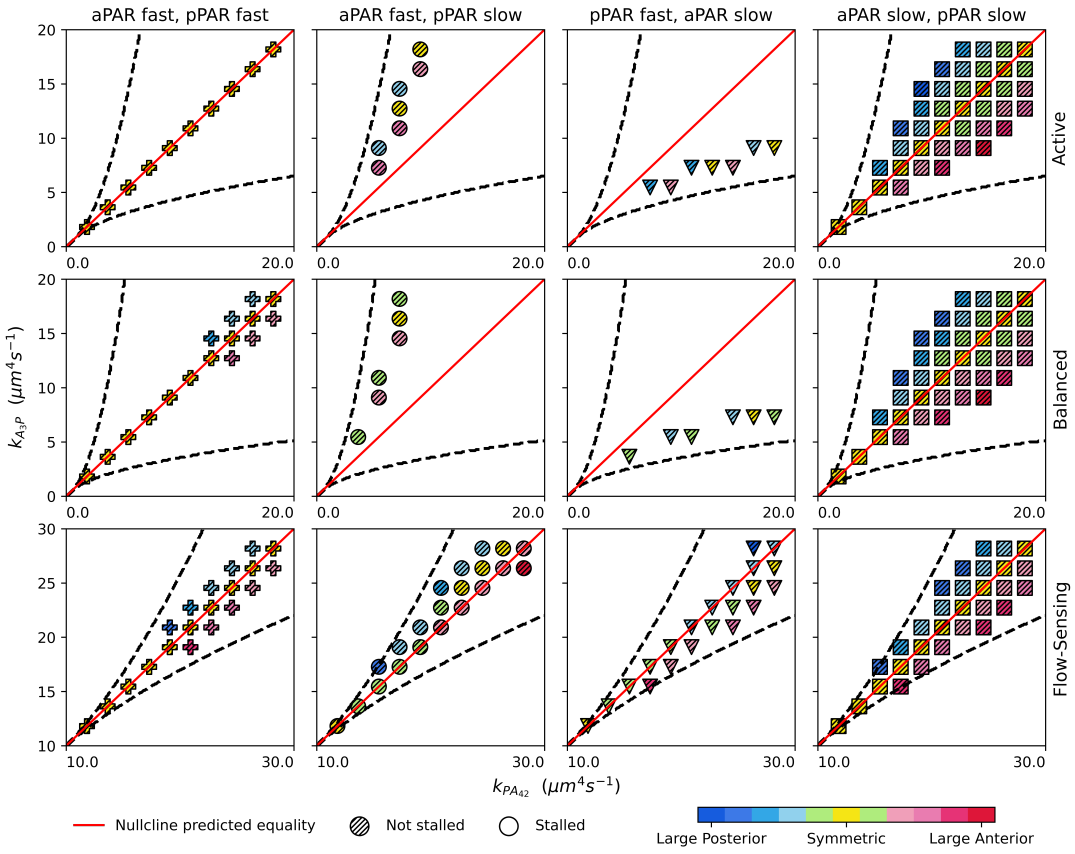


Figure 4.21: Biasing diffusivity of the active species requires a counter-balancing shift in relative antagonism to favour the opposing active species. The symmetric system is sensitive to relative antagonism when the diffusivity of the active species is fast. Polarising parameterisations of the symmetric model that result in domain formation from an initially artificially polarised state. Simulations therefore proxy polarity maintenance in the cell. Various diffusive regimes of the active species are represented.

The ability to maintain a polarised domain is a key component of the polarity process. However, the cell must first respond to the polarising cue and initialise the patterning template. We therefore moved to investigate the characteristic polarising ability of the symmetric model from a homogeneous steady state, fig. 4.22.

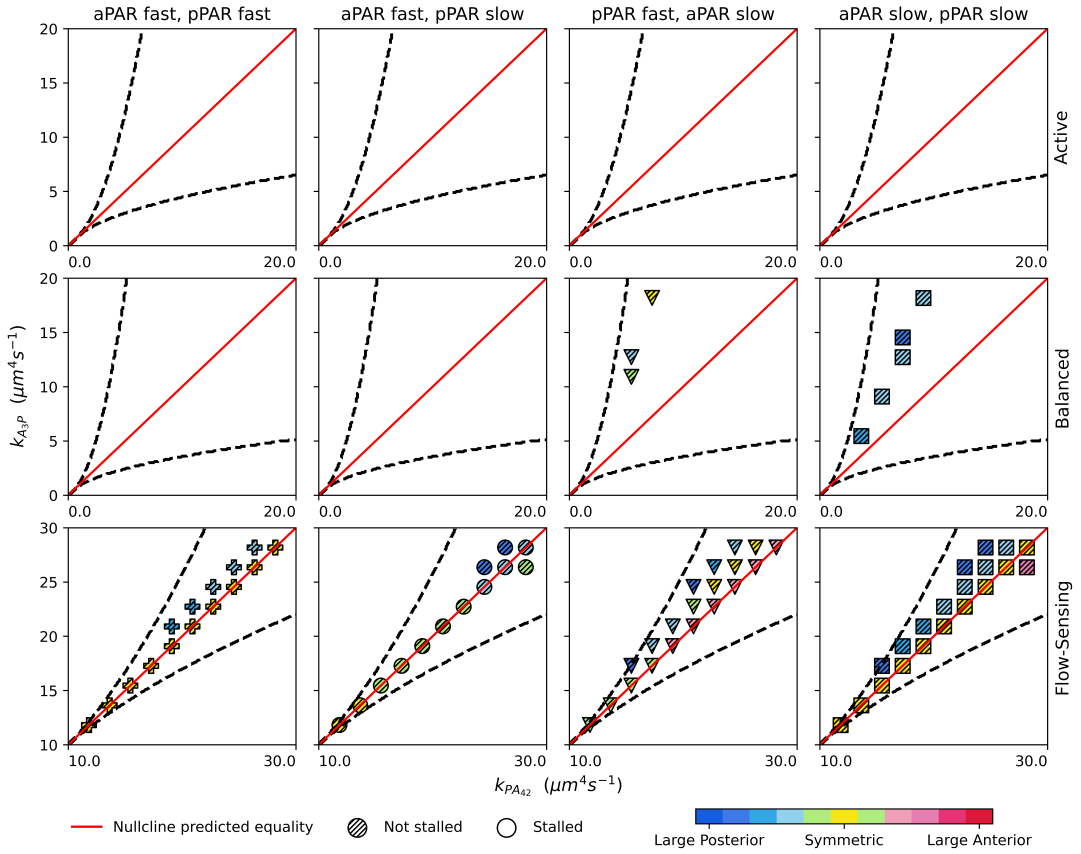


Figure 4.22: The symmetric system cannot polarise in response to cortical flows when in an active state. Polarising parameterisations of the symmetric model that result in approximately equal domain formation from an initially anterior homogeneous state. Various diffusive regimes of the active species are represented. Red indicates the position in antagonism phase-space of parametrisation that result in equal domain sizes, as predicted by nullcline analysis. Depth of colour indicates the enhanced size of the dominant domain, with yellow representing almost equal domains. Hashed represents an almost stalled state.

Most strikingly, the symmetric model is unable to to produce a final domain state under all diffusive regimes when in the active state. This behaviour continues in the balanced state when the diffusivity of the active posterior protein is fast. This illustrated hypersensitivity to diffusivity and antagonistic ability is expected in the symmetric model. The reduced flow-sensing pool is unable to properly segregate anterior protein and it is readily antagonised by the opposing active species. This inability to produce a patterning

template in the establishment phase of the polarisation process ultimately leads to a failure to polarise. In the balanced state when the diffusivity of the active anterior is slow, domain states can form however these are asymmetric with an over-expanded anterior. Again, the model ineffectively segregates in response to flows and so posterior binding is delayed and can only occur when the activity of the posterior species is increased. Delayed binding and clearance leads to a larger anterior as the domain slowly relaxes back toward the relatively clear posterior after establishment phase. In the flow-sensing state, the system responds well to flows and clears a larger posterior region which can be maintained by the posterior state at increased activity. In this flow-sensing state, the system cannot support domains where the activity of the anterior protein is increased as compared to the posterior. As the initial state of the membrane pre-establishment phase is anterior dominant, there is a bias toward active anterior membrane-bound protein. The active protein does not sense flows, is not translocated to the anterior and therefore remains in low concentrations across the membrane during establishment phase. When the antagonistic ability of this anterior protein is greater than that of the posterior it readily antagonises the posterior protein, excluding it from the posterior. As a result the system relaxes back to a homogeneous, anterior state.Our analysis of a symmetric model reveals fundamental design flaws in a model of polarity development that describes the aPKC with a cyclic motif. Whilst able to maintain a polarised state, the model is only able to effectively establish polarity when in a flow-sensing configuration.

4.4.4 Sensitivity in the coupled model of the aPKC cyle

Our above investigations of the extended aPKC models of cell polarity illustrate that the coupled model is a weak model candidate for robust polarisation. Characteristics of PAR protein behaviour, such as the inherent dissociation and diffusion rate and the rate of antagonism by opposing species serve to control the shape and positioning of the domain boundary. In a 2-PAR model of cell polarity, increased diffusivity of a species results in a shallower domain boundary, increased dissociation rate in a lower domain height and antagonism rates an expanded domain length favouring the more active protein [131]. Our investigation illustrates the delicate interplay of these characteristics,

particularly highlighting the importance of network topology when considering characteristics in combination. We find that coupling of the functionally distinct complexes in a directed cycle where production of the diffuse, active species relies on conversion from the flow-sensing, inactive species leaves the system sensitive to perturbation. The construction of such a loop leaves the system unable to balance system requirements for polarisation as favouring one regime comes at a direct cost to loss of the other dynamic regime and hence loss of functionality. This is particularly pertinent when considering the temporal requirements of polarisation: flexibility between a flow-sensing state in establishment phase and an active state in maintenance phase. The decoupling of dynamic behaviour and activity by means of this direct cycle therefore serves to obstruct, rather than aid robust and controllable polarisation.

4.5 Bayesian analysis to assess suitability of the extended aPKC cycle models of polarisation

We have explored the characteristic behaviour of both the coupled and uncoupled model under different system states and dynamic regimes. This exploration, found in section 4.4, illustrated the effect of the division of dynamic behaviour between an active, diffuse state and an inactive flow-sensing state. We found that both the coupled and uncoupled model were able to form domains, however, the coupled model was sensitive to perturbation - readily destabilised by both changes in relative diffusion of the active species and the relative concentration of active and flow-sensing species. Our grid search revealed the general behaviour for the models and gave insight into the possible mechanistic limitations of the network design: namely that mass-conservation coupled with a cyclic topology limits the flexibility of the coupled system. Having exposed the general behaviour of the coupled and uncoupled models we next moved to investigate the hypothesis that an aPKC cycle functions to enhance robustness of the advectively-triggered model of polarisation. Our grid analysis gives insight into the characteristic behaviour of our extended aPKC models and their sensitivity to perturbation of relative antagonism, relative concentrations of functionally distinct proteins and relative diffusivity of the active proteins. Whilst

this approach for gaining insight into the overarching robustness of the system, the grid analysis is limited to assessing sensitivity to perturbation from the perspective of where polarisation fails. Inevitably, as the antagonistic interactions in our extended models of cell polarity are non-linear, a finite regular grid will be unable to elucidate the onset of model breakdown in antagonism space.

We therefore turned to implement Approximate Bayesian Computation as a means to infer from data parameter sets that lead to quantifiable successful polarisation. Armed with this knowledge, we can then accurately assess the robustness of polarisation in the coupled and uncoupled models. Finally, we compare the results to polarisation in the 'simple' 2-PAR model to assess whether there is any advantage to polarisation endowed by the increased complexity of the extended aPKC models [70].

4.5.1 Approximate Bayesian Computation

Approximate Bayesian Computation is a computational statistical method that is used to infer the posterior distribution a model without having to first evaluate the associated likelihood. Its statistical basis is rooted in Bayes Theorem, which describes the following relationship between a parametric statistical model $p(D|\theta)$ which aims to describe a set of observations D:

$$p(\theta|D) = \frac{p(D|\theta)p(\theta)}{p(D)} \tag{4.35}$$

where $p(\theta|D)$ is the posterior, $p(D|\theta)$ is the likehood, $p(\theta)$ is the prior and $p(D)$ is the evidence. Unlike the frequentist approach to model evaluation - which evaluates against a null hypothesis, the Bayesian approach to model evaluation can infer model suitability based only on information constrained in the observed data [132].

For complex models, direct evaluation of the likelihood is usually either computationally expensive or analytically intractable. In these cases, estimation of the posterior distribution is instead carried out through the implementation of Approximate Bayesian Computation. Approximate Bayesian Computation implements a sampling regime to instead infer the posterior distribution of model parameters, θ - see fig. 4.23. Parame-

ter samples are drawn from a prior distribution which reflects the current knowledge of the system. Each parametrisation is simulated and the outcome compared to data and scored according to a costing criteria. In our implementation, we chose a costing criteria based on summary statistics as described in fig. 4.33. Simulations are then accepted or rejected based on an acceptance threshold. The distribution of the accepted parameters then represents the posterior distribution [133].

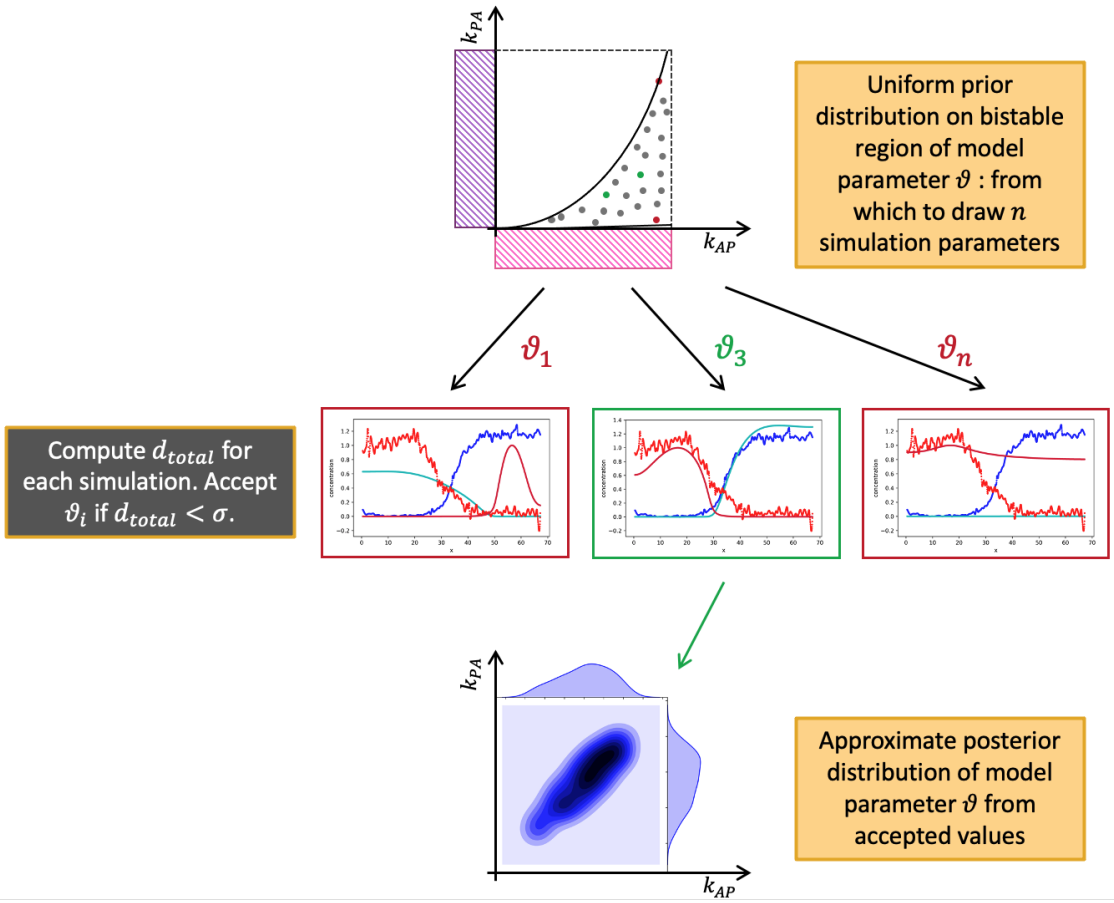
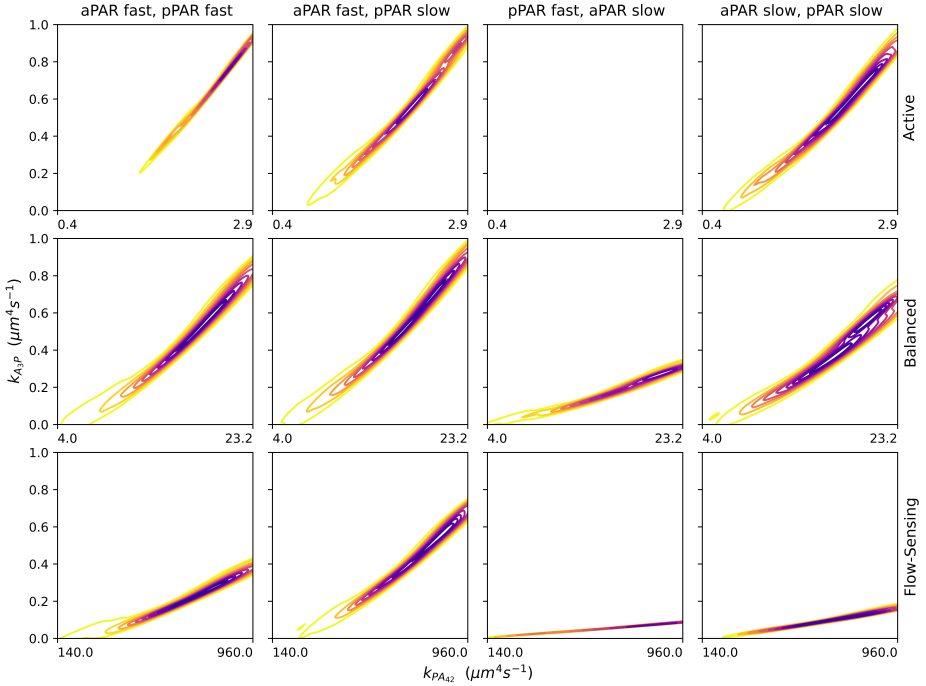


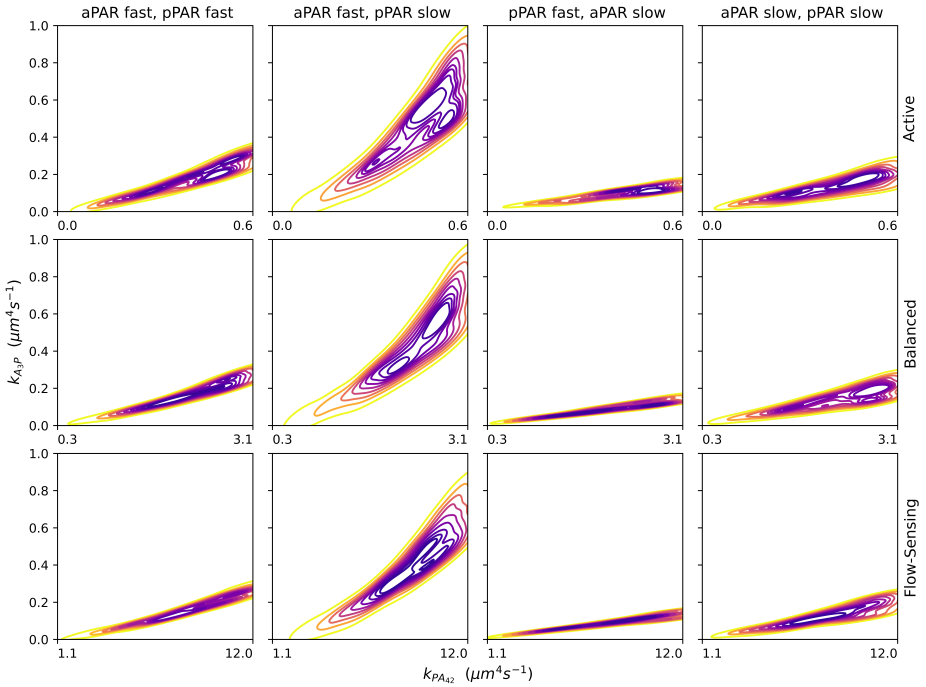
Figure 4.23: Scheme describing Approximate Bayesian Computation Model parameters are sampled according to a prior distribution. Simulations of the model defined by the parametrisations are then run and outputs scored against a costing criteria. Simulations are accepted or rejected based on the comparison of their score to a threshold. The distribution of the accepted simulations provides an estimate of the posterior distribution.

4.5.2 The uncoupled model polarises more robustly than the coupled model

We sampled antagonistic parameter sets (k_{PA},k_{AP}) from a uniform prior distribution for each diffusive regime, again comparing the models in different anterior configurations (active, balanced and flow-sensing). We defined successful polarisation by way of a distance measure calculated through summary statistics which combined a score for relative domain size, relative domain height and boundary gradient. To compare across models, we selected all simulations whose total distance was below a threshold as defined in section 4.6.3. With reference to fig. 4.24, it was found that our ABC implementation yielded characteristically similar results to our initial grid search for both the coupled and uncoupled model. Contrastingly, see fig. 4.24a, the Bayesian approach reveals a small region of polarisation for both the active state in a fast diffusive regime and the flow-sensing regime where the diffusivity of the anterior active species outstrips that of the posterior species. The elucidation of such a region reinforces our choice of methodological approach to assess model robustness. Coupled with the slowly-diffusing, flow-sensing state these regimes are characterised by an extremely compressed region of acceptance. As expected, there remains a complete failure to polarise in the active state when the diffusivity of the posterior active species outstrips that of the anterior species. Comparatively, the uncoupled model achieves successful polarisation across all sub-system states and diffusive regimes - see fig. 4.24b. Similarly to the results of the coupled model, the uncoupled model polarises least robustly in the state where the active posterior protein diffuses more quickly than the anterior species.



(a)



(b)

Figure 4.24: Bayesian Computation reveals compressed regions of successful polarisation in the coupled model. Contour map showing the regions of acceptance from Approximate Bayesian Computation for the **(a)** coupled and **(b)** uncoupled model in antagonism phase-space across 'active', 'balanced' and 'flow-sensing' system configurations for various diffusive regimes. All simulations were initialised with an anterior dominant homogeneous state. Accepted simulations are those with score below a universal threshold. The time period simulated encompassed both establishment and maintenance phase.

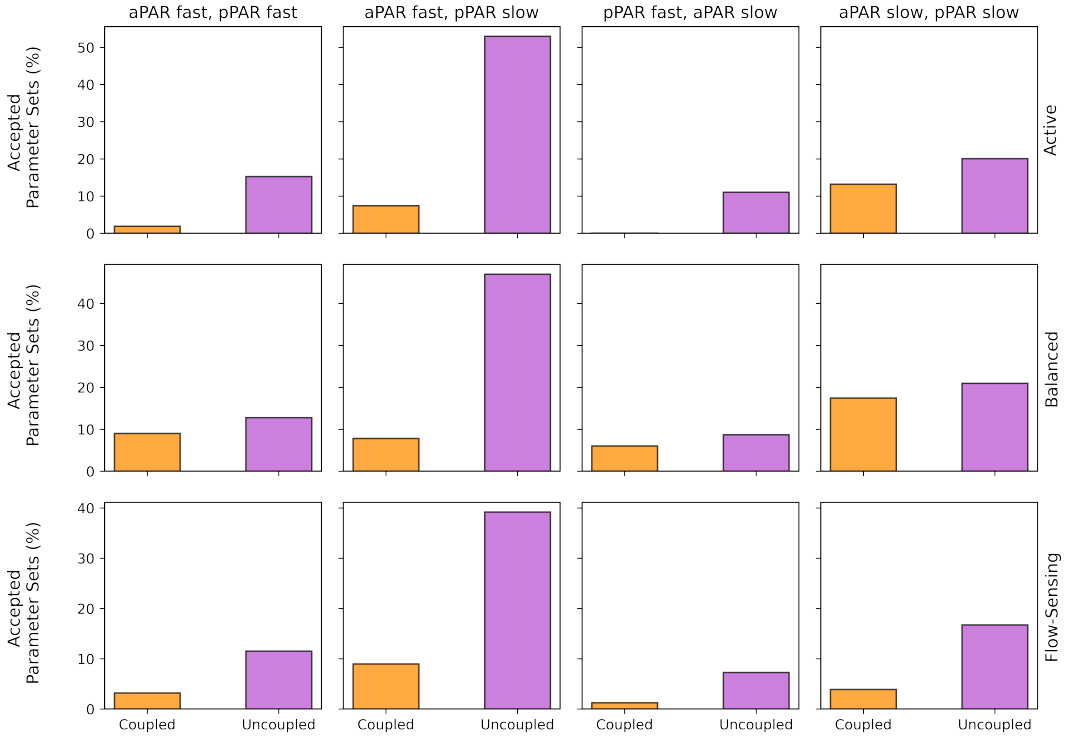


Figure 4.25: Polarisation in the uncoupled model is most robust when pPAR diffuses slowly. Number of accepted simulations from Approximate Bayesian Computation for the coupled and uncoupled model in antagonism phase-space across 'active', 'balanced' and 'flow-sensing' system configurations for various diffusive regimes. All simulations were initialised with an anterior dominant homogeneous state. The time period simulated encompassed both establishment and maintenance phase. Accepted simulations are those with score below a universal threshold.

Perhaps most strikingly, in all diffusive regimes the uncoupled network design is able to switch between an active and flow-sensing state without requiring a shift in relative antagonism of the active species. When the diffusivity of the anterior active species is slow, the required balance of antagonism is characteristically similar in the uncoupled model. Interestingly, the region of polarisation is not only stable across system states, but is also significantly expanded when the anterior active species diffuses more quickly than the posterior active species. Across all regimes the uncoupled model performs more robustly than the uncoupled model - see fig. 4.25. This is most noticeable in the fast-diffusing anterior, slow-diffusing posterior state, where the uncoupled model performs

twice as well as any other diffusive regime and almost five times as successfully as the coupled model.

4.5.3 The extended aPKC models are less robust to changes in relative antagonism than the 'simple' 2-PAR model.

Finally, we looked to quantify model robustness as compared to the 'simple' 2-PAR model. To reflect recent measurements of PAR diffusivity, we focused our model comparison on the fast-diffusing regime. For an overview of the characterisation of the 2-model, we refer the reader to section 4.2. We applied our ABC methodology to the 2-PAR model and again accepted parameter sets who distance measure was less than the threshold outlined in section 4.6.3. The regions of acceptance for each model and the score associated with accepted parameter sets is shown in fig. 4.26. In the case of the 2-PAR model, the total score was calculated as an average of the distance scores relating to the position of the domain boundary and the relative height of the domains. The distance contribution from the scoring of domain gradient was dropped as all simulations produced sufficiently steep gradients, earning a low resultant score and biasing the overall average such that larger scores for other summary statistics were accepted. The coupled and uncoupled model were scored according to average distance characterised by the position of domain equality, the gradient of the domains and the relative domain height.

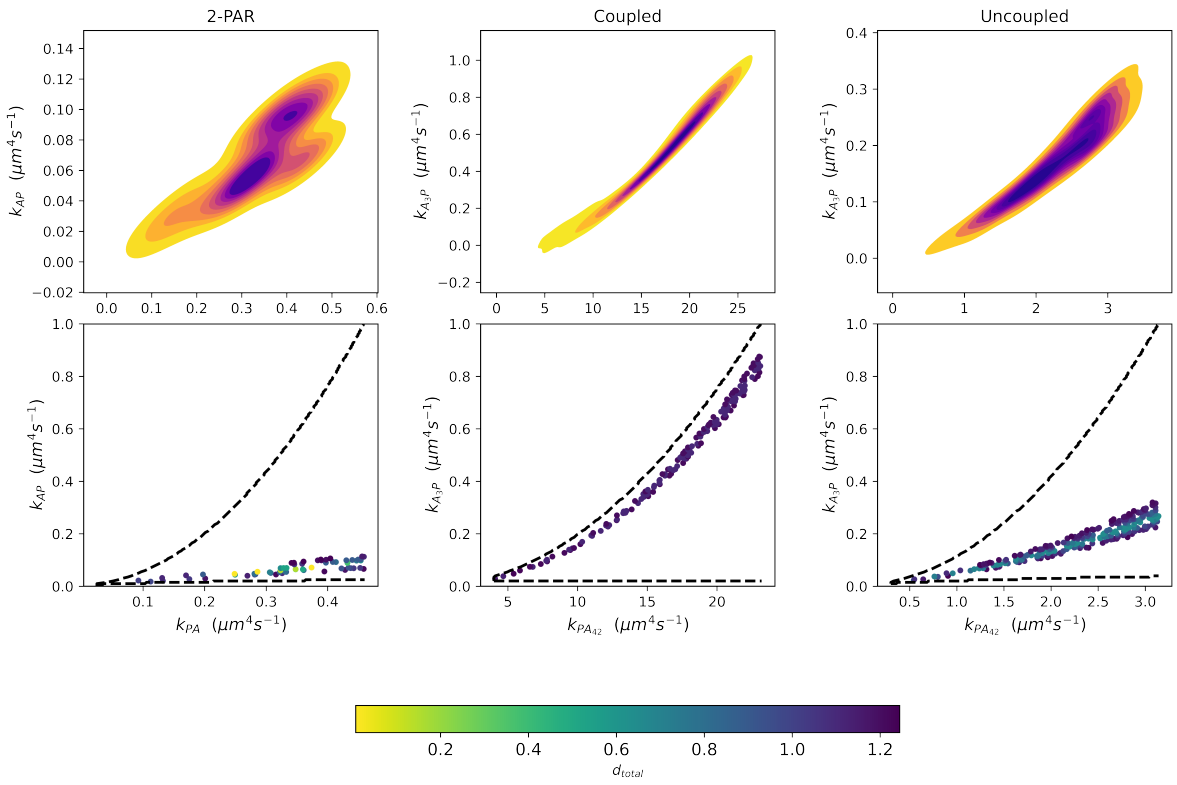


Figure 4.26: The extended aPKC models require increased control over relative rates of antagonism. Characterisation of the accepted simulations from Approximate Bayesian Computation in antagonism phase-space for the **Left** 2-PAR **Middle** Coupled and **Right** Uncoupled model. **Top** Kernel density estimates of the position of accepted sets in parameter space. **Bottom** Position of accepted sets in the bi-stable region. Colouring indicates the distance score, d_{total}, normalised across all models. All simulations were initialised with an anterior dominant homogeneous state. Accepted simulations are those with score below a universal threshold. The time period simulated encompassed both establishment and maintenance phase.

In the case of the extended polarity models, it is imperative to include the domain gradient statistics as the decoupling of the anterior population into functionally and dynamically distinct complexes affects the overall gradient of domain formation (previously discussed in section 4.4.1.1). We find that the region of acceptance is most compressed in the coupled model. With reference to fig. 4.28 we find that the 2-PAR model presents parametrisations with the lowest scores (fig. 4.28a), whilst the coupled model is characterised with the worst scoring simulations (fig. 4.28c). We find that the coupled model is unable to balance domain concentration or gradient in all simulations and is unable to

respond well to polarising flows - fig. 4.29c, fig. 4.29d. Contrarily, both the 2-PAR and uncoupled model respond well to flows and control relative domain concentrations - see fig. 4.29.

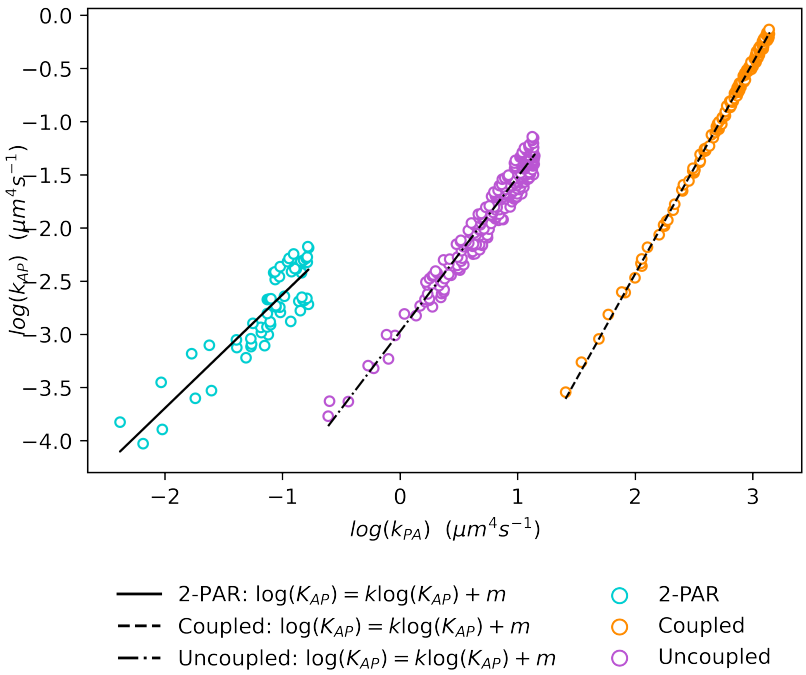


Figure 4.27: Position of accepted simulations in the (log-log) antagonism phase-space for the: 'simple' 2 PAR model (turquoise), the coupled model (orange) and the uncoupled model (purple). Dashed lines indicate log-log line of best fit to data. Region of acceptance is most tightly-bound for the coupled model, with a correlation coefficient $R = 0.998$. All simulations were initialised with an anterior dominant homogeneous state. The time period simulated encompassed both establishment and maintenance phase.

Model	k	m	R-squared
2-PAR	1.07	0.21	0.790
Coupled	1.98	0.00166	0.998
Uncoupled	1.45	0.0511	0.951

Table 4.1: Best fit to accepted simulation data in log-log space: $\log(k_{AP}) = k\log(k_{PA}) + m$.

The region of acceptance of the coupled model is tightly constrained and this is further illustrated in fig. 4.27 where the accepted sets lie closely to an exponential fit - $R^2 = 0.998$, indicating hyper-sensitivity to the relative antagonism of the active species. As the stoichiometry of the antagonistic terms define the functional form of the monostable/bi-stable boundary it is unsurprising that in the case of the coupled model,

where the region of acceptance is located tightly along the posterior-monostable/bi-stable boundary, that the exponent of this fit ($k = 1.98$) is close to $\alpha = 2$. Polarisation in the uncoupled model occurs more centrally in the bi-stable region than the coupled model and so the relationship defining relative PAR activity is relaxed ($k = 1.45$). However, with reference to fig. 4.27, it can be seen that splitting of the anterior species into functionally distinct complexes negatively affects robustness of polarisation - identifiable through the compression in the region of accepted parameter sets for both the coupled and uncoupled model as compared to the 2-PAR model. Unlike the extended models of cell polarity, the 2-PAR model encompasses both a symmetric network topology and near-balanced reaction and diffusion rates of the opposing PARs. This results in a near-linear relationship in the ratio of the antagonism rates of the parameter regimes accepted through our ABC implementation. In our investigations of the symmetric model (section 4.4.3), we illustrated how this symmetry enhances the model ability to maintain polarised domains. Dissimilar to the extended symmetric model, where the dynamic behaviour of the proteins are functionally distinct, the dynamics of the species in the 2-PAR model are encompassed in the single protein complex. To this end, the 2-PAR model overcomes the limitations present in the extended models as a result of the dynamically distinct sub-species in the mass-conserved system. In the extended models, the anterior active and inactive species have different dynamic characteristics which result in an increased sensitivity to relative antagonism. This is particularly apparent in the coupled model, where the upregulation of one sub-species directly down-regulates the availability of the other anterior sub-species. Whilst the 2-PAR model is able to remain more robust to relative antagonism it remains that, unlike the extended models, this 'simple' description of cell polarisation is inflexible to specialisation of functionality at different points in the cell cycle. This may have adverse effects on the robustness of polarisation when considering the model in the context of external factors, such as the variability in signal transducing molecular players that act upstream of the PAR proteins in the asymmetric division of the cell.

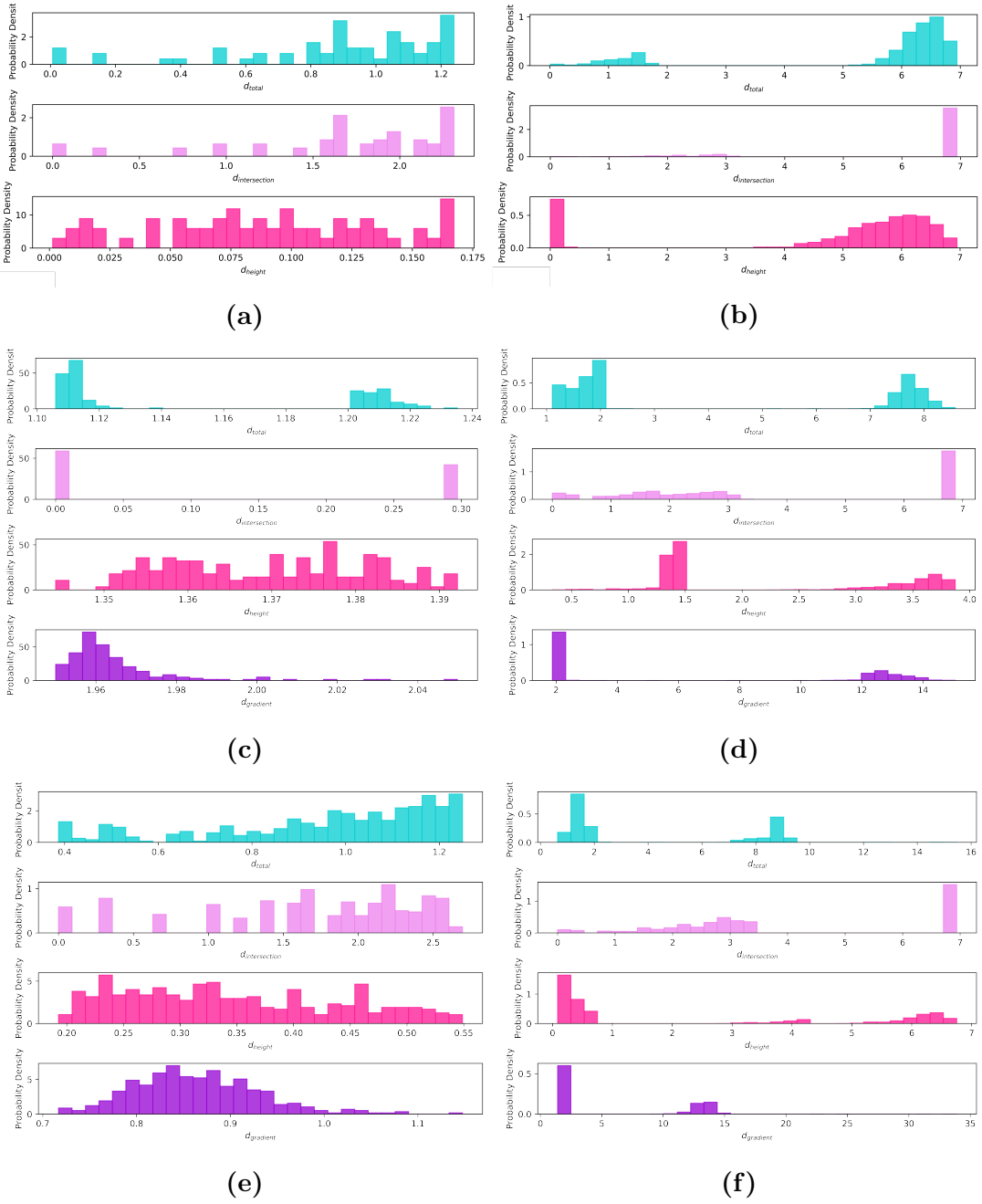


Figure 4.28: Summary statistics reveal that the coupled model is unable to balance domain concentrations and domain gradients. Conversely, the uncoupled model consistently controls these characteristics. Histograms of distance scores arising from the **(a)** 2-PAR model accepted parameter sets **(b)** 2-PAR model all parameter sets **(c)** coupled model accepted parameter sets **(d)** coupled model all parameter sets **(e)** uncoupled model accepted parameter sets **(f)** uncoupled model all parameter sets.

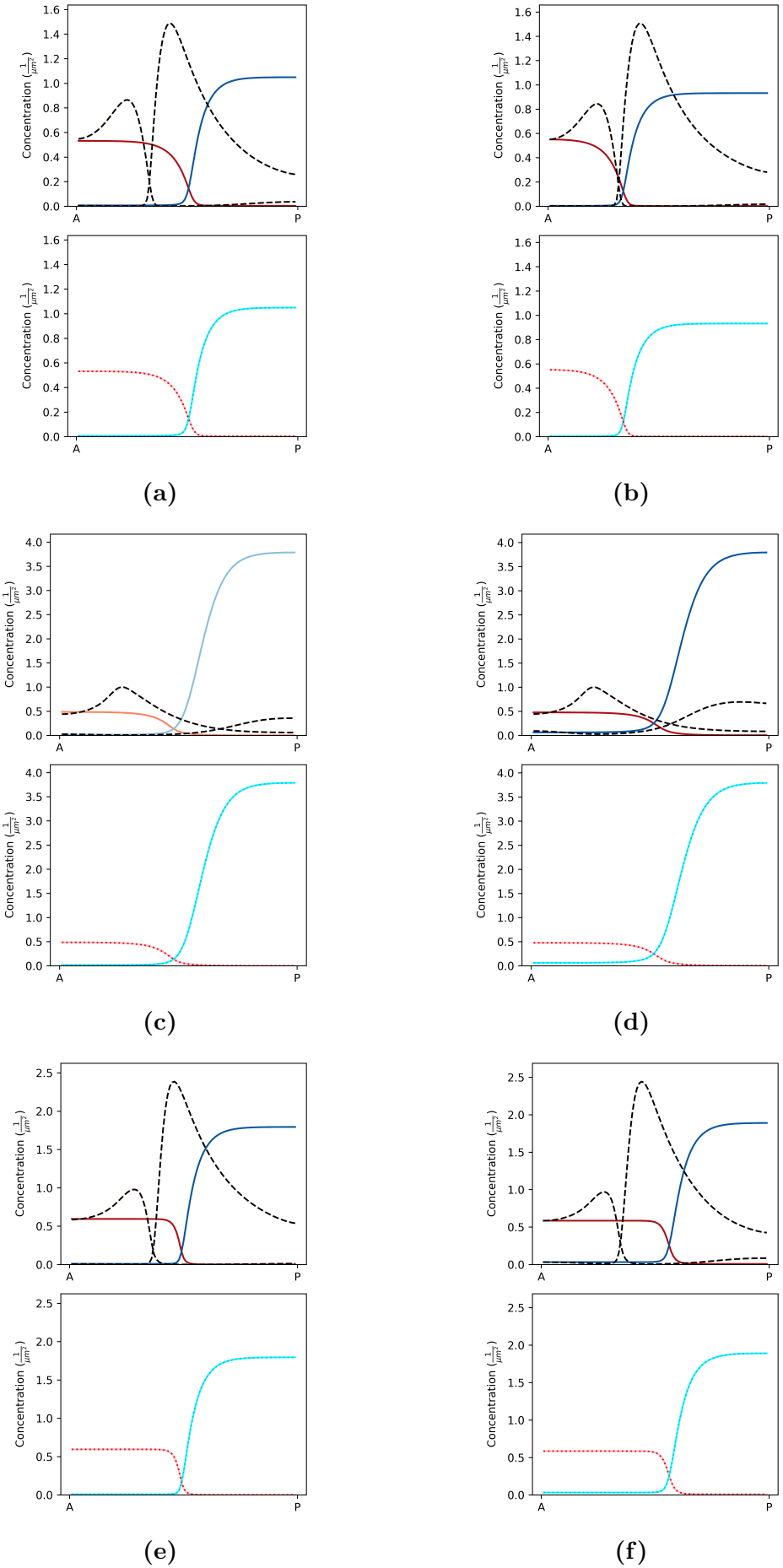


Figure 4.29: Polarity profiles of the highest and lowest scoring accepted parameter sets. The lowest scoring sets for the **(a)** 2-PAR model, **(c)** coupled model, **(e)** uncoupled model. The highest scoring sets for the **(b)** 2-PAR model, **(d)** coupled model, **(f)** uncoupled model.

4.5.4 Discussion

In this chapter, we looked to uncover the design principles underlying networks describing successful polarisation in the *C. elegans* zygote. We investigated two opposing polarity network designs that described the relationship between opposing functional modules in the anterior PAR group and assessed their biological viability, limitations, and robustness of polarisation. The biochemical networks we investigated encompassed an aPKC cycle, where PAR-6/aPKC cycled between a flow-sensing, inactive PAR-3 associated complex and an active, diffuse CDC-42. In the coupled model, this cycling was directly coupled, with PAR-6/aPKC loading to the membrane exclusively via PAR-3. In the uncoupled model, PAR-6/aPKC was decoupled from the PAR-3 complex, instead undergoing enhanced membrane binding in the presence of PAR-3.

Previous modelling of the PAR system has uncovered important design principles of polarity networks: mass-conservation which enables cytoplasmic depletion and domain stalling, non-linear reaction terms to endow bi-stability and advective-triggering by cortical flows [126][45][70]. Incorporating these principles into our network design, we utilised reaction-advection-diffusion modelling model each network throughout establishment and maintenance phase. Alike the wave-pinning model of Goehring et al. the flow-sensing species in our PAR polarity networks were passively advected by cortical flows, which we represented by a flow profile approximated from our investigations in [70].

We found that the coupled model is hyper-sensitive to perturbation of antagonism and requires a significant bias in relative activity of the CDC-42/PAR-6/aPKC complex as compared to the posterior species. This is likely biologically unviable, with over-expression of aPKC and CDC-42 activity being implicated in loss-of-function or aberrant cell behaviour [134].

Both the coupled and uncoupled model could respond to a polarising cue to establish and maintain domains. However, the ability of the coupled model to sense flows is limited and so the coupled model relies on antagonism to clear the posterior and complete polarity establishment. Polarisation is known to occur in response to both a cortical guiding cue (flow) and a posterior cue (antagonism) [71]. Therefore, whilst polarisation does not

solely rely on response to cortical flows, the reliance on the posterior cue results in slowed polarity establishment in the coupled model. Polarisation of embryos as a result of the posterior 'rescue pathway' is observed *in-vivo*, but the time to reach steady state is longer than that observed in zygotes polarising in response to flows - alike that observed in our simulations [70][135]. Interestingly, recent measurements of cortical flows show that peak flows are present for a shorter period of time than implemented in our model and so it is likely that the success of polarisation in our modelling represents an optimistic view [71].

Through exploration of a symmetric coupled model, we identified that the failures of the coupled model are a result of the cyclic motif in the anterior biochemical network. In an extended aPKC model characterised by mass-conservation, this motif spatially constricts the production of active anterior material. Additionally, removal of the PAR-3/PAR-6/aPKC complex through antagonism reduces the available active pool even further. Decoupling of the cue-sensing, inactive anterior complex from the diffuse, active complex forces an inherent trade off between responsiveness to flows and antagonism of the posterior PAR.

An aPKC cycle as described by the 'coupled' model is hypothesised to endow the PAR polarity system with the ability to tune its internal composition, favouring functionally advantageous PAR modules at relevant times in the cell cycle [78]. To simulate these temporally advantageous states, we configured the coupled model in either an 'active' or a 'flow-sensing' anterior state. The former represents a primarily signal-receiving state, reflecting the upregulation of PAR-3/PAR-6/aPKC seen during establishment phase [45]. The latter represents a signal-transducing stage, reflecting the preferential formation of the diffuse, active CDC-42/PAR-6/aPKC complex that has been observed in vivo [60]. We found that the coupled model performed poorly in all configurations which instead worked to amplify the constraints of polarisation imposed by the cyclic motif.

In the 'flow-sensing' configuration, polarisation occurred but required an unviable $1000-fold$ higher activity of the anterior protein. In the 'active' state, sensitivity to relative antagonism was amplified. As a result of mass-conservation, the much-diminished flow-sensing pool could not respond to flows. To enable polarisation, the system required

the relative activity of the posterior species to be maximised and so polarisation occurred close to the edge of bi-stability. A small perturbation to antagonism therefore resulted in either an anterior homogeneous state – where posterior PAR had been unable to clear the posterior through antagonism, or a posterior homogeneous state – where the system destabilised, and the posterior domain expanded to the full length of the embryo. Microtubule-cortex action works downstream of polarity establishment to stabilise and correct errors in boundary positioning during polarisation, enabling precise cytokinesis [136]. Therefore, a maintenance state in which polarisation is readily lost like that representing the active state of the coupled model is unlikely to represent the mechanism of polarisation *in-vivo*.

Our Approximate Bayesian Computation implementation revealed that the splitting of the anterior population into functionally distinct complexes reduced the robustness of polarisation to changes in relative antagonism as compared to the simpler 2-PAR model. However, as compared to the coupled model, the region of polarisation of the uncoupled model remained consistent across anterior system configurations for various diffusive regimes. Unlike the coupled model, the PAR-6/aPKC can bind independently of PAR-3, which instead works to enhance PAR-6/aPKC membrane binding. This alleviates the constraints on polarisation imposed in the coupled model network topology leading to enhanced robustness of polarisation.

Interestingly, the uncoupled model polarised most robustly when the diffusivity of the posterior protein was slowed. To enhance robustness of polarisation, the uncoupled model requires an enhancement in activity of posterior PAR. Recent work has indicated that alike PAR-3, the posterior PAR network contains a clustering species CHIN-1. CHIN-1 is known to inhibit activity of CDC-42, with clustering enhancement occurring during polarity maintenance phase [65]. With the knowledge that PAR-3 clusters modulate their dynamics by slowed diffusion, these observations could indicate an important posterior candidate for control of a robust extended model of PAR polarity. In summary, the uncoupled model could provide the PAR system with a means in which to temporally favour functional complexes in order to drive successful polarisation of the *C. elegans*

zygote.

4.6 Methods

4.6.1 Processing and assessing steady states

4.6.1.1 Linear stability analysis

Linear stability analysis about the homogeneous solution was implemented to assess the stability of model parametrisations. In the antagonism phase-space (k_{AP}, k_{PA}), for $\alpha \geq 1, \beta > 1$ or $\beta \geq 1, \alpha > 1$ the system can give rise to multi-stable solutions representing either an anterior or posterior dominant state [70]. Stability analysis was carried out according to a gridsearch in the k_{AP}, k_{PA} phase-space, with all other parameters fixed according to appendix A. For a general system of three interacting species A_1, A_2, P linear stability analysis would be carried out as follows:

1. **Calculate fixed points from nullclines**

   Solve the nullcline system to obtain the homogeneous fixed solution, x^*:

   $$F(R_{A_1}, R_{A_1}, R_P)|_{x^*} = 0$$

   where R_{A_1}, R_{A_2}, R_P represent the reaction terms of the reaction-advection-diffusion system:

   $$\begin{aligned} \partial_t A_1 &= D_{A_1} \partial_{xx} A_1 - \partial_x (v A_1) + R_{A_1} \\ \partial_t A_2 &= D_{A_2} \partial_{xx} A_2 + R_{A_2} \\ \partial_t P &= D_P \partial_{xx} P - \partial_x (v P) + R_P \end{aligned}$$

2. **Construct the Jacobian matrix**

$$J(A_1,A_2,P) = \begin{bmatrix} \partial_{A_1}A_1 & \partial_{A_2}A_1 & \partial_P A_1 \\ \partial_{A_1}A_2 & \partial_{A_2}A_2 & \partial_P A_2 \\ \partial_{A_1}P & \partial_{A_2}P & \partial_P P \end{bmatrix} \tag{4.36}$$

3. **Compute eigenvalues, λ by solving the characteristic equation**

$$det(J|_{x^*} - \lambda I) = 0 \tag{4.37}$$

Initital searches in antagonism phase-space were carried out to focus the region such that the point of emergence of the bifurcation line between mono-stable posterior and multi-stable state, $f_{bif,mp}$ was aligned with the origin and the maximum k_{AP} value. Once the search region had been aligned according to these constraints, stability calculations were then carried out across a $200x200$ grid.

$$f_{bif,mp}(k_{PA})|_{k_{PA}=min} = 0 \tag{4.38}$$

and

$$f_{bif,mp}(k_{PA})|_{k_{PA}=max} = 1 \tag{4.39}$$

Linear stability analysis was carried out in Mathematica. Phase-space visualisations were produced using Python.

4.6.1.2 Assessing the form of bifurcations

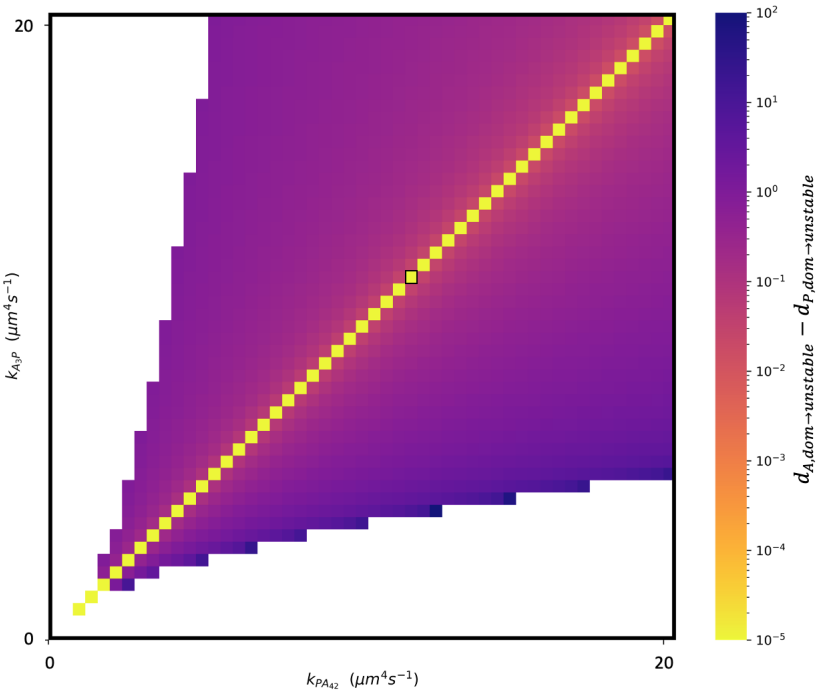
The antagonism phase-space is divided into multi-stable and mono-stable regions depending on the system stability (refer to section 4.6.1.1 for details on stability calculations). The boundaries dividing these regions represent bifurcations: points where depending on the direction of perturbation, the system would be driven to either of the mono-stable or multi-stable states. The forms of these bifurcations were calculated using the polyfit

class of the NumPy package. The bifurcation lines were fit to a function of the form:

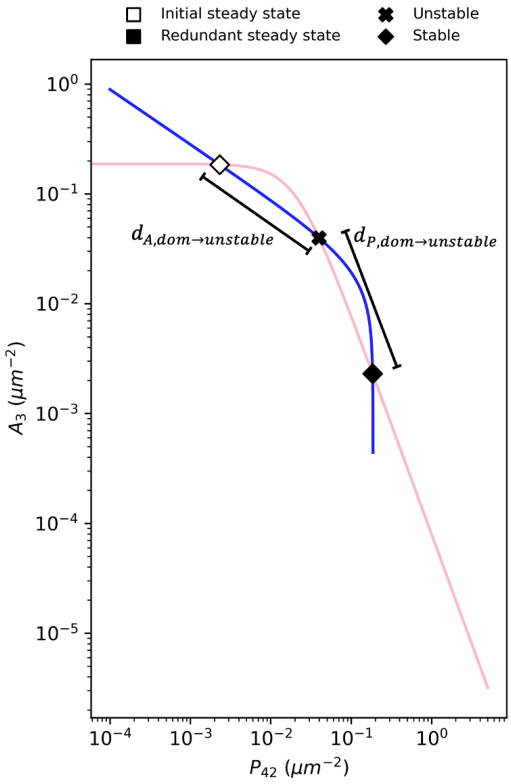
$$y(x) = Ae^{Bx} + C \tag{4.40}$$

4.6.1.3 Prediction of domain equality from the homogeneous steady state

The predicted position of domain equality in antagonism phase-space was calculated using the position of steady states calculated in our linear stability analysis (section 4.6.1.1). Within the multi-stable region, the Euclidean distance between the posterior dominant, stable state and the unstable state was compared to the Euclidean distance between the anterior dominant, stable state and the unstable state. When the difference between these distances was minimised, the corresponding grid point was denoted as the location where domain equality was predicted. Accuracy of this method is therefore limited by the width of the grid separation.



(a) The difference between the Euclidean distance separating the anterior/posterior stable and unstable steady states.



(b) Nullclines of parametrisation of the symmetric system corresponding to the black square in **(a)**.

Figure 4.30: The separation of steady states can predict the position of domain equality. **(a)** The difference between the stables anterior/posterior dominant state and the unstable state is minimised in a symmetric system when the antagonistic ability of each species is balanced ie. $k_{AP} = k_{PA}$. **(b)** An example showing the nullclines of the symmetric system in a parametrised state where the size of the polarised domains is predicted to be equal ie $d_{A,dom\to unstable} = d_{P,dom\to unstable}$.

4.6.2 Numerical simulations

Initially, a custom finite-difference solver was created in Python to enable numerical simulation of the PAR systems. Other numerical methods - such as spectral methods or finite element methods - could have been implemented to solve the coupled non-linear differential equations that describe the PAR system. However, the finite-difference approach was taken due to its tractability, especially when considering simulation in $1D$. The general principle of finite difference methods involves the discretisation of the simulation domain into a grid, where at each grid point the derivative in the equation is approximated using Taylor expansions around the grid point [137]. The form of the Taylor expansion results in schemes that are forward, backward or centered differencing and the order of the expansion denotes the final order of accuracy of the scheme.

The PAR system is described by advective (bulk transport in response to flows) and diffusive dynamics. The operators describing these dynamics are characteristically distinct and therefore require distinct numerical schemes to efficiently describe their dynamics. To this end, we implement Lie splitting, allowing us to separate the effect of advective and diffusive dynamics and instead solve two simpler sub-systems; one describing the evolution of advection and the other the evolution of diffusion. A Crank-Nicolson method was implemented to solve for the diffusive motion, as it is both second order accurate and unconditionally stable according the von Neumann analysis [138]. A Beam-Warming scheme was implemented to solve for the advective motion, as it is a second order accurate scheme and correctly handles the spatially variant velocity function due to its biased nature (see fig. 4.9) [139]. This solver was written in Python and similarly to the work of Goehring et al., the simulation domain was a $1D$ line of length L with periodic boundary conditions.

The accuracy and stability of the numerical solution described by a finite difference scheme is limited by the separation of evaluation points in the grid. This results in trade-offs between accuracy of the solution and computational efficiency. It is prudent to maximise the grid spacing - therefore minimising computational time - whilst still satisfying the stability criteria associated with the numerical scheme of choice. Spatial,

Δx, and time, Δt, step choices were constrained according to the following three stability criteria:

1. **Courant-Friedrichs-Lewy condition**:

$$\frac{v_{max}\Delta t}{\Delta x} \lessapprox 1$$

This condition dictates that the characteristic line passing through a given grid point must be contained within the numerical domain of dependence - information through a given grid point must be contained within its neighbours within a given time increment.

2. **Peclet condition**:

$$\frac{v_{max}\Delta x}{D} \lessapprox 2$$

This condition governs the ratio of advective to diffusive transport.

3. **Thermal diffusivity ratio**:

$$\frac{D\Delta t}{\Delta x^2} \lessapprox \frac{1}{2}$$

Figure 4.31 describes the process implemented over time to solve an equation of the form:

$$\frac{\partial u(x,t)}{\partial t} = D\frac{\partial^2 u(x,t)}{\partial x^2} - \frac{\partial (v(x)u(x,t))}{\partial x} + Reactions \tag{4.41}$$

where M_{adv} arises from the Beam-Warming method:

$$u_i^{n+1} = \big(1 - \frac{\lambda^2}{2} - \frac{3\lambda}{2}\big)u_i - (\lambda^2 + 2\lambda)u_{i+1} + \big(\frac{\lambda^2}{2} + \frac{\lambda}{2}\big)u_{i+2}$$

and P_{diff}, Q_{diff} from the Crank-Nicolson method:

$$-\sigma u_{i-1}^{n+1} + (2+2\sigma)u_i^{n+1} - \sigma u_{i+1}^{n+1} = \sigma u_{i-1}^n + (2-2\sigma)u_i^n + \sigma u_{i+1}^n$$

Accordingly,

$$\lambda = \frac{v_{max}\Delta t}{\Delta x^2}$$

$$\sigma = \frac{D\Delta t}{\Delta x^2}$$

Solver accuracy was benchmarked against Mathematica NDSolve. The 'simple' 2-PAR system (section 4.2) was simulated for $t = 800\,\mathrm{s}$. The custom solver yielded comparable solutions to numerical simulations using Mathematica's NDSolve - see fig. 4.32.

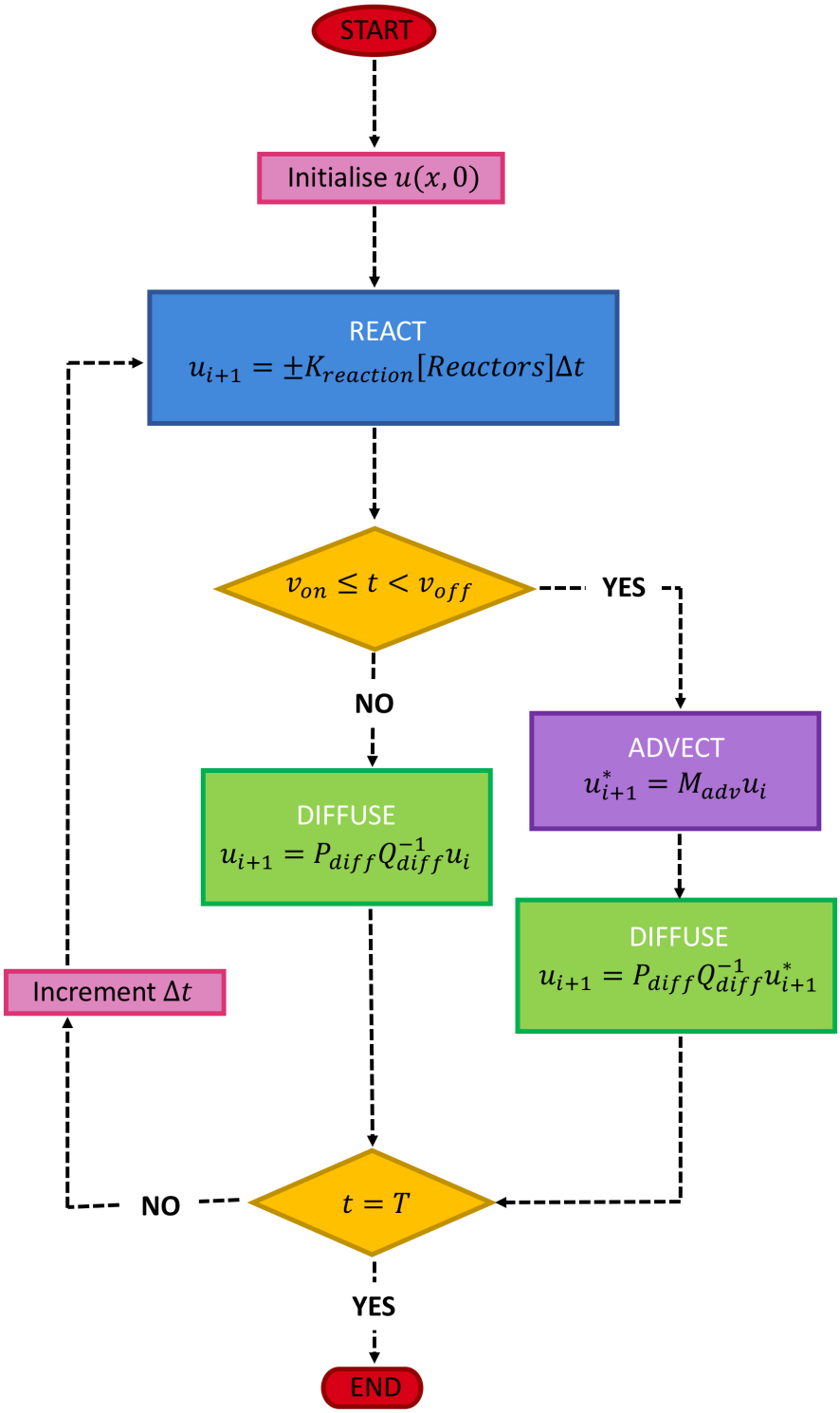


Figure 4.31: Algorithm describing the custom-built numerical solver. Described is the spatio-temporal evolution of a concentration of species, u.

This solver could be implemented using parallelised batch processing and so trade-offs between computational time and accuracy of the solver were feasible. However, when considering times beyond that of usual polarisation (ie. $t > 2000\,\mathrm{s}$) the stiffness of

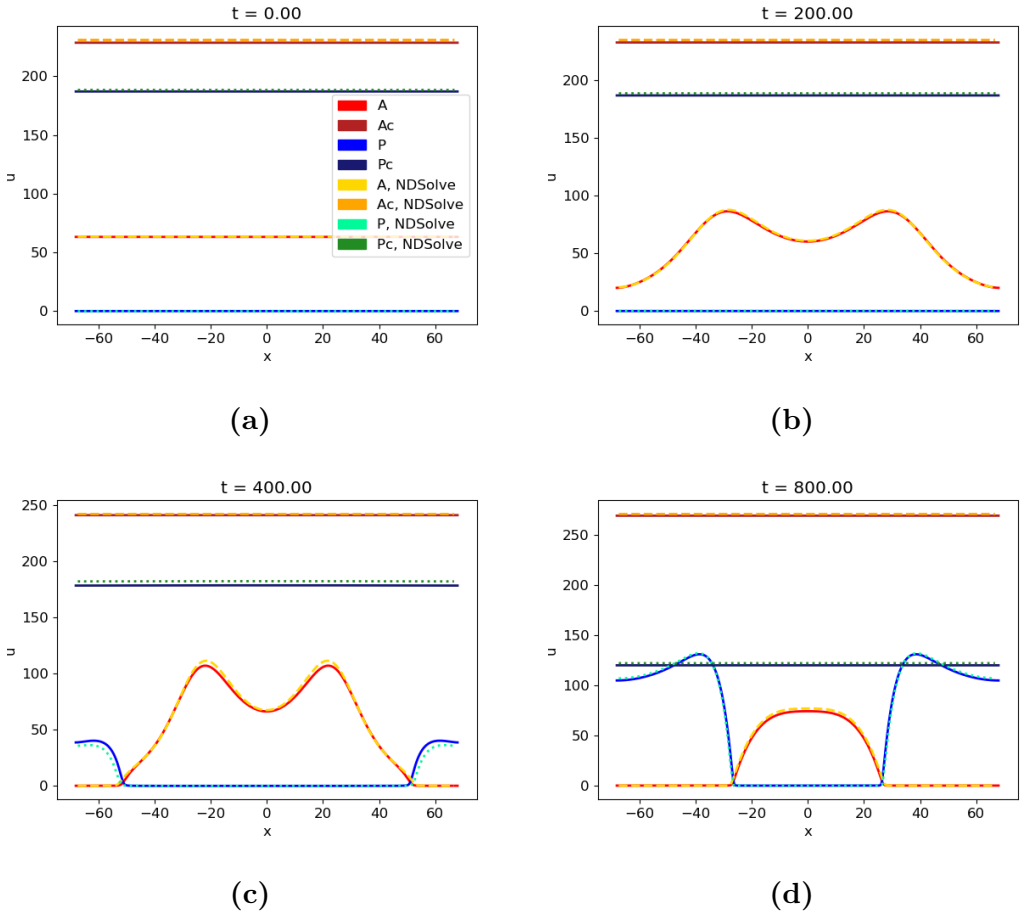


Figure 4.32: Spatio-temporal evolution of the 2-PAR system. Solutions derived from the custom-built solver are compared with Mathematica NDSolve. Dynamics as described in the 2-PAR model. Dashed lines represent NDSolve solutions, solid lines represent finite difference RAD solutions. **(a) - (d)** represent snapshots at $t = 0, 200, 400, 800s$ respectively. Centralised about 0 is the position of the anterior pole, with the posterior centered around $\pm\frac{L}{2} = 68\,\mu\text{m}$

the coupled non-linear system required a time-step for stability that was too small to be computationally feasible when considering the long simulation times of $t > 30000\,\text{s}$. Therefore, these simulations were instead carried out using the NDSolve function in Mathematica.

4.6.2.1 Scoring polarisation outcomes

Simulations were assigned broad criteria relating to their success of polarisation. The position of the domain boundary and the relative height of the polarising domains were considered. In the grid analysis, domains were considered to satisfy the criteria for boundary positioning and relative domain heights if:

$$x_{intersection} = \frac{L}{4} \pm \frac{L}{16} \tag{4.42}$$

$$\frac{conc_A}{conc_P} = \frac{1}{2} \pm \frac{1}{4} \tag{4.43}$$

4.6.3 Approximate Bayesian Computation

4.6.3.1 Stall point of polarisation

The stall point of polarisation was approximated through monitoring of the change in position of the domain boundary. Simulations were run for $\tau = 30000\,\mathrm{s}$. All instances where the boundary position remained stationary for $\tau = t_{stall}s$ were then found. The analysis sought to maximise the stationary duration τ. Initial stall durations of $\tau = 10000\,\mathrm{s}$ were searched for. If this search failed, stall times were incrementally decreased until a lower bound $\tau = 5000\,\mathrm{s}$ was reached.

Importantly, our analysis considered the relative domain height as a metric for successful polarisation. Therefore, each time-point fulfilling the stalling requirement on the position of the domain boundary was additionally analysed to check that domain concentrations had relaxed to their steady state. This is particularly important in flow-sensing simulations which respond well to flows and so take on a steep asymmetry in their domain profile as a result of advection. Domains were considered to have relaxed when the temporal change in domain profile changed by less than 1%.

The first instance that satisfied both the requirements for boundary stalling and domain relaxation was considered the stall point of the simulation and this spatial profile was used to score the simulation outcomes. If no time-point that satisfied both the requirement on boundary stalling and domain relaxation was found, the simulation was scored based on the final time-point $t = 30000\,\mathrm{s}$.

4.6.3.2 Summary statistics

Polarisation outcomes were allocated a score based on the weighted average of three summary statistics - the position of domain intersection, the relative height of domains

and the average domain gradient. The average of these scores then denoted the total score d_{tot} for the simulation.

$$d_{tot} = \frac{1}{3}\sum d_{intersection} + d_{height} + d_{gradient} \tag{4.44}$$

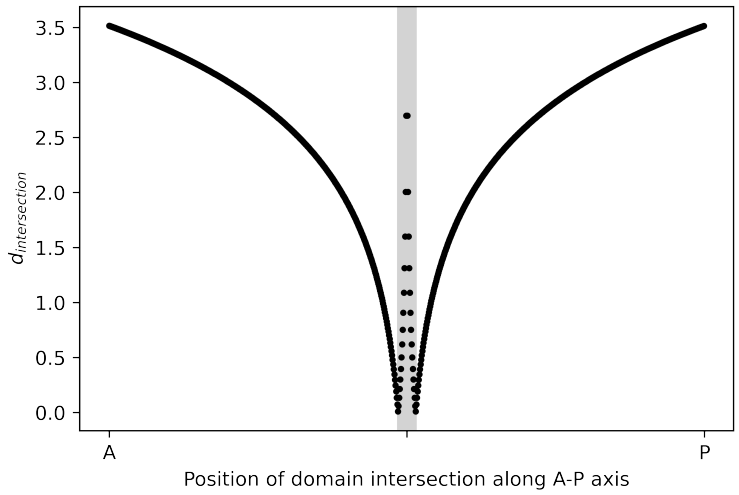
The scoring of the summary statistics ($d_{intersection}, d_{height}, d_{gradient}$) took the following forms:

$$d_{intersection} = \begin{cases} 0, & \text{if } \left(\frac{L}{4} - 1\right) \leq x_{intersection} \leq \left(\frac{L}{4} + 1\right) \\ \log\left(|\frac{L}{4} - x_{intersection}|\right), & \text{otherwise} \end{cases} \tag{4.45}$$

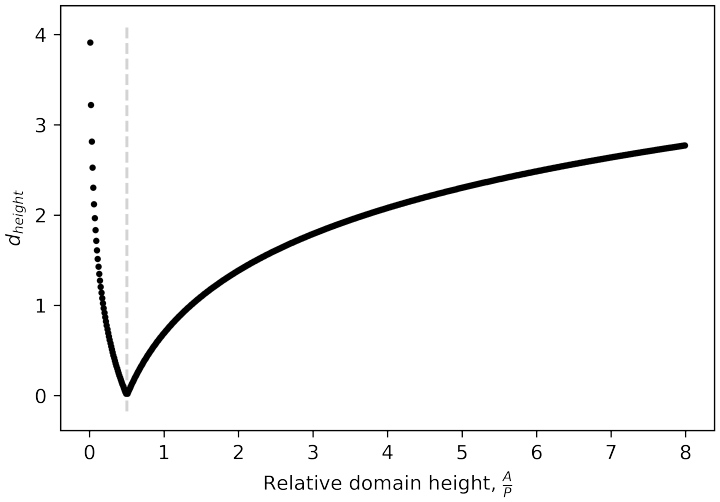
$$d_{height} = |\log\left(\frac{L}{2}\right) - \log\left(\frac{conc_A}{conc_P}\right)| \tag{4.46}$$

$$d_{intersection} = \begin{cases} \log\left(\frac{2}{grad_A + grad_P}\right), & \text{if } \left(\frac{grad_A + grad_P}{2}\right) < 1 \\ 0, & \text{otherwise} \end{cases} \tag{4.47}$$

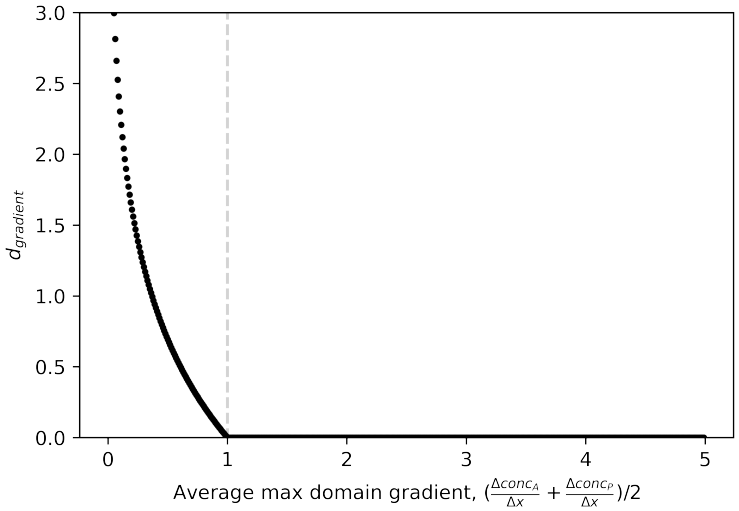
As the cell is approximated to be symmetric in geometry, the scoring function relating to the point of intersection is symmetric about the mid-point fig. 4.33a. Domain intersections close to that of mid-cell are not additionally penalised. The gradient score serves only to penalise shallow domain formation.



(a)



(b)

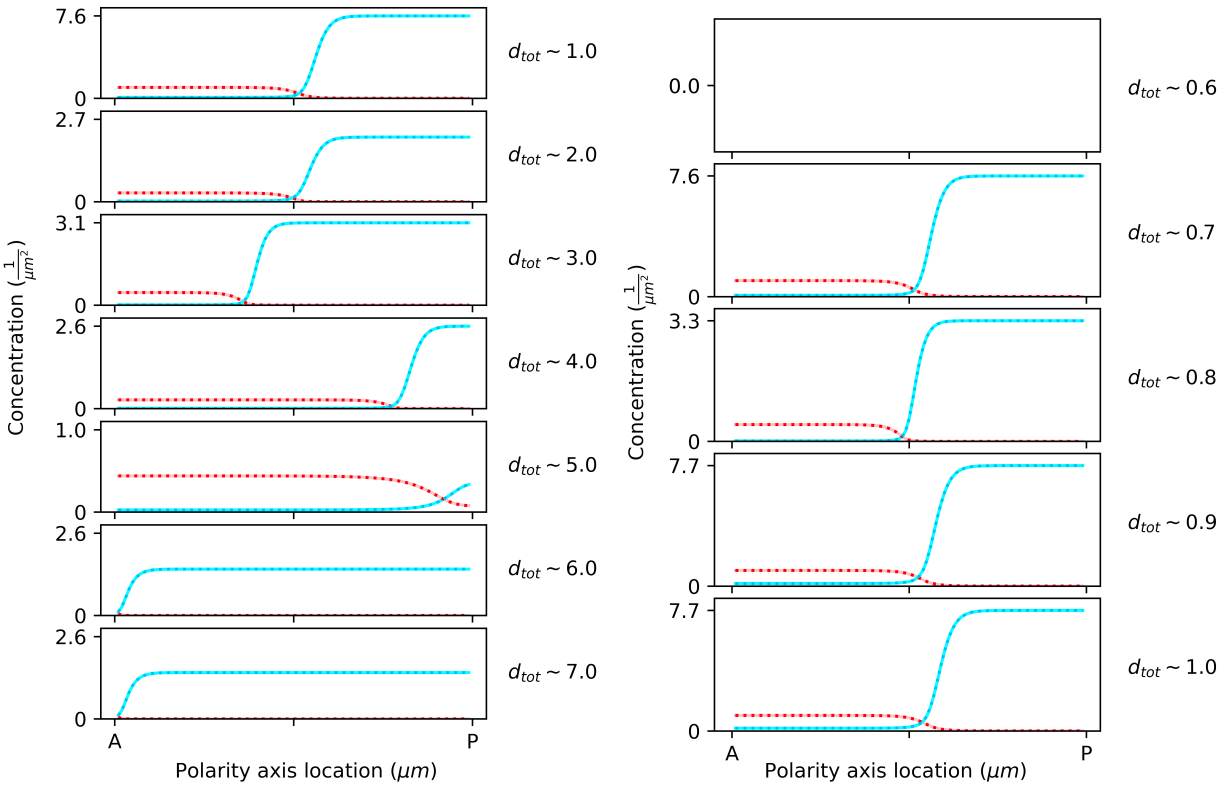


(c)

Figure 4.33: The allocation of distance scores based on characteristics of polarisation. Summary statistics were penalised according to their: **(a)** positioning of the domain boundary **(b)** the relative height of domain profiles and **(c)** the steepness of the domain profiles at the boundary.

4.6.3.3 Threshold

The threshold for acceptance was an average distance score of $\sigma \leq 1.25$. To decide this threshold, we conducted a manual investigation of polarisation outcomes and their associated scores. This broad investigation of scores revealed a breakdown of polarisation at $d_{tot} \sim 5.0$ and successful polarisation at $d_{tot} \lesssim 2.0$.



(a) **(b)**

Figure 4.34: A manual investigation of distance scores and their associated polarisation outcomes. **(a)** A broad exploration of possible scores illustrates the incremental loss of polarity. **(b)** A focus on low scores illustrates that or scoring system can successfully rank polarisation outcomes.

Chapter 5

Conclusions and Outlook

The general aim of this thesis was to uncover design principles encoded in the PAR polarity network that enable successful and robust polarisation of the *C. elegans* zygote. We drew a particular focus to the role of the clustering PAR-3 species, which is indispensable for polarisation and gates membrane association of other key polarity complexes [76][60].

PAR-3 is known to respond to polarising cortical flows during establishment phase and both cluster number and intensity is upregulated during at this time [60]. In chapter 2 we utilised methods from image analysis to investigate the functional relationship between clustering and cortical flows. In this manner, we view upregulated PAR-3 clustering as an enhancement of the cue-sensing ability of the system, enabling it to respond to polarity cues effectively. We applied Particle Image Velocimetry to microscopy images of dual labelled PAR-3/NMY-2 embryos and demonstrated that the global flow of PAR-3 clusters along the polarity axis is characteristically similar to flows observed in the cortex. Additionally, we found that PAR-3 clusters are closely coupled to local flows, with average flow velocities matching that of the NMY-2 cortex.

PAR-3 clustering has been shown to be indispensable for polarisation and it has recently been suggested that PAR-3 clustering may function to directly enhance efficiency of translocation to the anterior [78]. However, grouping our analysis of PAR-3 translocation in response to cortical flows by cluster size revealed that the largest and smallest clusters flow to the anterior with equal efficiency. Single particle tracking is less able to accurately track smaller clusters and so it is likely that our analysis is biased towards

larger PAR-3 populations. Therefore, we cannot eliminate the hypothesis of a threshold dependency on cluster size for efficiency of translocation by flows, if this threshold size was small. Interestingly, recent models of biophysical cluster transport in response to flows suggest that the scalar projection of PAR-3 cluster motion may provide insight into the mechanism by which PAR-3 clusters sense cortical flows [140]. Our findings that cluster size is dispensable for PAR-3 advection by flow would suggest that PAR-3 is directly coupled to the cortex. However, the scalar projection metric distinguishes between models of PAR-3 cluster transport most clearly at low cluster sizes and so an expansion of our analysis to experimental data that favours smaller clusters would be beneficial to our understanding of PAR-3 clustering and its role in polarity establishment.

Inspired by the finding that indirect cortical tension rescued PAR-3 clustering, we investigated whether PAR-3 clustering was directly enhanced as a result of physical interaction with the contracting cortex [72]. We calculated the divergence of our global flow field and investigated whether larger PAR-3 cluster were preferentially located in areas of negative divergence (contraction), or underwent preferential enhancement of size after emerging from a region of contraction. We found no correlation between cluster size, cluster enhancement and local regions of cortical contraction. This could indicate that the clusters are not directly bound to the membrane. Algorithms that remove erroneous tracks in single particle tracking are also likely to remove particle merging events which could arise due to contraction of the membrane. This may limit our analysis, though it is expected that should this be the primary driver of PAR-3 clustering then these merging events would be observed more prominently *in-vivo*. Additionally, our finding that PAR-3 clusters may not directly sense forces in the contracting membrane are in line with recent findings suggesting that PAR-3 clusters are not directly associated with the membrane and instead sense cortical flows as a result of viscous drag [118]. When PAR-3 is removed from the embryo polarity is disrupted and the cell fails to divide asymmetrically - indicating a fundamental role for PAR-3 in the successful polarisation of the embryo. Coupled with our analysis of PAR-3 clusters in response to cortical flows, we investigated the design principles of a polarity network explicitly encompassing a flow-sensing, PAR-3

complex. Guided by experimental observation and hypothesis, we investigated possible network topologies describing the aPKC cycle - whereby PAR-6/aPKC cycles between an inactive, flow-sensing PAR-3 state and an activated, diffuse CDC-42 state [78] [60]. Modelling these sub-complexes of the anterior PAR system takes a novel and important step toward understanding the design principles underpinning successful and robust polarisation of the cell. We find that direct coupling of the CDC-42/PAR-6/aPKC (active) to PAR-3/PAR-6/aPKC (inactive) through a cyclic motif results in a system that is both sensitive to perturbation and does not produce final domains with features that are observed *in vivo*. Rather, we find that an uncoupled network without a direct cycle, where PAR-3 clusters enhance binding of PAR-6/aPKC to the membrane and thus production of the active CDC-42/PAR-6/aPKC state is a more suitable candidate for polarisation of the single cell. The relaxation of the constraint on the production of an active state via an inactive, but antagonised, complex enables the uncoupled model to produce biologically viable domain states which encompass all the hallmarks of polarised domains *in vivo*. These findings discredit the applicability of the model of polarisation hypothesised by Rodriguez et al., where PAR-6/aPKC directly cycles between the two functionally distinct PAR-3 and CDC-42 associated complexes. In this context, the imposition of the cyclic motif coupled with the mass-conservation existent in the PAR circuit serves to hinder rather promote robust polarisation.

Work in synthetic systems has indicated that in simple systems, coupling both double-negative feedback (analogous to mutual antagonism) and positive feedback (analogous to PAR-3 clustering) works to enhance robustness of polarisation [141]. Separately, these mechanisms have been previously implicated in stabilising PAR polarisation in the *C. elegans* zygote [74] [65] [56]. Our implementation of Approximate Bayesian Computation to assess robustness of our extended models revealed that neither extended model exhibited enhanced robustness to mutual antagonism than the simple 2-PAR model of Goehring et al. Our findings highlight the obstacles faced when considering these simple mechanisms in combination and embedded in more complex protein networks.

Additional components in increasingly complex systems are expensive to biology and

therefore usually endow the system with some form of increased robustness to variability, flexibility or efficiency of process [142]. Rodriguez et al. proposed the cycling of PAR-6/aPKC between different functional modules as a mechanism by which the cell can favour a dynamic/reactive anterior regime at different times in the cell cycle, when processes underlying polarisation require specific characteristics to occur effectively. Namely, when initiating polarisation during the establishment phase the zygote would favour a flow-sensing PAR-3 state and would then be able to switch to favouring a diffusive, active state during maintenance phase. Interestingly, our Bayesian analysis did reveal that in the uncoupled model polarisation occurred in a consistent region of antagonism parameter space when considering a system configured to favour either an active or flow-sensing state. The inclusion of functionally distinct complexes in the uncoupled model therefore endows the PAR polarity system with the temporal flexibility suggested by Rodriguez et al.. This flexibility of specialisation could describe a more robust system whereby the zygote can upregulate functionally specialised complexes to correct for variability or error of other, upstream polarity effectors. For instance, favoured production of a flow-sensing PAR-3 state would increase sensitivity to a disrupted polarising cue, rescuing polarisation. However, alike a toggle-switch mechanism, there must exist a lower threshold to ensure the increased sensitivity did not result in mis-polarisation in response to noise of the environment [143]. The tolerance of our extended models to external cues would be an interesting direction for future research.

Hierarchical layering of multiple redundant mechanisms are omnipresent in nature, increasing robustness of processes [144]. Notably, the uncoupled model performed most robustly when the diffusivity of the active posterior protein was slowed. Work by Sailer et al. has identified the posterior, clustering CHIN-1 as having a key role in polarity maintenance phase forming an effective sub-circuit with CDC-42 [65]. With clustering serving as an effective mechanism to slow diffusivity in PAR-3, it remains of interest whether the coincidence of CHIN-1 cluster formation with maintenance phase serves to enhance robustness of polarisation of an extended model of cell polarity.

Appendix A

Model parametrisations

Parameter	Value	Unit	Definition	Source
L	134.6	μm	Perimeter of long axis of prolate spheroid (dim. $27 \times 15 \times 15$)	Goehring et al., Science 2011 [70]
ψ	0.174	μm^{-1}	Surface to volume ratio of prolate spheroid (dim. $27 \times 15 \times 15$)	Goehring et al., Science 2011 [70]
ρ_A	1.56	μm^{-3}	Normalised density of species A	Goehring et al., Science 2011 [70]
ρ_P	1	μm^{-3}	Normalised density of species P	Goehring et al., Science 2011 [70]
D_{A3}	0.01	$\mu m^2 s^{-1}$	Diffusion constant, species A_3	Polarity lab, Francis Crick Institute 2017
D_{A42}	0.1	$\mu m^2 s^{-1}$	Diffusion constant, species A_{42}	Geohring et al., Journal Cell Biology [115]
D_P	0.15	$\mu m^2 s^{-1}$	Diffusion constant, species P	Geohring et al., Journal Cell Biology [115]
D_{Ac}	2000	$\mu m^2 s^{-1}$	Diffusion constant, cytosolic A	Goehring et al., Science 2011 [70]
D_{Pc}	2000	$\mu m^2 s^{-1}$	Diffusion constant, cytosolic P	Goehring et al., Science 2011 [70]
$K_{ON,A3}$	0.001	$\mu m s^{-1}$	Association constant, species A_3	*
K_{342}	0.00275–0.0275	s^{-1}	Conversion rate from A_3 to A_{42} associated species	*
$K_{ON,P}$	0.0474	$\mu m s^{-1}$	Association constant, species P	Goehring et al., Science 2011 [70]
$K_{OFF,A42}$	0.00275–0.0275	s^{-1}	Dissociation constant, species A_{42}	*
$K_{OFF,P}$	0.0073	s^{-1}	Dissociation constant, species P	Geohring et al., Journal Cell Biology [115]
K_{A3P}	0.01–1	$\mu m^4 s^{-1}$	Antagonism of species A_3 by species P	*
K_{PA42}	0.048–12	$\mu m^4 s^{-1}$	Antagonism of species P by species A_{42}	*
α	2	None	Stoichiometric term for bi-stability	Goehring et al., Science 2011 [70]
β	2	None	Stoichiometric term for bi-stability	Goehring et al., Science 2011 [70]

Table A.1: Parametrisation of the coupled aPKC model. * indicates an approximated parameter.

Parameter	Value	Unit	Definition
L	134.6	μm	Perimeter of long axis of prolate spheroid (dim. $27 \times 15 \times 15$)
ψ	0.174	μm^{-1}	Surface to volume ratio of prolate spheroid (dim. $27 \times 15 \times 15$)
ρ_A	1.56	μm^{-3}	Normalised density of species A
ρ_P	1	μm^{-3}	Normalised density of species P
D_{A3}	0.01	$\mu m^2 s^{-1}$	Diffusion constant, species A_3
D_{A42}	0.1	$\mu m^2 s^{-1}$	Diffusion constant, species A_{42}
$D_{P,FIA}$	0.01	$\mu m^2 s^{-1}$	Diffusion constant, flow-sensing inactive species P_{FIA}
$D_{P,DA}$	0.1	$\mu m^2 s^{-1}$	Diffusion constant, diffuse active species P_{DA}
D_{Ac}	2000	$\mu m^2 s^{-1}$	Diffusion constant, cytosolic A
D_{Pc}	2000	$\mu m^2 s^{-1}$	Diffusion constant, cytosolic P
$K_{ON,A3}$	0.001	$\mu m s^{-1}$	Association constant, species A_3
$K_{ON,PFIA}$	0.001	$\mu m s^{-1}$	Association constant, flow-sensing inactive species P_{FIA}
K_{342}	0.00275–0.0275	s^{-1}	Conversion rate from A_3 to A_{42} associated species
K_{FIADA}	0.00275–0.0275	s^{-1}	Conversion rate from P_{FIA} to P_{DA} associated species
$K_{OFF,A42}$	0.00275–0.0275	s^{-1}	Dissociation constant, species A_{42}
$K_{OFF,PDA}$	0.00275–0.0275	s^{-1}	Dissociation constant, species P_{DA}
K_{A3P}	0–30	$\mu m^4 s^{-1}$	Antagonism of species A_3 by species P_{DA}
K_{PA42}	0–30	$\mu m^4 s^{-1}$	Antagonism of species P_{FIA} by species A_{42}
α	2	None	Stoichiometric term for bi-stability
β	2	None	Stoichiometric term for bi-stability

Table A.2: Parametrisation of the symmetric aPKC model.

Parameter	Value	Unit	Definition	Source
L	134.6	μm	Perimeter of long axis of prolate spheroid (dim. $27 \times 15 \times 15$)	Goehring et al., Science 2011 [70]
ψ	0.174	μm^{-1}	Surface to volume ratio of prolate spheroid (dim. $27 \times 15 \times 15$)	Goehring et al., Science 2011 [70]
ρ_{A3}	0.78	μm^{-3}	Normalised density of species A_3	Polarity lab, Francis Crick Institute 2017
ρ_{A6}	1.56	μm^{-3}	Normalised density of species A_6	Goehring et al., Science 2011 [70]
ρ_P	1	μm^{-3}	Normalised density of species P	Goehring et al., Science 2011 [70]
D_{A3}	0.01	$\mu m^2 s^{-1}$	Diffusion constant, species A_3	Polarity lab, Francis Crick Institute 2017
D_{A6}	0.1	$\mu m^2 s^{-1}$	Diffusion constant, species A_6	Geohring et al., Journal Cell Biology [115]
D_P	0.15	$\mu m^2 s^{-1}$	Diffusion constant, species P	Goehring et al., Science 2011 [70]
D_{Ac3}	2000	$\mu m^2 s^{-1}$	Diffusion constant, cytosolic A_3	Goehring et al., Science 2011 [70]
D_{Ac6}	2000	$\mu m^2 s^{-1}$	Diffusion constant, cytosolic A_6	Goehring et al., Science 2011 [70]
D_{Pc}	2000	$\mu m^2 s^{-1}$	Diffusion constant, cytosolic P	Goehring et al., Science 2011 [70]
$K_{ON,A3}$	0.01	$\mu m s^{-1}$	Association constant, species A_3	*
$K_{ON,A6}$	0.01–0.05	$\mu m s^{-1}$	Association constant, species A_6	*
$K_{ON,P}$	0.0474	$\mu m s^{-1}$	Association constant, species P	*
$K_{OFF,A3}$	0.01	s^{-1}	Dissociation constant, species A_3	Polarity lab, Francis Crick Institute 2017
$K_{OFF,A6}$	0.1	s^{-1}	Dissociation constant, species A_6	Geohring et al., Journal Cell Biology [115]
$K_{OFF,P}$	0.0073	s^{-1}	Dissociation constant, species P	Geohring et al., Journal Cell Biology [115]
K_{A3P}	0.02–1	$\mu m^4 s^{-1}$	Antagonism of species A_3 by species P	*
K_{PA42}	0.4–960	$\mu m^4 s^{-1}$	Antagonism of species P by species A_6	*
α	2	None	Stoichiometric term for bi-stability	Goehring et al., Science 2011 [70]
β	2	None	Stoichiometric term for bi-stability	Goehring et al., Science 2011 [70]

Table A.3: Parametrisation of the uncoupled aPKC model. * indicates an approximated parameter.

Bibliography

[1] Michael Bradie and Fred D. Miller. Teleology and Natural Necessity in Aristotle. *History of Philosophy Quarterly*, 1(2):133–146, 1984. Publisher: [North American Philosophical Publications, University of Illinois Press].

[2] Shidan Lotfi and The Hegeler Institute. The 'Purposiveness' of Life: Kant's Critique of Natural Teleology. *Monist*, 93(1):123–134, 2010.

[3] T. B. VEBLEN. KANT'S CRITIQUE OF JUDGMENT. *The Journal of Speculative Philosophy*, 18(3):260–274, 1884. Publisher: Penn State University Press.

[4] Staffan Müller-Wille. Cell Theory, Specificity, and Reproduction, 1837–1870. *Studies in history and philosophy of biological and biomedical sciences*, 41(3):225–231, September 2010.

[5] Paolo Mazzarello. A unifying concept: the history of cell theory. *Nature Cell Biology*, 1(1):E13–E15, May 1999. Bandiera˙abtest: a Cg˙type: Nature Research Journals Number: 1 Primary˙atype: Reviews Publisher: Nature Publishing Group.

[6] P. Kyle Stanford. August Weismann's Theory of the Germ-Plasm and the Problem of Unconceived Alternatives. *History and Philosophy of the Life Sciences*, 27(2):163–199, 2005. Publisher: Stazione Zoologica Anton Dohrn - Napoli.

[7] Abigail P. Bline, Anne Le Goff, and Patrick Allard. What Is Lost in the Weismann Barrier? *Journal of Developmental Biology*, 8(4):E35, December 2020.

[8] Siegfried Roth. Mathematics and biology: a Kantian view on the history of pattern formation theory. *Development Genes and Evolution*, 221(5):255–279, December 2011.

[9] Arthur D. Lander. Pattern, Growth and Control. *Cell*, 144(6):955–969, March 2011.

[10] Philip Ball. In retrospect: On Growth and Form. *Nature*, 494(7435):32–33, February 2013. Bandiera˙abtest: a Cg˙type: Nature Research Journals Number: 7435 Primary˙atype: Books & Arts Publisher: Nature Publishing Group Subject˙term: Culture;Evolution;Mathematics and computing Subject˙term˙id: culture;evolution;mathematics-and-computing.

[11] Eric Karsenti. Self-organization in cell biology: a brief history. *Nature Reviews Molecular Cell Biology*, 9(3):255–262, March 2008.

[12] Nicolas Bacaër. Lotka, Volterra and the predator–prey system (1920–1926). In Nicolas Bacaër, editor, *A Short History of Mathematical Population Dynamics*, pages 71–76. Springer, London, 2011.

[13] Alan Turing. The Chemical Basis of Morphogenesis. page 36, March 1952.

[14] K. Kirschfeld and W. Reichardt. [Processing of stationary optical information by the complex eye of Limulus. (Ommatidial visual fields and spatial distribution of inhibition)]. *Kybernetik*, 2(2):43–61, June 1964.

[15] A. Gierer and H. Meinhardt. A theory of biological pattern formation. *Kybernetik*, 12(1):30–39, December 1972.

[16] Jeremy B. A. Green and James Sharpe. Positional information and reaction-diffusion: two big ideas in developmental biology combine. *Development*, 142(7):1203–1211, April 2015.

[17] Interactions between zebrafish pigment cells responsible for the generation of Turing patterns | PNAS.

[18] Tetsuya Nakamura, Naoki Mine, Etsushi Nakaguchi, Atsushi Mochizuki, Masamichi Yamamoto, Kenta Yashiro, Chikara Meno, and Hiroshi Hamada. Generation of Robust Left-Right Asymmetry in the Mouse Embryo Requires a Self-Enhancement and Lateral-Inhibition System. *Developmental Cell*, 11(4):495–504, October 2006.

[19] Martina Pesch and Martin Hülskamp. Creating a two-dimensional pattern de novo during Arabidopsis trichome and root hair initiation. *Current Opinion in Genetics & Development*, 14(4):422–427, August 2004.

[20] Stefanie Sick, Stefan Reinker, Jens Timmer, and Thomas Schlake. WNT and DKK Determine Hair Follicle Spacing Through a Reaction-Diffusion Mechanism. *Science*, 314(5804):1447–1450, December 2006. Publisher: American Association for the Advancement of Science Section: Report.

[21] Andrew D. Economou, Atsushi Ohazama, Thantrira Porntaveetus, Paul T. Sharpe, Shigeru Kondo, M. Albert Basson, Amel Gritli-Linde, Martyn T. Cobourne, and Jeremy B. A. Green. Periodic stripe formation by a Turing mechanism operating at growth zones in the mammalian palate. *Nature Genetics*, 44(3):348–351, March 2012. Bandiera˙abtest: a Cg˙type: Nature Research Journals Number: 3 Primary˙atype: Research Publisher: Nature Publishing Group Subject˙term: Development Subject˙term˙id: development.

[22] Susan G. Ernst. A Century of Sea Urchin Development. *American Zoologist*, 37(3):250–259, June 1997.

[23] Johannes Jaeger and Berta Verd. Dynamic positional information: Patterning mechanism versus precision in gradient-driven systems. In *Current Topics in Developmental Biology*, volume 137, pages 219–246. Elsevier, 2020.

[24] Anne Ephrussi and Daniel St Johnston. Seeing Is Believing: The Bicoid Morphogen Gradient Matures. *Cell*, 116(2):143–152, January 2004. Publisher: Elsevier.

[25] Lewis Wolpert and Cheryll Tickle. *Principles of Development*. OUP Oxford, 4 edition, January 2011.

[26] James Sharpe. Wolpert's French Flag: what's the problem? *Development*, 146(24), December 2019.

[27] Norbert Perrimon and Andrew P. McMahon. Negative Feedback Mechanisms and Their Roles during Pattern Formation. *Cell*, 97(1):13–16, April 1999. Publisher: Elsevier.

[28] Hans Meinhardt. Turing's theory of morphogenesis of 1952 and the subsequent discovery of the crucial role of local self-enhancement and long-range inhibition. *Interface Focus*, 2(4):407–416, August 2012.

[29] Alexander Y. Mitrophanov and Eduardo A. Groisman. Positive feedback in cellular control systems. *BioEssays : news and reviews in molecular, cellular and developmental biology*, 30(6):542–555, June 2008.

[30] Shigeru Kondo and Takashi Miura. Reaction-Diffusion Model as a Framework for Understanding Biological Pattern Formation. *Science*, 329(5999):1616–1620, September 2010.

[31] Brian D. Slaughter, Sarah E. Smith, and Rong Li. Symmetry Breaking in the Life Cycle of the Budding Yeast. *Cold Spring Harbor Perspectives in Biology*, 1(3):a003384, January 2009. Company: Cold Spring Harbor Laboratory Press Distributor: Cold Spring Harbor Laboratory Press Institution: Cold Spring Harbor Laboratory Press Label: Cold Spring Harbor Laboratory Press Publisher: Cold Spring Harbor Lab.

[32] A E Adams, D I Johnson, R M Longnecker, B F Sloat, and J R Pringle. CDC42 and CDC43, two additional genes involved in budding and the establishment of cell polarity in the yeast Saccharomyces cerevisiae. *Journal of Cell Biology*, 111(1):131–142, July 1990.

[33] Jian-geng Chiou, Mohan K. Balasubramanian, and Daniel J. Lew. Cell Polarity in Yeast. *Annual review of cell and developmental biology*, 33:77–101, October 2017.

[34] Anne-Christine Butty, Nathalie Perrinjaquet, Audrey Petit, Malika Jaquenoud, Jeffrey E. Segall, Kay Hofmann, Catherine Zwahlen, and Matthias Peter. A positive feedback loop stabilizes the guanine-nucleotide exchange factor Cdc24 at sites of polarization. *The EMBO Journal*, 21(7):1565–1576, April 2002.

[35] Beatrice Ramm, Tamara Heermann, and Petra Schwille. The E. coli MinCDE system in the regulation of protein patterns and gradients. *Cellular and Molecular Life Sciences*, 76(21):4245–4273, November 2019.

[36] Jakob Schweizer, Martin Loose, Mike Bonny, Karsten Kruse, Ingolf Mönch, and Petra Schwille. Geometry sensing by self-organized protein patterns. *Proceedings of the National Academy of Sciences*, 109(38):15283–15288, September 2012. Publisher: National Academy of Sciences Section: Biological Sciences.

[37] Tetsuya Takano, Chundi Xu, Yasuhiro Funahashi, Takashi Namba, and Kozo Kaibuchi. Neuronal polarization. *Development*, 142(12):2088–2093, June 2015.

[38] Tetsuya Takano, Mengya Wu, Shinichi Nakamuta, Honda Naoki, Naruki Ishizawa, Takashi Namba, Takashi Watanabe, Chundi Xu, Tomonari Hamaguchi, Yoshimitsu Yura, Mutsuki Amano, Klaus M. Hahn, and Kozo Kaibuchi. Discovery of long-range inhibitory signaling to ensure single axon formation. *Nature Communications*, 8(1):33, June 2017. Bandiera˙abtest: a Cc˙license˙type: cc˙by Cg˙type: Nature Research Journals Number: 1 Primary˙atype: Research Publisher: Nature Publishing Group Subject˙term: Cellular neuroscience;Neuronal development Subject˙term˙id: cellular-neuroscience;neuronal-development.

[39] Marie-Dominique Filippi. Neutrophil transendothelial migration: updates and new perspectives. *Blood*, 133(20):2149–2158, May 2019.

[40] Sachin Kumar, Juying Xu, Charles Perkins, Fukun Guo, Scott Snapper, Fred D. Finkelman, Yi Zheng, and Marie-Dominique Filippi. Cdc42 regulates neutrophil migration via crosstalk between WASp, CD11b, and microtubules. *Blood*, 120(17):3563–3574, October 2012.

[41] Kathleen Szczur, Yi Zheng, and Marie-Dominique Filippi. The small Rho GTPase Cdc42 regulates neutrophil polarity via CD11b integrin signaling. *Blood*, 114(20):4527–4537, November 2009.

[42] Daniel Muschiol, Fabian Schroeder, and Walter Traunspurger. Life cycle and population growth rate of Caenorhabditis elegans studied by a new method. *BMC Ecology*, 9(1):14, May 2009.

[43] Da Yin and Eric S. Haag. Evolution of sex ratio through gene loss. *Proceedings of the National Academy of Sciences*, 116(26):12919–12924, June 2019.

[44] Donald L. Riddle, Thomas Blumenthal, Barbara J. Meyer, and James R. Priess. *Fertilization*. Cold Spring Harbor Laboratory Press, 1997. Publication Title: C. elegans II. 2nd edition.

[45] Edwin Munro, Jeremy Nance, and James R. Priess. Cortical Flows Powered by Asymmetrical Contraction Transport PAR Proteins to Establish and Maintain Anterior-Posterior Polarity in the Early C. elegans Embryo. *Developmental Cell*, 7(3):413–424, September 2004.

[46] Sukriti Kapoor and Sachin Kotak. Centrosome Aurora A regulates RhoGEF ECT-2 localisation and ensures a single PAR-2 polarity axis in C. elegans embryos. *Development*, 146(22), November 2019.

[47] Pavan Kadandale and Andrew Singson. Oocyte production and sperm utilization patterns in semi-fertile strains of Caenorhabditis elegans. *BMC Developmental Biology*, 4:3, April 2004.

[48] Raphaela Gessele, Jacob Halatek, and Erwin Frey. PAR protein activation-deactivation cycles stabilize long-axis polarization in C. elegans. *bioRxiv*, page 451880, October 2018.

[49] M. L. Begasse and A. A. Hyman. The first cell cycle of the Caenorhabditis elegans embryo: spatial and temporal control of an asymmetric cell division. *Results and problems in cell differentiation*, 53:109–133, 2011.

[50] Laurence Pelletier, Nurhan Özlü, Eva Hannak, Carrie Cowan, Bianca Habermann, Martine Ruer, Thomas Müller-Reichert, and Anthony A Hyman. The Caenorhabditis elegans Centrosomal Protein SPD-2 Is Required for both Pericentriolar Material Recruitment and Centriole Duplication. *Current Biology*, 14(10):863–873, May 2004.

[51] Lionel Pintard and Bruce Bowerman. Mitotic Cell Division in Caenorhabditis elegans. *Genetics*, 211(1):35–73, January 2019. Publisher: Genetics Section: Wormbook.

[52] Pierre Gönczy. Mechanisms of asymmetric cell division: flies and worms pave the way. *Nature Reviews Molecular Cell Biology*, 9(5):355–366, May 2008.

[53] Jacques Pécréaux, Stefanie Redemann, Zahraa Alayan, Benjamin Mercat, Sylvain Pastezeur, Carlos Garzon-Coral, Anthony A. Hyman, and Jonathon Howard. The Mitotic Spindle in the One-Cell C. elegans Embryo Is Positioned with High Precision and Stability. *Biophysical Journal*, 111(8):1773–1784, October 2016.

[54] K. J. Kemphues, J. R. Priess, D. G. Morton, and N. S. Cheng. Identification of genes required for cytoplasmic localization in early C. elegans embryos. *Cell*, 52(3):311–320, February 1988.

[55] Shawn N. Jordan, Tim Davies, Yelena Zhuravlev, Julien Dumont, Mimi Shirasu-Hiza, and Julie C. Canman. Cortical PAR polarity proteins promote robust cytokinesis during asymmetric cell division. *The Journal of Cell Biology*, 212(1):39–49, January 2016.

[56] Charles F. Lang and Edwin Munro. The PAR proteins: from molecular circuits to dynamic self-stabilizing cell polarity. *Development*, 144(19):3405–3416, October 2017.

[57] Adrian A. Cuenca, Aaron Schetter, Donato Aceto, Kenneth Kemphues, and Geraldine Seydoux. Polarization of the C. elegans zygote proceeds via distinct establish-

ment and maintenance phases. *Development (Cambridge, England)*, 130(7):1255–1265, April 2003.

[58] Jörg Betschinger and Jürgen A. Knoblich. Dare to Be Different: Asymmetric Cell Division in Drosophila, C. elegans and Vertebrates. *Current Biology*, 14(16):R674–R685, August 2004.

[59] Dan Lin, Amelia S. Edwards, James P. Fawcett, Geraldine Mbamalu, John D. Scott, and Tony Pawson. A mammalian PAR-3–PAR-6 complex implicated in Cdc42/Rac1 and aPKC signalling and cell polarity. *Nature Cell Biology*, 2(8):540–547, August 2000. Bandiera˙abtest: a Cg˙type: Nature Research Journals Number: 8 Primary˙atype: Research Publisher: Nature Publishing Group.

[60] Daniel J. Dickinson, Francoise Schwager, Lionel Pintard, Monica Gotta, and Bob Goldstein. A Single-Cell Biochemistry Approach Reveals PAR Complex Dynamics during Cell Polarization. *Developmental Cell*, 42(4):416–434.e11, August 2017.

[61] Jin Li, Heon Kim, Donato G. Aceto, Jeffrey Hung, Shinya Aono, and Kenneth J. Kemphues. Binding to PKC-3, but not to PAR-3 or to a conventional PDZ domain ligand, is required for PAR-6 function in C. elegans. *Developmental Biology*, 340(1):88–98, April 2010.

[62] Donato Aceto, Melissa Beers, and Kenneth J. Kemphues. Interaction of PAR-6 with CDC-42 is required for maintenance but not establishment of PAR asymmetry in C. elegans. *Developmental Biology*, 299(2):386–397, November 2006.

[63] Fumio Motegi, Seth Zonies, Yingsong Hao, Adrian A. Cuenca, Erik Griffin, and Geraldine Seydoux. Microtubules induce self-organization of polarized PAR domains in C. elegans zygotes. *Nature cell biology*, 13(11):1361–1367, October 2011.

[64] F. Motegi and G. Seydoux. The PAR network: redundancy and robustness in a symmetry-breaking system. *Philosophical Transactions of the Royal Society B: Biological Sciences*, 368(1629):20130010–20130010, September 2013.

[65] Anne Sailer, Alexander Anneken, Younan Li, Sam Lee, and Edwin Munro. Dynamic Opposition of Clustered Proteins Stabilizes Cortical Polarity in the C. elegans Zygote. *Developmental Cell*, 35(1):131–142, October 2015.

[66] Alexander Beatty, Diane Morton, and Kenneth Kemphues. The C. elegans homolog of Drosophila Lethal giant larvae functions redundantly with PAR-2 to maintain polarity in the early embryo. *Development (Cambridge, England)*, 137(23):3995–4004, December 2010.

[67] Lawrence E. Small and Adriana T. Dawes. PAR proteins regulate maintenance-phase myosin dynamics during Caenorhabditis elegans zygote polarization. *Molecular Biology of the Cell*, 28(16):2220–2231, August 2017. Publisher: American Society for Cell Biology (mboc).

[68] Marie-Anne Félix and Michalis Barkoulas. Pervasive robustness in biological systems. *Nature Reviews Genetics*, 16(8):483–496, August 2015. Bandiera˙abtest: a Cg˙type: Nature Research Journals Number: 8 Primary˙atype: Reviews Publisher: Nature Publishing Group Subject˙term: Computational biology and bioinformatics;Evolvability;Robustness Subject˙term˙id: computational-biology-and-bioinformatics;evolvability;robustness.

[69] James Michael Whitacre. Biological Robustness: Paradigms, Mechanisms, and Systems Principles. *Frontiers in Genetics*, 3:67, May 2012.

[70] Nathan W. Goehring, Philipp Khuc Trong, Justin S. Bois, Debanjan Chowdhury, Ernesto M. Nicola, Anthony A. Hyman, and Stephan W. Grill. Polarization of PAR Proteins by Advective Triggering of a Pattern-Forming System. *Science*, 334(6059):1137–1141, November 2011.

[71] Peter Gross, K. Vijay Kumar, Nathan W. Goehring, Justin S. Bois, Carsten Hoege, Frank Jülicher, and Stephan W. Grill. Guiding self-organized pattern formation in cell polarity establishment. *Nature Physics*, 15(3):293–300, March 2019.

[72] Shyi-Chyi Wang, Tricia Yu Feng Low, Yukako Nishimura, Laurent Gole, Weimiao Yu, and Fumio Motegi. Cortical forces and CDC-42 control clustering of PAR proteins for Caenorhabditis elegans embryonic polarization. *Nature Cell Biology*, 19(8):988–995, July 2017.

[73] Bob Goldstein and Ian G. Macara. The PAR proteins: fundamental players in animal cell polarization. *Developmental Cell*, 13(5):609–622, November 2007.

[74] Edwin Munro. Protein Clustering Shapes Polarity Protein Gradients. *Developmental Cell*, 42(4):309–311, August 2017.

[75] Tony J. C. Harris. Protein clustering for cell polarity: Par-3 as a paradigm. *F1000Research*, 6, August 2017.

[76] Bijan Etemad-Moghadam, Su Guo, and Kenneth J. Kemphues. Asymmetrically distributed PAR-3 protein contributes to cell polarity and spindle alignment in early C. elegans embryos. *Cell*, 83(5):743–752, December 1995.

[77] Erika V. Soriano, Marina E. Ivanova, Georgina Fletcher, Philippe Riou, Philip P. Knowles, Karin Barnouin, Andrew Purkiss, Brenda Kostelecky, Peter Saiu, Mark Linch, Ahmed Elbediwy, Svend Kjær, Nicola O'Reilly, Ambrosius P. Snijders, Peter J. Parker, Barry J. Thompson, and Neil Q. McDonald. aPKC Inhibition by Par3 CR3 Flanking Regions Controls Substrate Access and Underpins Apical-Junctional Polarization. *Developmental Cell*, 38(4):384–398, August 2016.

[78] Josana Rodriguez, Florent Peglion, Jack Martin, Lars Hubatsch, Jacob Reich, Nisha Hirani, Alicia G. Gubieda, Jon Roffey, Artur Ribeiro Fernandes, Daniel St Johnston, Julie Ahringer, and Nathan W. Goehring. aPKC Cycles between Functionally Distinct PAR Protein Assemblies to Drive Cell Polarity. *Developmental Cell*, 42(4):400–415.e9, August 2017.

[79] Hiroaki Kitano. Biological robustness. *Nature Reviews Genetics*, 5(11):826–837, November 2004.

[80] D. Bray and J. G. White. Cortical flow in animal cells. *Science*, 239(4842):883–888, February 1988.

[81] U. Wolke, E. A. Jezuit, and J. R. Priess. Actin-dependent cytoplasmic streaming in C. elegans oogenesis. *Development*, 134(12):2227–2236, May 2007.

[82] Rob Phillips and Janes Kondev. *Physical Biology of the Cell*. Garland Science, 2 edition, November 2012.

[83] Thomas D. Pollard and John A. Cooper. Actin and Actin-Binding Proteins. a Critical Evaluation of Mechanisms and Functions. *Annual Review of Biochemistry*, 55(1):987–1035, 1986. eprint: https://doi.org/10.1146/annurev.bi.55.070186.005011.

[84] Benjamin A. Smith, Karen Daugherty-Clarke, Bruce L. Goode, and Jeff Gelles. Pathway of actin filament branch formation by Arp2/3 complex revealed by single-molecule imaging. *Proceedings of the National Academy of Sciences*, 110(4):1285–1290, January 2013. Publisher: National Academy of Sciences Section: Biological Sciences.

[85] Laurent Blanchoin, Rajaa Boujemaa-Paterski, Cécile Sykes, and Julie Plastino. Actin Dynamics, Architecture, and Mechanics in Cell Motility. *Physiological Reviews*, 94(1):235–263, January 2014. Publisher: American Physiological Society.

[86] Geoffrey M. Cooper. Actin, Myosin, and Cell Movement. *The Cell: A Molecular Approach. 2nd edition*, 2000. Publisher: Sinauer Associates.

[87] Kevin J. Chalut and Ewa K. Paluch. The Actin Cortex: A Bridge between Cell Shape and Function. *Developmental Cell*, 38(6):571–573, September 2016. Publisher: Elsevier.

[88] Michael Murrell, Patrick W. Oakes, Martin Lenz, and Margaret L. Gardel. Forcing cells into shape: the mechanics of actomyosin contractility. *Nature Reviews Molecular Cell Biology*, 16(8):486–498, August 2015.

[89] Gijsje H Koenderink and Ewa K Paluch. Architecture shapes contractility in actomyosin networks. *Current Opinion in Cell Biology*, 50:79–85, February 2018.

[90] Martin Lenz, Todd Thoresen, Margaret L. Gardel, and Aaron R. Dinner. Contractile Units in Disordered Actomyosin Bundles Arise from F-Actin Buckling. *Physical Review Letters*, 108(23), June 2012.

[91] Poul M. Bendix, Gijsje H. Koenderink, Damien Cuvelier, Zvonimir Dogic, Bernard N. Koeleman, William M. Brieher, Christine M. Field, L. Mahadevan, and David A. Weitz. A quantitative analysis of contractility in active cytoskeletal protein networks. *Biophysical Journal*, 94(8):3126–3136, April 2008.

[92] Wei Yung Ding, Hui Ting Ong, Yusuke Hara, Jantana Wongsantichon, Yusuke Toyama, Robert C. Robinson, François Nédélec, and Ronen Zaidel-Bar. Plastin increases cortical connectivity to facilitate robust polarization and timely cytokinesis. *The Journal of Cell Biology*, 216(5):1371–1386, May 2017.

[93] Masatoshi Nishikawa, Sundar Ram Naganathan, Frank Jülicher, and Stephan W Grill. Controlling contractile instabilities in the actomyosin cortex. *eLife*, 6, January 2017.

[94] Aaron F. Severson, David L. Baillie, and Bruce Bowerman. A Formin Homology Protein and a Profilin Are Required for Cytokinesis and Arp2/3-Independent Assembly of Cortical Microfilaments in C. elegans. *Current Biology*, 12(24):2066–2075, December 2002.

[95] Weiwei Luo, Cheng-han Yu, Zi Zhao Lieu, Jun Allard, Alex Mogilner, Michael P. Sheetz, and Alexander D. Bershadsky. Analysis of the local organization and dynamics of cellular actin networks. *J Cell Biol*, 202(7):1057–1073, September 2013.

[96] S. N. Hird and J. G. White. Cortical and cytoplasmic flow polarity in early embryonic cells of Caenorhabditis elegans. *The Journal of Cell Biology*, 121(6):1343–1355, June 1993.

[97] David P Hill and SUSAN STROMEf. Brief cytochalasin-induced disruption of microfilaments during a critical interval in 1-cell C. elegans embryos alters the partitioning of developmental instructions to the 2-cell embryo. page 14.

[98] Mirjam Mayer, Martin Depken, Justin S. Bois, Frank Jülicher, and Stephan W. Grill. Anisotropies in cortical tension reveal the physical basis of polarizing cortical flows. *Nature*, 467(7315):617–621, September 2010.

[99] Sundar Ram Naganathan, Sebastian Fürthauer, Masatoshi Nishikawa, Frank Jülicher, and Stephan W. Grill. Active torque generation by the actomyosin cell cortex drives left–right symmetry breaking. *eLife*, December 2014.

[100] G. Salbreux, J. Prost, and J. F. Joanny. Hydrodynamics of Cellular Cortical Flows and the Formation of Contractile Rings. *Physical Review Letters*, 103(5), July 2009.

[101] Betül Senay Aras, Y. C. Zhou, Adriana Dawes, and Ching-Shan Chou. The importance of mechanical constraints for proper polarization and psuedo-cleavage furrow generation in the early Caenorhabditis elegans embryo. *PLOS Computational Biology*, 14(7):e1006294, July 2018.

[102] Carrie R. Cowan and Anthony A. Hyman. Acto-myosin reorganization and PAR polarity in C. elegans. *Development*, 134(6):1035–1043, March 2007.

[103] Woongjoon Moon and Fumio Matsuzaki. Aurora A kinase negatively regulates Rho-kinase by phosphorylation in vivo. *Biochemical and Biophysical Research Communications*, 435(4):610–615, June 2013.

[104] Wan Jun Gan and Fumio Motegi. Mechanochemical Control of Symmetry Breaking in the Caenorhabditis elegans Zygote. *Frontiers in Cell and Developmental Biology*, 8:1714, 2021.

[105] Stephanie Schonegg and Anthony A. Hyman. CDC-42 and RHO-1 coordinate acto-myosin contractility and PAR protein localization during polarity establishment in C. elegans embryos. *Development (Cambridge, England)*, 133(18):3507–3516, September 2006.

[106] Kerstin Klinkert, Nicolas Levernier, Peter Gross, Christian Gentili, Lukas von Tobel, Marie Pierron, Coralie Busso, Sarah Herrman, Stephan W Grill, Karsten Kruse, and Pierre Gönczy. Aurora A depletion reveals centrosome-independent polarization mechanism in Caenorhabditis elegans. *eLife*, 8:e44552.

[107] N. Jenkins. CYK-4/GAP Provides a Localized Cue to Initiate Anteroposterior Polarity upon Fertilization. *Science*, 313(5791):1298–1301, September 2006.

[108] Fumio Motegi and Asako Sugimoto. Sequential functioning of the ECT-2 RhoGEF, RHO-1 and CDC-42 establishes cell polarity in Caenorhabditis elegans embryos. *Nature Cell Biology*, 8(9):978–985, September 2006.

[109] G. Joberty, C. Petersen, L. Gao, and I. G. Macara. The cell-polarity protein Par6 links Par3 and atypical protein kinase C to Cdc42. *Nature Cell Biology*, 2(8):531–539, August 2000.

[110] M. Beers and Kenneth Kemphues. Depletion of the co-chaperone CDC-37 reveals two modes of PAR-6 cortical association in C. elegans embryos. *Development*, 133(19):3745–3754, October 2006.

[111] Monica Gotta, Mary C. Abraham, and Julie Ahringer. CDC-42 controls early cell polarity and spindle orientation in C. elegans. *Current Biology*, 11(7):482–488, April 2001.

[112] Keiko Mizuno, Atsushi Suzuki, Tomonori Hirose, Koichi Kitamura, Koichi Kutsuzawa, Masaaki Futaki, Yoshiko Amano, and Shigeo Ohno. Self-association of PAR-3-mediated by the conserved N-terminal domain contributes to the development of epithelial tight junctions. *The Journal of Biological Chemistry*, 278(33):31240–31250, August 2003.

[113] Clifford P. Brangwynne, Christian R. Eckmann, David S. Courson, Agata Rybarska, Carsten Hoege, Jöbin Gharakhani, Frank Jülicher, and Anthony A. Hyman. Germline P granules are liquid droplets that localize by controlled dissolution/condensation. *Science (New York, N.Y.)*, 324(5935):1729–1732, June 2009.

[114] Pierre Recouvreux and Pierre-François Lenne. Molecular clustering in the cell: from weak interactions to optimized functional architectures. *Current Opinion in Cell Biology*, 38:18–23, February 2016.

[115] Nathan W. Goehring, Carsten Hoege, Stephan W. Grill, and Anthony A. Hyman. PAR proteins diffuse freely across the anterior–posterior boundary in polarized *C. elegans* embryos. *The Journal of Cell Biology*, 193(3):583–594, May 2011.

[116] Adriana T. Dawes and Edwin M. Munro. PAR-3 Oligomerization May Provide an Actin-Independent Mechanism to Maintain Distinct Par Protein Domains in the Early Caenorhabditis elegans Embryo. *Biophysical Journal*, 101(6):1412–1422, September 2011.

[117] Robert G. Endres. *Physical Principles in Sensing and Signaling: With an Introduction to Modeling in Biology.* Oxford University Press, Incorporated, Oxford, UNITED KINGDOM, 2013.

[118] Yiran Chang and Daniel J. Dickinson. A particle size threshold governs diffusion and segregation of PAR-3 during cell polarization. preprint, Cell Biology, June 2021.

[119] Nicole Gorfinkiel. From actomyosin oscillations to tissue-level deformations. *Developmental Dynamics*, 245(3):268–275, 2016. ˙eprint: https://anatomypubs.onlinelibrary.wiley.com/doi/pdf/10.1002/dvdy.24363.

[120] Ajay K. Prasad. Particle Image Velocimetry. *Current Science*, 79(1), July 2000.

[121] Richard D. Keane and Ronald J. Adrian. Theory and simulation of particle image velocimetry. In *Fifth International Conference on Laser Anemometry: Advances and Applications*, volume 2052, pages 477–492. International Society for Optics and Photonics, August 1993.

[122] Sven Scharnowski and Christian J. Kähler. Particle image velocimetry - Classical operating rules from today's perspective. *Optics and Lasers in Engineering*, 135:106185, December 2020.

[123] William Thielicke and Eize Stamhuis. PIVlab – Towards User-friendly, Affordable and Accurate Digital Particle Image Velocimetry in MATLAB. *Journal of Open Research Software*, 2(1):e30, October 2014.

[124] Seth Zonies, Fumio Motegi, Yingsong Hao, and Geraldine Seydoux. Symmetry breaking and polarization of the C. elegans zygote by the polarity protein PAR-2. *Development*, page dev.045823, January 2010.

[125] J. L. Watts, B. Etemad-Moghadam, S. Guo, L. Boyd, B. W. Draper, C. C. Mello, J. R. Priess, and K. J. Kemphues. par-6, a gene involved in the establishment of asymmetry in early C. elegans embryos, mediates the asymmetric localization of PAR-3. *Development*, 122(10):3133–3140, October 1996.

[126] Yoichiro Mori, Alexandra Jilkine, and Leah Edelstein-Keshet. Wave-Pinning and Cell Polarity from a Bistable Reaction-Diffusion System. *Biophysical Journal*, 94(9):3684–3697, May 2008.

[127] Lars Hubatsch, Florent Peglion, Jacob D Reich, Nelio TL Rodrigues, Nisha Hirani, Rukshala Illukkumbura, and Nathan W Goehring. A cell size threshold limits cell polarity and asymmetric division potential. *Nature physics*, 15(10):1075–1085, June 2019.

[128] Sungrim Seirin Lee and Tatsuo Shibata. Self-organization and advective transport in the cell polarity formation for asymmetric cell division. *Journal of Theoretical Biology*, 382:1–14, October 2015.

[129] Filipe Tostevin and Martin Howard. Modeling the Establishment of PAR Protein Polarity in the One-Cell C. elegans Embryo. *Biophysical Journal*, 95(10):4512–4522, November 2008.

[130] Ryan N. Gutenkunst, Joshua J. Waterfall, Fergal P. Casey, Kevin S. Brown, Christopher R. Myers, and James P. Sethna. Universally Sloppy Parameter Sensitivities in Systems Biology Models. *PLOS Computational Biology*, 3(10):e189, October 2007.

[131] Lars Hubatsch. Interplay between Cell Size and Cell Polarity, 2018.

[132] Branimir K. Hackenberger. Bayes or not Bayes, is this the question? *Croatian Medical Journal*, 60(1):50–52, February 2019.

[133] Tina Toni, David Welch, Natalja Strelkowa, Andreas Ipsen, and Michael P.H Stumpf. Approximate Bayesian computation scheme for parameter inference and model selection in dynamical systems. *Journal of The Royal Society Interface*, 6(31):187–202, February 2009.

[134] Kristi Bray, Melissa Gillette, Jeanette Young, Elizabeth Loughran, Melissa Hwang, James Cooper Sears, and Tracy Vargo-Gogola. Cdc42 overexpression induces hyperbranching in the developing mammary gland by enhancing cell migration. *Breast Cancer Research*, 15(5):R91, September 2013.

[135] Christopher A. Shelton, J. Clayton Carter, Gregory C. Ellis, and Bruce Bowerman. The Nonmuscle Myosin Regulatory Light Chain Gene mlc-4 Is Required for Cytokinesis, Anterior-Posterior Polarity, and Body Morphology during Caenorhabditis elegans Embryogenesis. *The Journal of Cell Biology*, 146(2):439–451, July 1999.

[136] Christian Schenk, Henrik Bringmann, Anthony A. Hyman, and Carrie R. Cowan. Cortical domain correction repositions the polarity boundary to match the cytokinesis furrow in C. elegans embryos. *Development (Cambridge, England)*, 137(10):1743–1753, May 2010.

[137] Peter Olver. *Introduction to Partial Differential Equations*. Springer, 1 edition, 2014.

[138] H. P. Langtangen. Truncation Error Analysis, December 2013.

[139] P. Valenta. Beam-Warming second-order upwind method, January 2015.

[140] Cole Zmurchok and William R. Holmes. Biophysical Models of PAR Cluster Transport by Cortical Flow in *C. elegans* Early Embryogenesis. preprint, Biophysics, June 2021.

[141] Angela H. Chau, Jessica M. Walter, Jaline Gerardin, Chao Tang, and Wendell A. Lim. Designing Synthetic Regulatory Networks Capable of Self-Organizing Cell Polarization. *Cell*, 151(2):320–332, October 2012. Publisher: Elsevier.

[142] J. M. Carlson and John Doyle. Complexity and robustness. *Proceedings of the National Academy of Sciences*, 99(suppl 1):2538–2545, February 2002. Publisher: National Academy of Sciences Section: Colloquium Paper.

[143] Keun-Young Kim and Jin Wang. Potential Energy Landscape and Robustness of a Gene Regulatory Network: Toggle Switch. *PLOS Computational Biology*, 3(3):e60, March 2007. Publisher: Public Library of Science.

[144] Marie E. Csete and John C. Doyle. Reverse Engineering of Biological Complexity. *Science*, March 2002. Publisher: American Association for the Advancement of Science.